ALMA MATER STUDIORUM · UNIVERSITÀ DI BOLOGNA

Dottorato di Ricerca in

Future Earth, Climate Change and Societal Challenges

CYCLE XXXVI

Settore Concorsuale: 04/A4 GEOFISICA

Settore Scientifico Disciplinare: GEO/12 - OCEANOGRAFIA E FISICA DELL'ATMOSFERA

A NUMERICAL STUDY OF SUBSURFACE OIL SPILLS

Presentata da

Giulia Gronchi

Relatori

Prof.ssa Nadia Pinardi

Dr. Giovanni Coppini

Dr. Gianandrea Mannarini

Coordinatore di dottorato

Silvana di Sabatino

Esame finale anno 2024

Abstract

This thesis aims to tackle the numerical modelling of oil entering the ocean from subsurface sources, such as drilling well blowouts or pipeline failures. We present a single-phase oil model, devoid of a gaseous component. We designed and implemented a new Python-based near-field plume model, where buoyant oil forms a coherent plume by maintaining a self-similar structure along the vertical upliftings. One of the original contributions of this thesis is the coherent definition of the essential plume variables and the equations of the coupled water-oil system. The near-field component is based on an integral Lagrangian elements plume model and is validated using laboratory-scale and real-scale experiments in the North Sea. A sensitivity analysis on the experimental coefficients characterising the entrainment has been developed, achieving a good fit with in-situ data.

After the plume reaches a terminal level—due to loss of momentum from the source and loss of buoyancy due to ocean stratification—a far-field stage ensues, characterised by the dispersion of individual oil droplets by ocean currents and eddy-turbulence. The far-field initial condition is the final state of the near-field, where the plume element dissolves into oil parcels. The near field oil and water mixture at the terminal level is seamlessly connected to the horizontal and vertical spreading of the mixture. The far-field component is based on a Lagrangian Particle Tracking model (OceanParcels), where we incorporated a vertical component into the basic advection-diffusion problem. Size-dependent buoyancy results in the

formation of distinct clusters with varying resurfacing times.

The newly created plume model and the far-field model, both Python-based, are unified under the name UWORM (UnderWater Oil Release Model). Both the near- and far-field components use as input 3D ocean state data provided by the Copernicus Marine Service (currents velocity, temperature, and salinity fields). Uncertainties in the two modelling components are discussed and highlighted for future work. In the near-field phase, uncertainties primarily concern the choices made for the entrainment parametrisation, as well as the input ocean data. It is shown that ocean currents play a role in the plume's trajectory while stratification influences the terminal level. In the far-field, uncertainties include the resolution of input ocean currents and the chosen eddy diffusivity parametrisation. Moreover, as size impacts the overall buoyancy, the droplet size distribution plays an important role in the total volume of oil resurfaced.

Contents

Abstract i

List of Figures v

List of Tables xi

1 Preface 1

1.1 Marine oil spills: subsurface risk 1

1.2 Thesis objectives and outline 10

2 Literature review of plume models 15

2.1 Introduction 15

2.2 Models based on dimensional analysis 18

2.3 Eulerian models 23

2.4 Lagrangian models 26

2.4.1 Oil and gas in shallow to deep waters 29

2.5 Summary and conclusions 34

3 Modelling underwater near-field oil plume 37

3.1 Introduction 37

3.2 Model equations and variables 42

3.2.1 Seawater entrainment 48

65 3.3 Numerical methods 51
66 3.4 Jet / plume regimes 53
67 3.5 Model validation in laboratory-scale experiments 56
68 3.5.1 Unstratified flowing ambient 56
69 3.5.2 Stratified flowing ambient 59
70 3.6 Model validation in large-scale North Sea exercise 60
71 3.7 Summary and conclusions 71

72 **4 Far-field modelling and linking near-far field dynamics** **73**
73 4.1 Introduction 73
74 4.2 Lagrangian Particle Tracking for oil spills 75
75 4.3 Coupling near and far-field dynamics 79
76 4.3.1 Droplets buoyant velocity 82
77 4.3.2 Droplets size distribution 84
78 4.4 Deep-release scenario in the Southern Adriatic Sea 88
79 4.5 Summary and conclusions 101

80 **5 Conclusions and perspectives** **103**

81 **Appendices** **109**
82 A.1 Forced Entrainment computation 109
83 A.2 Plume model numerical discretization 113
84 A.3 Diagnosed ocean vertical velocity 117

85 **Bibliography** **121**

86 **Acknowledgements** **141**

List of Figures

1.1 Number of medium (7-700 tons) and large (>700 tons) tanker spills within 1970-2022. 4

1.2 Offshore oil and gas platforms (red areas), data from Lujala et al. (2007), mapped through QGIS software. 5

1.3 **a**, Offshore marine pipeline infrastructure of British domain in the North Sea, from data in (NSTA, 2023); **b**, Offshore marine pipeline infrastructure in the Gulf of Mexico, from data in (NOAA, 2023); plotted with ARCGIS. 7

1.4 Schematic representation of a subsurface spill event with typical length L and time T scales. The near-field region ($L \sim$ 10-500 m, $T \sim$ 1-10 min) depicts the collective ascent of oil in a plume, concluding with subsurface intrusion. In the far-field region, individual oil droplets rise to the surface ($L \sim$ 100 m - 10 km, $T \sim$ 1-20 hr). (Premathilake and Khangaonkar, 2019). 12

2.1 Schematic representation of a jet. A global (x, y, z) and local (x', y', z') coordinate systems are defined, with jet velocity $\vec{v}$, density ρ, radius b. The ambient currents $\vec{v}_a$ bend the jet and entrain seawater of density ρ_a. 19

2.2 Drivers acting on a fluid release into another: initial momentum (direction and intensity), buoyancy, column stratification, cross-currents. 20

2.3 Schematic representation of Eulerian model by (Jirka, 2004), where the plume and ambient variables are depicted. 24

2.4 Plume trajectory and envelope simulated with CORJET compared with data from laboratory experiment (Fan, 1967). An inclined buoyant discharge $\theta = 45°$ is eventually trapped due to ambient stratification. Courtesy of (Jirka, 2004) 27

2.5 Plume element with liquid (oil + water) and gas components. Gas is found in inner core or radius βb. Gas bubbles have total volume V^b and the liquid part has volume V^l. 30

2.6 Thermodynamic equilibrium curve for a gas, methane, and a temperature profile for a location in Gulf of Mexico. The hydrate phase is below $z \sim 500$ m, while at shallower depths the hydrate component transforms in free gas. Courtesy of (Zheng et al., 2003). 32

2.7 In deep waters, gas separation from the plume occurs as it is bent by strong cross-currents. Depending on their density and size, bubbles rise separately from the plume. Courtesy of (Socolofsky and Adams, 2002). 33

3.1 The plume is modelled as a series of independent cylinders, with diameter $D = 2b$ and thickness h. In a global cartesian coordinate system, $\vec{v}_0$ is the release velocity, and $\vec{v}_a$ is the ambient ocean velocity. In a local spherical coordinate system, each cylinder velocity is $(|\vec{v}|, v_\theta, v_\phi)$. 42

3.2 Numerical scheme workflow. The release variables serve as initial condition. At each time-step, the 10 prognostic equations and 5 diagnostic equations are solved. The ambient ocean profiles are interpolated at the cylinder depth and inserted in the equations. With the oil and entrained seawater density calculated from T and S, the density of the oil and water mixture is obtained. Finally, the reduced gravity and the entrainment coefficient are updated. . . . 52

3.3 UWORM-1 simulation (solid lines) and laboratory data (markers) are compared in flowing unstratified ambient water. In **a** the x-z trajectories, in **b** the oil concentrations. The ambient parameters and release conditions in Table 3.4. 58

3.4 UWORM-1 simulation and laboratory data are compared in stratified ambient water. The simulated maximum height of rise is compared with the experimental value. 60

3.5 In **a**,**b** the ambient vertical profiles of seawater density, temperature, and salinity at the location and time of the oil release at the Frigg Field from the Copernicus Marine Service reanalysis fields. In **c**, the ocean velocity vertical profile, which vary over time. The depicted velocity components profiles are interpolated at 08:13 local time. . 61

3.6 North Sea Experiment: the neutral buoyancy level is linked to reduced gravity $\rightarrow 0$ (red) and the maximum height with $w \rightarrow 0$ (blue). 64

3.7 North Sea Experiment: in **a** the plume envelope, in **b** the plume centerline position in time. A comparison between simulations (UWORM-1 in black and (Yapa et al., 1999) in red) and data (green) is shown. Observed terminal range (grey). 65

3.8 North Sea Experiment: Plume diameter comparison between UWORM-1 and data. With the entrainment coefficient in (Yapa et al., 1999) diameter is underestimated. 66

3.9 North Sea experiment calibration: the shear (orange-purple) component can be tuned via the entrainment coefficient α, while the forced (black) component is fixed. 67

3.10 North Sea Experiment calibration: in **a**, the plume envelope, in **b**, the plume centerline position in time. Again, a comparison between UWORM-1 (black), data (green) is displayed. With calibration, the plume entrains more water, resulting heavier and slower. 69

3.11 North Sea Experiment calibration: comparison of plume diameter from UWORM-1 and data. Augmented plume width. 70

4.1 Ocean vertical velocity in the Mediterranean Sea, computed from the horizontal velocity components through the continuity equation for August 1,1995 retrieved from Copernicus Marine Service (Coppini et al., 2023). 79

4.2 Initial particles position: (left panel) uniform distribution, (right panel) normal distribution. The plume final radius is marked in red. 81

4.3 Customary drag coefficient for spheres as a function of the Reynolds number, from (Duan et al., 2015). The transition from a laminar to a turbulent regime is for $Re \sim 3 \cdot 10^5$. 83

4.4 Diagram showing different initial volume fluxes (see colour legend) and nozzle diameters (Johansen et al., 2013) Different Ohnesorge and Reynolds numbers are obtained, with a transition between laminar and turbulent flow (solid diagonal line). On the bottom right, the DeepSpill experiment. 86

4.5 Summary of observed cumulative droplet size distributions of five different data sets, with the associated lognormal and Rosin-Rammler distribution fits to the droplet size data. (Li et al., 2017). 87
4.6 Offshore crude oil installations in the Adriatic Sea area. In purple, the dismissed platforms, in blue, the ones operational. Off Brindisi coast, the selected site Aquila 2 ENI platform (40.93018 ^{o}N 18.32711 ^{o}E). Courtesy of Emodnet. 88
4.7 Schematics of the Adriatic Sea surface circulation from (Artegiani et al., 1997). 89
4.8 Ambient profiles of seawater temperature, and salinity (**a**), and density (**b**), on 01/08/1995 from interpolation at the release location. 91
4.9 Ambient profiles of zonal and meridional velocity components (**a**), and upward vertical component (**b**), on 01/08/1995 from interpolation at the release location. The vertical velocity is computed diagnostically. 92
4.10 Southern Adriatic Sea near-field simulation: zonal (**a**) and meridional (**b**) transects of plume envelope and center-line trajectory. In (red), the depth of neutral buoyancy, in (blue), the maximum height of rise. 95
4.11 Southern Adriatic Sea near-field output: the evolution in time for (**a**), reduced gravity (solid red) and plume vertical velocity (solid blue), for (**b**), oil mass fraction c (dashed red) and vertical position (solid black). See correspondence with Figure 4.10 for neutral buoyancy and maximum rise level. 96
4.12 Southern Adriatic Sea ocean currents from CMEMS (Coppini et al., 2023) on 01/08/1995. In yellow, the final state of the near-field and initial state of the far-field, at depth z = -134 m. 97

4.13 Southern Adriatic Sea near-far field coupling: in **a**, the Droplet Size Distribution according to a log-normal profile. In **b**, the buoyant vertical velocity associated to each size, with small droplets $d < d_c$ and large droplets $d > d_c$. 98

4.14 Far-field simulation in the Southern Adriatic Sea: (**A1-B1**) 15 min, (**A2-B2**) 30 min after end of near-field (black circle); droplet size is colour-coded with the DSD in Fig.4.13; in **B1-B2** ocean currents at z=-55 m and Lat-Lon view of the spill. 99

4.15 Far-field simulation in the Southern Adriatic Sea: (**A3-B3**) 6 hours, (**A4-B4**) 8 hours after end of near-field (black circle); in **B3-B4** ocean currents at z=-55 m and Lat-Lon view of the spill. Smaller particles persist longer subsurface. 100

5.1 Cylinder infinitesimal area dA is calculated from potential stretching S, enlarging of radius Δb and bending Δv_ϕ. The ambient current direction is set by u_a. 112

5.2 **a**, oil mass fraction c; **b**, vertical position z. Comparison between the Euler (purple) and RK-IV (green) schemes. The relative error is $\sim 0.5\%$. 116

5.3 Arakawa-C grid used in NEMO model: T indicates scalar points where temperature, salinity, horizontal divergence are defined, (u,v,w) indicates vector points, and f indicates vorticity points. Adapted from NEMO v4.3 manual (Gurvan et al., 2022). 117

5.4 Computed vertical velocity depth profiles, for two different locations in the Mediterranean Sea. In orange, the one given by NEMO, in blue, the one computed through the algorithm described. Maximum discrepancy is $\sim 10^{-6}$ m/s. 118

List of Tables

1.1 The average annual contribution of main sources of petroleum in kilotons per year (ktons/yr) entering worldwide marine waters for the years 1975-1999 (Polinov et al., 2021). 3

1.2 Major oil spills due to tanker accidents from 1976 to 2022, data from (ITOPF, 2022). 3

2.1 Initial release and ambient variables of the Deepwater Horizon accident: b_0, v_0 by Camilli et al. (2012), z_0 by Camilli et al. (2010), other variables by Socolofsky et al. (2011). 21

2.2 Deepwater Horizon regimes calculated with dimensional analysis for the oil component only, neglecting the gas interaction. 22

2.3 Primary subsurface blowout models include CORMIX (dimensional analysis), CORJET (Eulerian), JETLAG (Lagrangian), and CDOG, DEEPBLOW (multi-phase for deep-water). 35

3.1 The fifteen prognostic and diagnostic plume element variables: mass, oil mass fraction, 3D velocity, density, oil density, entrained water density, oil and water mixture density, temperature, salinity, 3D position, thickness, and radius. 43

3.2 Ambient ocean variables, considered as input to the plume model: ocean water density, 2D ocean currents velocity, oil mass fraction, ocean temperature, salinity and stratification identified by the Brunt-Väisälä frequency square. 43
3.3 Shear entrainment optimal empirical parameters obtained from Yapa and Li (1997). 50
3.4 Seven experiments in unstratified (ρ_a = const) flowing ambient. Data from Fan (1967). The discharge parameters and ambient variables are indicated, together with the jet-plume scale and the jet-currents scale. 57
3.5 Fourteen experiments were performed in a stratified flowing ambient. Data from Wright (1977a,b). The initial discharge variables and ambient paramters are shown, alongside with L_{max} from dimensional analysis and the experimental value $L_{max-exp}$. 59
3.6 North Sea experiment initial release variables and ambient ocean conditions. 62
3.7 Transition scales and intrusion levels from the NOFO Experiment are compared with dimensional analysis and UWORM-1 output. 63

4.1 Release and ocean variables: depth, nozzle radius, velocity, initial oil density, buoyancy, stratification, Froude number, total spill duration and oil volume. 91
4.2 Summary of initial state, intermediate (end of near and start of far field) and final state. 93

Chapter 1

Preface

This thesis endeavors to contribute to the field of oil spill studies in the ocean, focusing specifically on subsurface accidents. Before delving into the complexities of subsurface spill modelling, Section 1.1 provides a comprehensive overview of oil spill pollution at sea, both surface and subsurface. In Section 1.2 the thesis objectives and outline are presented.

1.1 Marine oil spills: subsurface risk

Oil plays a crucial role in climate change. Globally, the oil industry significantly increases greenhouse gas emissions, while locally, accidental oil spills exacerbate marine environmental degradation. The problem of oil pollution in marine environments, along with its regulatory framework, has a long history. From 1907 to 2014, more than 7 million tons of oil were discharged into the environment through over 140 significant spills, resulting in economic, environmental, and public health issues (Etkin and Welch, 1997). Originating in 1954, the primary global framework addressing oil pollution from ships is the International Convention for the Prevention of Pollution from Ships, MARPOL 73/78 (IMO, 1983). Notably, Annex

I (Regulations for the Prevention of Pollution by Oil) has played a pivotal role in averting oil pollution, with the 1992 amendments mandating double hulls for new oil tankers. Recognising the urgent need to preserve marine life, the United Nations (UN) 2030 Agenda for Sustainable Development has incorporated the conservation of ocean life and the prevention of marine pollution, including oil, into Sustainable Development Goal 14, "Life Below Water" (UN, 2015).

Despite concerted efforts, oil continues to infiltrate the world's oceans through various channels, including shipping, ship-based activities, accidental spills, intentional discharges, land-based sources and natural oil seeps (NA, 1985). This results in ecological damage, ranging from immediate catastrophic effects to longer-term, lethal impacts. Over the years, different institutions have acknowledged the imperative to assess the overall volume of oil injected into the ocean. Several databases have been built, both at regional (in the Mediterranean area (EMSA, 2021), (REMPEC, 2018)) and global scale (ITOPF, 2022). The relative significance of primary sources, such as leaking pipelines, tanker collisions, and blowouts from drilling rigs, has experienced shifts. Furthermore, military operations and natural disasters like earthquakes and hurricanes have emerged as notable sources of oil spills, presenting a threat to various infrastructures, including oil refineries, power plants, fuel containers, and pipeline networks. The average estimated total oil entering worldwide marine waters for the years 1975-1999 was $\sim$1,271 ktons/yr, where the distinction by source type is provided in Table 1.1 (Polinov et al., 2021).

Oil spill modelling in the ocean focuses on spills associated with petroleum transportation, ranging from tanker accidents (primarily resulting in surface spills) to pipeline failures (occurring either at the surface or subsurface) and spills related to petroleum extraction (occurring beneath the surface). Apart from naturally caused spills and human caused illegal discharges, tankers have historically been the predominant sources of oil spills. Incidents related to tanker accidents are extensively documented. On the other hand, comprehensive databases for pipeline

Source		ktons/yr	%
Natural Seeps		600	47%
Extraction of petroleum		38	3%
Transportation of petroleum	Pipelines	12	1%
	Tankers	100	8%
	Illegal discharges	36	3%
	Others	5	0%
Consumption of petroleum	Illegal discharges	281	22%
	Others	199	16%
Total		1271	100%

Table 1.1: The average annual contribution of main sources of petroleum in kilotons per year (ktons/yr) entering worldwide marine waters for the years 1975-1999 (Polinov et al., 2021).

failures and blowouts are not readily accessible. Blowout accidents, in particular, are rare events, even though they may involve high spillage volumes.

Data on tanker spills is shown in Figure 1.1, with an overall reduction in the number of medium (7-700 tons) and large spills (> 700 tons). The most significant tanker-related accidents worldwide since 1967 are reported in Table 1.2.

Year	Vessel	Location	Tons
1979	Atlantic Empress	Tobago, West Indies	287,000
1991	Castillo de Bellver	Angola	260,000
1978	Amoco Cadiz	Brittany, France	223,000
1991	Haven	Genoa, Italy	144,000
1988	Odyssey	Nova Scotia, Canada	132,000
1967	Torrey Canyon	Scilly Isles, UK	119,000
2018	Sanchi	East China Sea	113,000
1996	Sea Empress	Pembrokeshire, Wales	72,000
2002	Prestige	Galicia, Spain	63,000
1989	Exxon Valdez	Gulf of Alaska	37,000

Table 1.2: Major oil spills due to tanker accidents from 1976 to 2022, data from (ITOPF, 2022).

Since the 1980s, there has been a significant reduction in the total discharged oil for incidents related to tankers (ITOPF, 2022). While the overall count of spill events has remained relatively stable, the amount of oil released in each individual spill has decreased. This positive trend can be attributed to both a reduced number of tanker accidents and improved security measures. These measures include the Global Positioning System (GPS) for vessel tracking and the "Double Hulls" convention adopted by the IMO's Marine Environment Protection Committee in 1992 (Huijer, 2005).

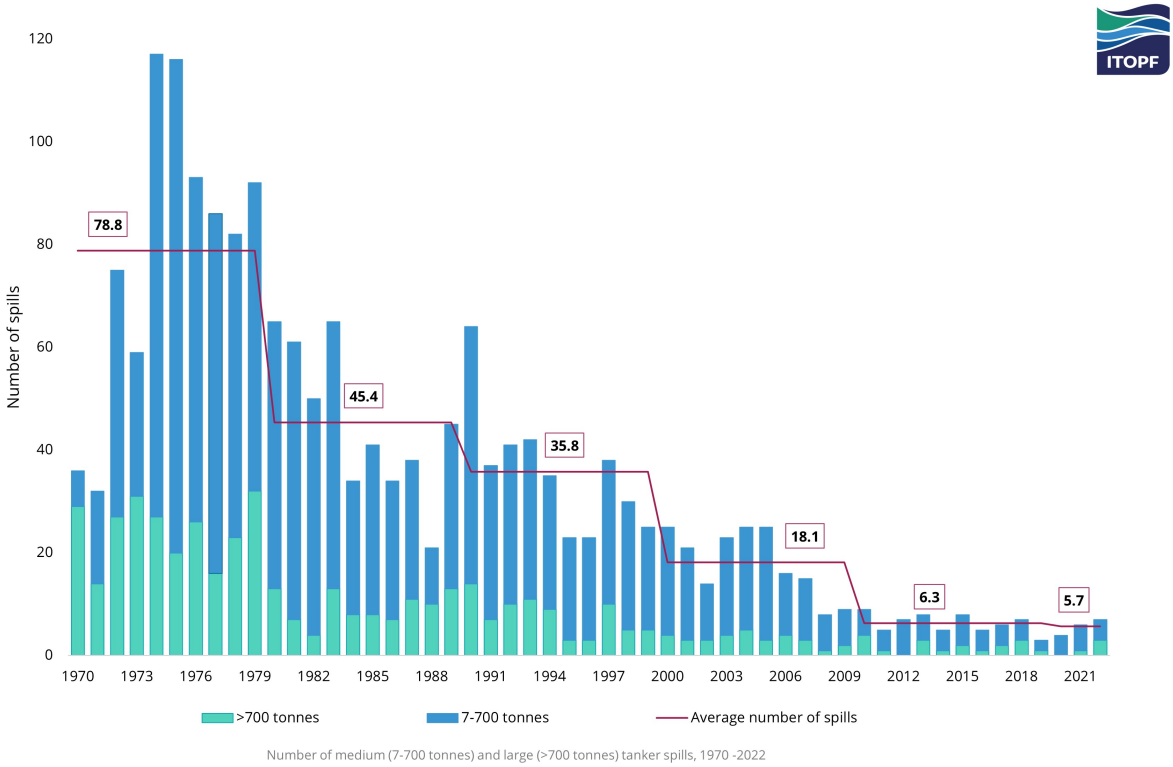

Figure 1.1: Number of medium (7-700 tons) and large (>700 tons) tanker spills within 1970-2022.

As for subsurface oil spills, distinct considerations come into play. The development of offshore oil and gas structures strategically focuses on specific geographic areas that house substantial oil fields. Figure 1.2 illustrates the primary offshore structures in regions such as the Gulf of Mexico, North Sea, areas off California, off

the coast of Brazil, Nova Scotia, and off Atlantic Canada. Approximately 33% of the total global crude oil production originates from offshore sources. In the early 2000's, the global offshore oil and gas industry boasted over 6,500 installations, with 4,000 located in the United States (Gulf of Mexico), 950 in Asia, 700 in the Middle East, and 400 in Europe (Harris, 2016). Regarding the pipelines infrastructure, the preponderance of facilities is concentrated in the North Sea and the Gulf of Mexico (refer to Figure 1.3). According to (GESAMP, 2007), the estimated annual oil discharge from marine pipelines has increased over the past 50 years, with an average 2,800 tons/yr.

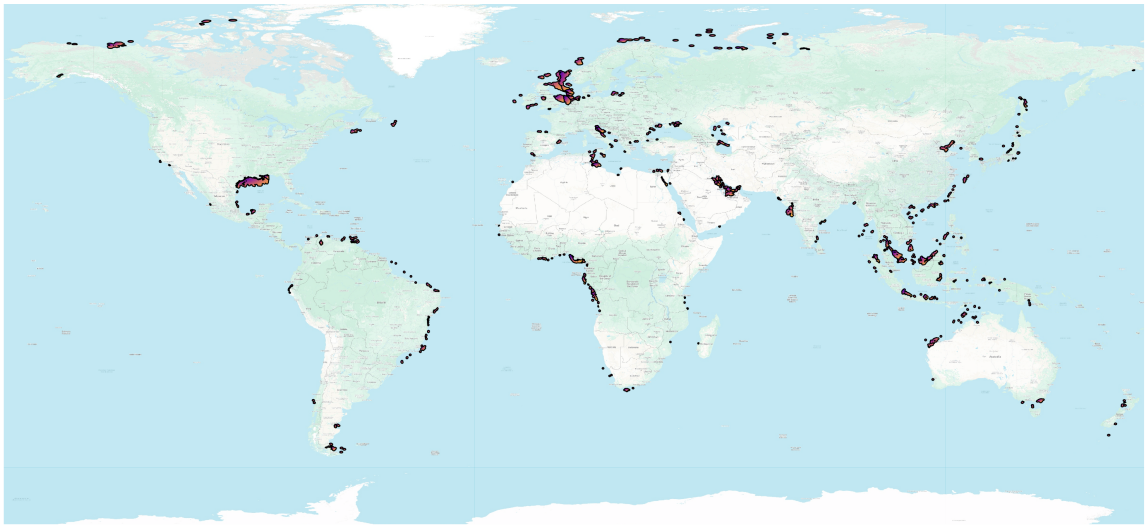

Figure 1.2: Offshore oil and gas platforms (red areas), data from Lujala et al. (2007), mapped through QGIS software.

The rise in pipeline-related spills can be attributed to various factors. Not only the overall pipeline infrastructure has expanded, but aging, inadequate maintenance and military operations played a role. Sabotaging has resulted in increased pollution in regions such as Arctic Russia, Niger Delta, and the Amazon (Jernelöv, 2010). A major spill of 14,000 tons of oil occurred in Tarut Bay, Arabia, in 1970, due to a rupture of a coastal pipeline. Large pipeline spills also occurred in 1998 in both

Nigeria and Brazil. In 2005, more than 22,000 tons of oil were spilled in the Gulf of Mexico and near-shore areas from multiple sources due to Hurricane Katrina. Regarding spills from well blowouts, the estimated annual oil release from offshore exploration and production is approximately 10 times higher than from pipelines ($\sim$ 20,000 tons/yr) (GESAMP, 2007). Furthermore, continuous advancement of technologies related to well exploration and deep-source production has lead to the relocation of rigs to progressively deeper and riskier waters (Kark et al., 2015).

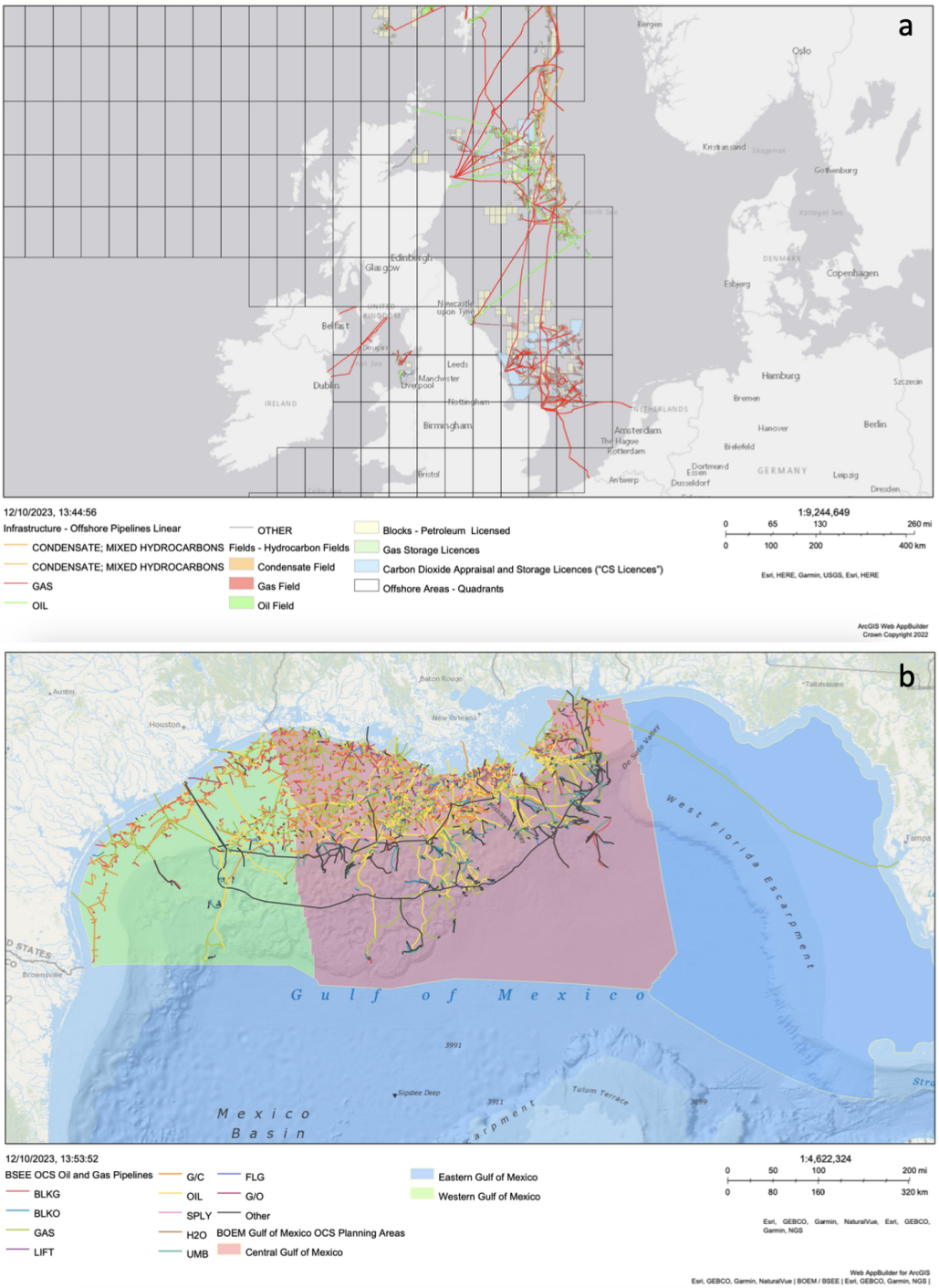

367

Figure 1.3: **a**, Offshore marine pipeline infrastructure of British domain in the North Sea, from data in (NSTA, 2023); **b**, Offshore marine pipeline infrastructure in the Gulf of Mexico, from data in (NOAA, 2023); plotted with ARCGIS.

In fact, even if less frequent, blowout accidents are generally more catastrophic than tanker accidents. In the Gulf of Mexico, two remarkable blowout accidents took place. In 1979, the Pemex (Petróleos Mexicanos) platform exploded while drilling an exploratory well in Bahia de Campeche in the Gulf of Mexico, at a shallow depth of ~ 50 m. The spill from the "Ixtoc I" oil well was capped only nine months later, with a total loss of 475,000 tons oil (Jernelöv and Lindén, 1981). Thirty-one years later, on April 20th 2010, the BP Deepwater Horizon offshore drilling rig exploded, leading to a catastrophic release of oil and gas into the sea. The well position was this time at the remarkable depth of $\sim$ 1500 m (Lehr et al., 2011). The spill lasted 87 days, during which an estimated 690,000 tons of oil went into the ocean, at an average rate of 8,000 tons/d (Camilli et al., 2012). The depth of the discharge and the particular ocean conditions favoured the formation of subsurface intrusion levels, where oil droplets were trapped for months (North et al., 2011).

Success in managing oil spills relies on prompt detection achieved through radars, optical sensors from airplanes and satellites, and on-site measurements (Marta-Almeida et al., 2013). Effective monitoring techniques are crucial for aiding spill remediation by enabling early detection of slicks, assessing oil properties, estimating spill size, and predicting the movement of oil. Another key factor is accurately forecasting the spill evolution over time. Over the last few decades, there has been a growing interest in predicting particle trajectories in the sea, involving both theoretical development (Haller, 2002; Berti et al., 2011) and operational numerical models. This process extends beyond oil to pollution forecasting in general, encompassing plastic (Lange and Van Sebille, 2017; Liubartseva et al., 2018; Zambianchi et al., 2017), as well as biogeochemical cycles (Palatella et al., 2014).

In the framework of oil entering the ocean, numerous models have been developed with the aim of predicting the slick evolution. Notable examples include: Oil Spill

Contingency and Response (OSCAR) (Reed et al., 1995) coupled with the subsurface model DeepBlow from SINTEF (Johansen, 2000), the Spill Impact Model Application Package/Oil Modelling Application Package (SIMAP/OILMAP), coupled with the subsurface model OILMAPDeep (https://www.rpsgroup.com/services/oceans-and-coastal/modelling/oilmap/), the GNOME/ADIOS model, coupled with the subsurface model TAMOC from NOAA (Lehr et al., 2002), the model TESEO (Sotillo et al., 2008; Chiri et al., 2020), the model MOHID (Fernandes et al., 2013), and the model MOTHY (Daniel et al., 2003). Others do not include the subsurface plume component such as the OILTRANS model (Berry et al., 2012) and the MEDSLIK-II model (De Dominicis et al., 2013a,b).

MEDSLIK-II is a community model developed and maintained by an international consortium, with the EuroMediterranean Centre on Climate Change (CMCC) being a member. This open-source model provides predictions on surface advection by currents of variable horizontal resolution, diffusion by sub-grid turbulence, and fate, including evaporation, spreading, and dispersion beneath the surface.

Following detection and forecast, it is necessary to implement countermeasures, which include physical, chemical, and biological interventions (Li et al., 2016). Among chemical measures, dispersants reduce the size of oil droplets, a controversial practice as it facilitates biodegradation but may have long-term effects due to increased particle persistence and dispersant toxicity (Michel, 2008). When applicable, bioremediation accelerates the degradation rate by introducing nutrients, microbes, and/or surfactants and can significantly reduce the volume of oily wastes.

Following the description of historically relevant subsurface accidents, which provides context for this work, we will present an overview of the main physical processes that need to be modelled after a subsurface oil release, along with the thesis motivation.

1.2 Thesis objectives and outline

Following a subsurface oil spill, it is imperative to address specific inquiries, including the determination of the location and timing of oil emergence at the surface, as well as establishing the likelihood of such occurrences. The objective of this work is to design and implement a new numerical model for subsurface oil releases, aiming to provide comprehensive answers to these critical questions. In a recent review by Socolofsky et al. (2016), the modelling of subsurface spills encompasses multiple aspects, each constituting a distinct field of research and presenting its own unique challenges:

- Oil droplets size distribution
- Near-field plume dynamics
- Intrusion layer formation
- Far-field oil evolution

Upon discharge, the formation of oil droplets depends on inflow characteristics and ambient conditions (Figure 1.4). Subsequently, oil droplets ascend in a coherent and self-similar structure during the near-field phase. Generally, oil droplets and gas bubbles form a multi-phase plume. Additionally, double plumes are commonly seen in stratification, featuring an inner rising flow and an outer descending flow. Initiated by the combined effects of pressure-driven release momentum and buoyancy, the plume continuously entrains ambient seawater through turbulent shear vortices at its edge, which alters the overall buoyancy. The plume also entrains water due to the transport by currents, which simultaneously affects the plume's momentum and causes bending. In scenarios of ocean stratified conditions, the near-field phase could end at a terminal level under the surface. Conversely, in shallow waters or under weak stratification, the near-field region could extend to

the ocean surface. The near-field terminal level marks the transition to a far-field regime. The volume of oil and water mixture is then represented by different size droplets that are subject to advection and diffusion by ocean currents and size-dependent buoyancy. Thus, the droplet size distribution does not impact the near-field phase, while becomes critical in the far-field phase.

The aim of this work is to design a new plume model for subsurface releases, for which a theoretical framework is established. The lack of such a framework halted the definition of a full set of equations to describe the near-field evolution of an oil and water mixture. The evolution follows a set of coupled prognostic (5) and diagnostic (10) equations for the essential model variables. This framework allows for a new analytical definition of the terminal level and better parametrisations of entrainment, which is a key process in the near-field evolution.

The final outcome of this work is an open-source Python-based near-field model that can be easily adapted to different subsea spill scenarios and coupled with far-field advection diffusion models (e.g., Medslik-II). To our knowledge, this capability is not currently available. For the sake of completeness, we included in this work the other three aspects discussed in Socolofsky et al., 2016. In this thesis, our near-field model is coupled with the far-field (subsurface) advection-diffusion model, which is a Lagrangian Particle Tracking model so-called OceanParcels. The coupling between the near and far fields is implemented, and buoyancy behaviour is added to the oil parcels according to a realistic droplet size distribution. From the work done in this thesis, a complete simulation from a subsurface spill to the ocean surface can thus be performed.

Both the plume model and the Lagrangian particles model are driven by the ocean fields (currents, temperature and salinity) from the Copernicus Marine Service products.

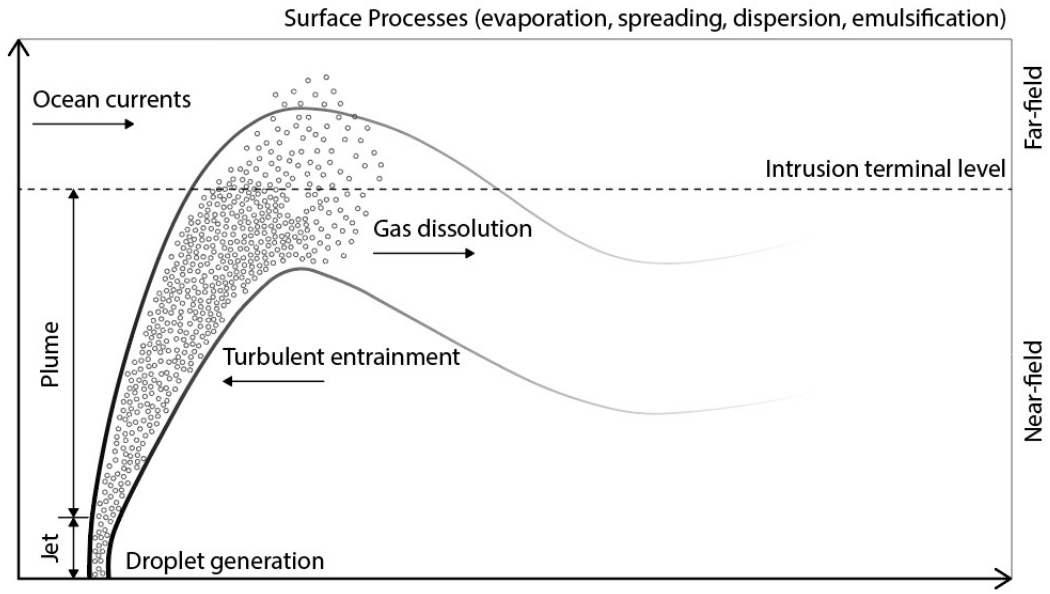

Figure 1.4: Schematic representation of a subsurface spill event with typical length L and time T scales. The near-field region ($L \sim$ 10-500 m, $T \sim$ 1-10 min) depicts the collective ascent of oil in a plume, concluding with subsurface intrusion. In the far-field region, individual oil droplets rise to the surface ($L \sim$ 100 m - 10 km, $T \sim$ 1-20 hr). (Prematilake and Khangaonkar, 2019).

This work is organised as follows. Chapter 2 provides a comprehensive review of state-of-the-art near-field plume models. These models, rooted in dimensional analysis techniques or resolving fluid dynamics equations through Eulerian or Lagrangian formulations, are critically examined.

In Chapter 3, we introduce the near-field plume Lagrangian model. The chapter delves into the model's variables and equations, introducing a novel definition for the oil and water mixture state equation. We explore shear and forced entrainment formulations, emphasising their distinct roles in plume evolution. A numerical workflow has been implemented to solve governing equations and update relevant parameters. The plume encounters various regimes, in alignment with existing literature. Model validation is achieved through both laboratory-scale data and a real-case scenario.

Chapter 4 delves into the far-field stage, presenting the coupling between the near-field plume phase and the far-field advection-diffusion phase. This allows for the resurfacing forecast of the spill, predicting the time and location of slicks. The concluding case study, in the final section, focuses on a hypothetical well blowout event in the Adriatic Sea. The simulation encompasses both near and far-field dynamics, providing realistic results.

Chapter 2

Literature review of plume models

2.1 Introduction

The hydrodynamics of effluent continuously discharging into a receiving body of water can be comprehensively understood by considering two distinct regions: the near-field and the far-field. In the near-field region, located close to the release point, the initial jet characteristics, including momentum flux, buoyancy flux, and outfall geometry, significantly influence the trajectory and mixing of the turbulent plume (Lee et al., 2003; Yapa and Li, 1997; Doneker et al., 1990; Milgram, 1983). As the turbulent plume travels away from the source, entering the far-field region, the influence of the source characteristics diminishes, and external conditions in the ambient environment take control of the plume's trajectory and dilution (Socolofsky et al., 2008). This far-field region is characterised by buoyant spreading motions and passive diffusion due to ambient turbulence (Yapa et al., 1999). In the transition between the near and far fields, intermediate lateral spreading occurs (Akar and Jirka, 1994).

Within the near-field phase, discharged particles, such as oil droplets and gas bubbles, rise collectively in a coherent structure known as the "jet" stage. This phase

is primarily driven by the initial pressure discharge momentum. Subsequently, in the“plume” stage, buoyancy becomes a secondary source of momentum, dominating both in time and space. The seamless transition between the jet and plume stages allows the term “buoyant jet” to be interchangeably used.

Immediately after the discharge, the jet flow becomes unstable at its boundary and breaks down into turbulent motion (boundary-layer nature of the flow). The shear between the two interacting fluids leads to the formation of mixing and turbulent eddies, with the size typically increasing with distance from the source. This favours the entrainment of ambient water into the plume, affecting overall pollutant dilution, momentum, and determining the trajectory (Morton et al., 1956). The interaction with the boundary ambient water, ambient ocean currents, and water column stratification also determines the evolution. All these factors contribute to the final asymptotic state, deciding whether the plume will reach the surface or be trapped at some depth.

The coherent structure observed in buoyant plumes within the near-field has led to the adoption of “integral ” models within the scientific community. Rather than individually describing oil droplets and gas bubbles, these models provide a coarse-grained perspective on their collective behaviour. The foundation of these models rests on the assumption that jet properties, such as velocity and pollutant concentration, maintain a self-similar structure along the jet trajectory, allowing for integral representation. As a marginal note, the self-similarity hypothesis applies after a certain distance from the release point. If D is the nozzle diameter, the Zone Of Flow Establishment (ZOFE $< 10\ D$), represents a region where the flow still exhibits unsheared profiles, and steady turbulent flow has not been established. Empirical observations indicate that within the ZOFE, cross-sectional profiles of plume properties (axial velocity, density, pollutant concentration) are chaotic, while in the Zone of Established Flow (ZOEF $> 10\ D$), a bi-variate Gaussian profile emerges (Doneker et al., 1990; Lee et al., 2003).

This chapter provides a comprehensive review of near-field integral plume models. While the initial models classified plume motion based on dimensional analysis assumptions, state-of-the-art models solve a parametrisation of the overall fluid dynamics equations, reducing the 3D problem to a 1D problem. These generations of models apply a parameterisation to the two-fluid dynamics by treating the plume as an integral object that interacts with the ambient environment, entraining sea-water along its evolution.

Nonetheless, integral models have some limitations, such as simulating the detrainment of oil out of the plume. Although this work does not delve into this framework, it is worth mentioning that Large Eddy Simulation (LES) has been applied to oil and gas plumes (Yang et al., 2016a,b). Unlike integral models, LES models do not rely on self-similarity. Instead, they use Computational Fluid Dynamics (CFD) techniques to solve hydrodynamics equations for the two fluids, incorporating closure assumptions for small-scale turbulent processes.

This chapter is dedicated to oil plume models and is structured as follows. In Section 2.2, we describe models based on dimensional analysis. Then, we focus on integral single-phase models: in Section 2.3, we review plume integral models in the Eulerian framework, and in Section 2.4, we examine them in the Lagrangian framework. In Section 2.4.1, we discuss the basic features of oil and gas models (double-phase), covering shallow to deep-water conditions. Finally, a schematic summary of the discussed plume models is given in Section 2.5.

2.2 Models based on dimensional analysis

Some modelling strategies involve the classification of plume evolution into different outcomes, based on information about initial and boundary conditions. One of the pioneering models employing this approach is CORMIX (Doneker et al., 1990), which utilises dimensional analysis techniques. See for example (Panos and John, 1988). We introduce dimensional analysis applied to plume problems, offering a general method to predict plume behaviour and provide insights into the evolution from initial and ambient conditions. It serves as a versatile first approximation applicable to any subsurface oil spill event. Insights into dimensional analysis are in Chapter 3.

As in Figure 2.1, we define a local coordinate system along the jet trajectory, where the velocity is $\vec{v}$, the jet density is ρ, the density difference with the ambient fluid is $\Delta\rho = \rho_a - \rho$, where ρ_a is the ambient fluid density. The ambient ocean currents are $\vec{v}_a$ and stratification is expressed through the Brunt-Väisälä frequency $N^2 = -\frac{g}{\rho_a}\frac{d\rho_a}{dz}$, where g is the gravitational acceleration and z the depth, defined as in Figure 2.1. These properties allow to define the volume flux Q, the momentum flux M and the buoyancy flux B along the trajectory, where A is the cross-sectional area of the plume and $\hat{n}$ is the normal versor:

$$Q = \int_A \left(\vec{v}\cdot\hat{n}\right) dA \tag{2.1}$$

$$M = \int_A \rho\vec{v}\left(\vec{v}\cdot\hat{n}\right) dA \tag{2.2}$$

$$B = \int_A \Delta\rho/\rho_a \; g\left(\vec{v}\cdot\hat{n}\right) dA \tag{2.3}$$

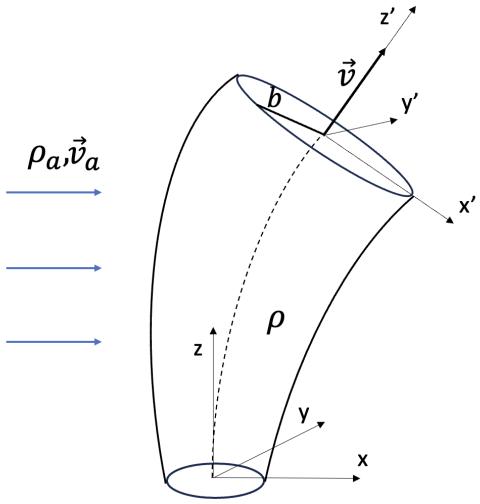

Figure 2.1: Schematic representation of a jet. A global (x, y, z) and local (x', y', z') coordinate systems are defined, with jet velocity $\vec{v}$, density ρ, radius b. The ambient currents $\vec{v}_a$ bend the jet and entrain seawater of density ρ_a.

Assuming uniform flow distribution at the release nozzle of radius b_0, we can write the initial conditions for the fluxes:

$$Q_0 = v_0 \pi b_0^2 \tag{2.4}$$

$$M_0 = Q_0 v_0 \tag{2.5}$$

$$B_0 = Q_0 \Delta\rho / \rho_a g \tag{2.6}$$

Any variable Φ, such as the jet velocity or density or pollutant concentration depends on a limited set of variables related to the initial and boundary conditions (Socolofsky and Adams, 2002) :

$$\Phi = f(Q_0, M_0, B_0, v_a, N^2, z)$$

Assuming that the entrainment is proportional to the distance z (Lee et al., 2003), the velocity in the jet phase is dependent, by definition, on the release momentum and distance from the source: $v_J = g(M_0, z)$. A dimensional analysis of the involved variables leads to the jet velocity in terms of power laws $v_J \propto M_0^{1/2} z^{-1}$. A similar

approach determines the velocity in the plume phase $v_P \propto B_0^{1/3} z^{-1/3}$. A buoyant plume is generally driven by a limited set of factors. These drivers are the initial release momentum (intensity and direction), the buoyancy, the ambient ocean currents and stratification effects, as shown in Figure 2.2.

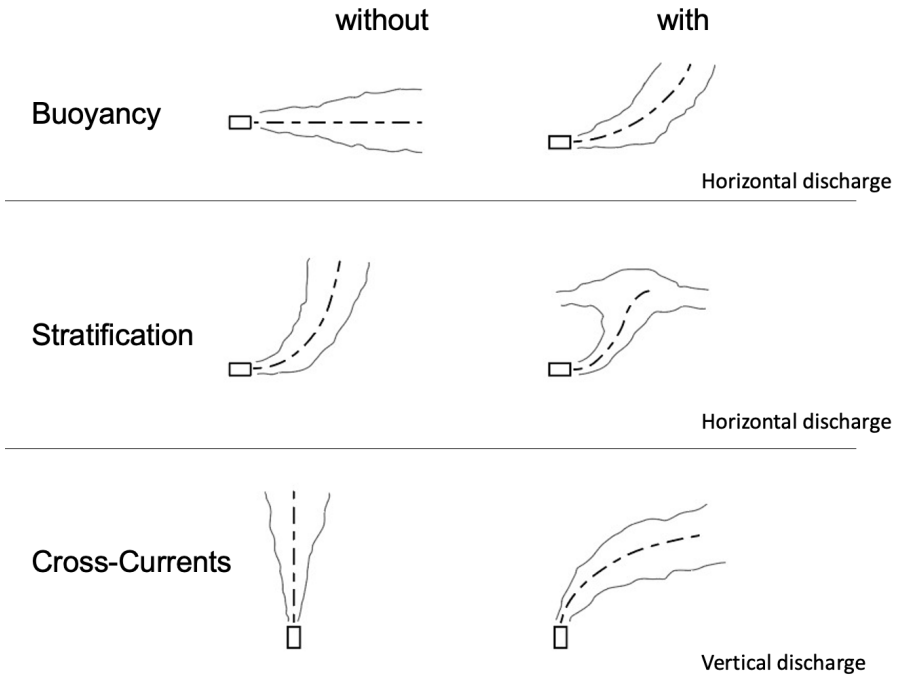

Figure 2.2: Drivers acting on a fluid release into another: initial momentum (direction and intensity), buoyancy, column stratification, cross-currents.

Each driver is responsible for a specific regime in jet-plume evolution. As previously noted, a jet momentum-driven phase is typically succeeded by a plume buoyancy-driven phase. Subsequently, the dominance of stratification effects or cross-current effects depends on their respective intensities. We can determine the transition

heights from one regime to another via dimensional analysis:

$$L_{JP} \propto M_0^{3/4} B_0^{1/2} \quad \text{Jet-Plume transition} \tag{2.7}$$

$$L_{JA} \propto M_0^{1/2} / v_a \quad \text{Jet-Ambient Currents transition} \tag{2.8}$$

$$L_{PA} \propto B_0 / v_a^3 \quad \text{Plume-Ambient Currents transition} \tag{2.9}$$

$$L_{JS} \propto M_0^{1/2} N^{-1/2} \quad \text{Jet-Stratification transition} \tag{2.10}$$

$$L_{PS} \propto B_0^{1/4} N^{-3/4} \quad \text{Plume-Stratification transition} \tag{2.11}$$

It is experimentally found that the end of the plume regime due to stratification is $L_{PS} = 4\, B_0^{1/4} N^{-3/4}$.

We show how dimensional analysis can be applied to the Deepwater Horizon spill. The spill consisted of both gas (23%) and oil (77%) (Camilli et al., 2012), however data for the oil component is available in literature. With the purpose of applying this method, we consider a similar DWH but with oil only, assuming that the oil-gas interaction is negligible. This is not a realistic assumption on the DWH spill (where the gas actually increased the overall plume buoyancy), but we find it useful to show potential application and comparison with real oil-and-gas data.
The initial and boundary conditions relatively to the broken riser source and the oil component are in Table 2.1. The oil release velocity v_0-oil is calculated from the oil volume flux $Q_{oil} = 0.074\,\mathrm{m^3 s^{-1}}$ and the broken riser radius b_0 (Camilli et al., 2012).

z_0(m)	$2b_0$(m)	v_0-oil(m s^{-1})	ρ_{oil}(kg m^{-3})	ρ_{a0}(kg m^{-3})	v_a(m s^{-1})	N^2(s^{-2})
-1500	0.53	0.34	858	1027.8	0.078	$4 \cdot 10^{-6}$

Table 2.1: Initial release and ambient variables of the Deepwater Horizon accident: b_0, v_0 by Camilli et al. (2012), z_0 by Camilli et al. (2010), other variables by Socolofsky et al. (2011).

The relevant undergone regimes during the spill were: a jet phase ($0 < z < L_{JP}$), a plume phase ($L_{JP} < z < L_{PS}$) and a current phase ($z > L_{PA}$). The relative scales

calculated from dimensional analysis inserting the DWH variables are shown in Table 2.2.

In the DWH, the observed jet regime was ~ 0.6 m (Camilli et al., 2012) while

L_{JP}(m)	L_{PS} (m)	L_{PA}(m)
0.18	249	256

Table 2.2: Deepwater Horizon regimes calculated with dimensional analysis for the oil component only, neglecting the gas interaction.

a plume regime, buoyancy dominated, sustained for the first hundreds meters. The ocean currents were relatively weak and did not have a role in shaping the plume motion. The end of the oil and gas plume regime was due to stratification and a large intrusion formation was observed at depths $\sim 1000 - 1200$ m (Camilli et al., 2012; Socolofsky et al., 2011). According to our analysis, without the gas component (which increases the overall plume buoyancy), the plume-stratification transition would have been $L_{PS} \sim 250$ m and the plume would have intruded at depths ~ 1250 m.

Dimensional analysis is a powerful tool to retrieve preliminary information on a subsea spill. The Cornell Mixing Zone Expert System (CORMIX) (Doneker et al., 1990) is based on such transition scales, assessing submerged single-port discharges. CORMIX2 extends this capability to submerged multiport diffusers. The tool predicts plume concentration and width based on discharge and ambient water properties. In its initial version, this model assumed conservative pollutants, neglecting reactions like biodegradation. The updated version accounts for non-conservative and positive/negative buoyant discharges. It is a steady-state model with a constant ambient current along the x-axis. CORMIX relies on a classification system to predict plume characteristics and the final state of evolution (position, width, pollutant concentration). It categories flows into 13 outcomes, The model also provides a rough approximation of the spreading layer and far-field region.

2.3 Eulerian models

In this section, we provide an overview of integral plume models based on the integration of differential equations, which predict the overall evolution of key quantities over time. These models are primarily categorised into Eulerian and Lagrangian formulations.

Eulerian models initiate from the governing equations of motion and turbulent transport (Reynolds equations), which are integrated along the plume trajectory, typically with a Gaussian hypothesis on cross-sectional distributions. Notably, McDougall (Mcdougall, 1978), Fannelop and Sjoen (Fannelop and Sjoen, 1980), and Milgram (Milgram, 1983) proposed Eulerian models for vertically discharged buoyant jets. Initially, they did not consider possible bending due to the effect of ambient flow, a consideration that was subsequently incorporated into this framework by Schatzmann (Schatzmann, 1979).

Jirka introduced CORJET (Jirka, 2004), an Eulerian model outlining the principles and limitations of integral modelling, which includes verification with laboratory data. We provide a concise overview of CORJET (Jirka, 2004), which predicts the behaviour of a 3D jet in an unbounded ambient environment. Eulerian models solve the hydrodynamics equations for fields in the whole domain (e.g. velocity $\vec{u}(\vec{x},t)$). The model accommodates uniform or stratified density and stagnant or steady current conditions (only along the x-axis), accounting for both positively and negatively buoyant discharges. The entrainment hypothesis is based on the eddy viscosity concept, and the model assumes a steady state of the ambient environment without predicting non-stationary behaviour.

In Eulerian context, the following fields are defined:

- Velocity $\vec{u}(\vec{x},t)$
- Density $\rho(\vec{x},t)$

- Temperature $T(\vec{x}, t)$
- Salinity $S(\vec{x}, t)$
- Pollutant concentration $c(\vec{x}, t)$

The ambient variables are the ocean currents velocity $\vec{u}_a$, the sea-water density ρ_a, the temperature T_a and salinity S_a. The model parameters and variables are represented in Figure 2.3, adopting a local spherical coordinates system (r, θ, ϕ). The main modelling assumption is the self-similarity of cross-sections. In particular,

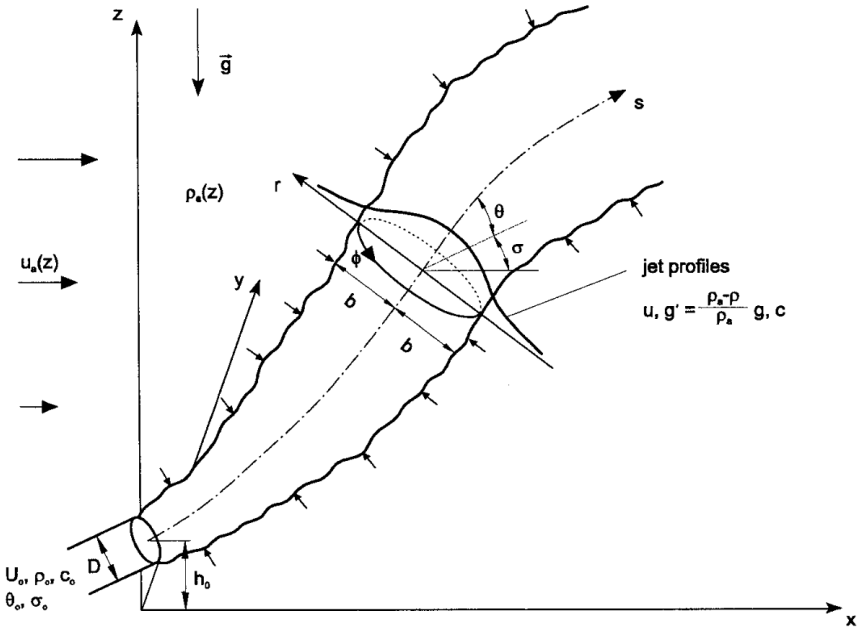

Figure 2.3: Schematic representation of Eulerian model by (Jirka, 2004), where the plume and ambient variables are depicted.

the introduced fields are a priori defined as bivariate Gaussian distributions:

$$u = u_c e^{-r^2/b^2} + u_a \cos\phi \cos\theta \tag{2.12}$$

$$g' = g'_c e^{-r^2/(\lambda b)^2} \tag{2.13}$$

$$T = T_c e^{-r^2/(\lambda b)^2} + T_a \tag{2.14}$$

$$S = S_c e^{-r^2/(\lambda b)^2} + S_a \tag{2.15}$$

$$c = c_c e^{-r^2/(\lambda b)^2} \tag{2.16}$$

where x_c is the centre-line value and $x = \{u, g, T, S, c\}$. In these definitions, the total fields are obtained by adding the ambient component to the jet component. The axisymmetric distribution defines a characteristic radius b, with a dispersion term $\lambda > 1$.

The plume properties change in time according to hydrodynamics, meaning the Reynolds equations. The conservation equations are solved along the jet trajectory $s(\vec{x}, t)$ for specific variables, the fluxes. These fluxes are, from definitions in Eqs. 2.3: the volume flux Q, the axial momentum flux M, the buoyancy flux B, and the temperature Q_T and salinity Q_S fluxes, the oil mass Q_c flux:

$$Q = 2\pi \int_0^R u r dr \tag{2.17}$$

$$M = 2\pi \int_0^R u^2 r dr \tag{2.18}$$

$$B = 2\pi \int_0^R u g' r dr \tag{2.19}$$

$$Q_T = 2\pi \int_0^R u(T - T_a) r dr \tag{2.20}$$

$$Q_S = 2\pi \int_0^R u(S - S_a) r dr \tag{2.21}$$

$$Q_c = 2\pi \int_0^R u c r dr \tag{2.22}$$

where R is the jet edge where boundary conditions should specified. Following Eqs. 2.12 - 2.16, it is usually taken $R \to \infty$. Conservation constraints along the jet

trajectory leads to the following equations of evolution:

$$\frac{dQ}{ds} = E \tag{2.23}$$

$$\frac{d}{ds}M_x = Eu_a + F_D \tag{2.24}$$

$$\frac{d}{ds}M_y = F_D \tag{2.25}$$

$$\frac{d}{ds}M_z = \pi\lambda^2 b^2 g_c' + F_D \tag{2.26}$$

$$\frac{dQ_T}{ds} = -Q\frac{dT_a}{dz}\sin\theta \tag{2.27}$$

$$\frac{dQ_S}{ds} = -Q\frac{dS_a}{dz}\sin\theta \tag{2.28}$$

$$\frac{dQ_c}{ds} = 0 \tag{2.29}$$

where E is a parametrisation of the sea-water inflow due to turbulent entrainment at the boundary. The entrainment is comprised of two primary terms referred to as "stream-wise" and "azimuthal" mechanisms. It is linked to the jet velocity, orientation, the relative influence of momentum to buoyancy, and the ambient water current (Jirka, 2004). A drag force F_D is also considered. The buoyancy flux conservation is not calculated directly, but density is inferred from a particular equation of state: $\rho_c = \rho_c(T_c, S_c)$.

An illustrative CORJET output is shown in Fig. 2.4, depicting a buoyant jet in a linearly stratified stagnant environment, where a final trapping is reached. The simulation is compared with data from laboratory experiments. CORJET has been modified to suit various applications. One example is BrIHne, a model designed for brine discharges from desalination plants (Palomar et al., 2012).

2.4 Lagrangian models

In contrast to Eulerian formulations that observe fluid from a fixed point in space, Lagrangian formulations track fluid elements along their trajectories over time.

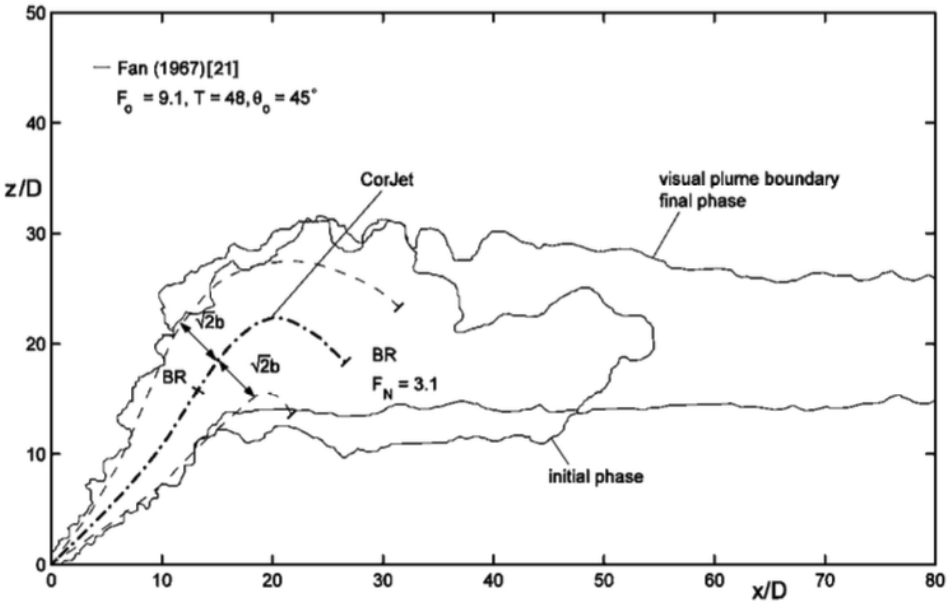

Figure 2.4: Plume trajectory and envelope simulated with CORJET compared with data from laboratory experiment (Fan, 1967). An inclined buoyant discharge $\theta = 45°$ is eventually trapped due to ambient stratification. Courtesy of (Jirka, 2004)

Lagrangian integral models treat the oil plume as a series of non-interfering moving elements. Each jet element is assumed to be advected with some average local velocity along the trajectory. During this advection, the element it undergoes transformation due to sea-water entrainment. The Eulerian and Lagrangian formulations link can be found in (Frick et al., 1994).

Lee and Cheung (Lee and Cheung, 1990) pioneered JETLAG, a model originally designed for wastewater. Over recent decades, Lagrangian plume models have evolved into multi-phase types, addressing potential oil and gas leaks (DEEPBLOW (Johansen, 2000) by SINTEF and the Clarkson Deepwater Oil and Gas model (CDOG) (Zheng et al., 2003), see next section).

Here, we present an overview of the JETLAG model (Lee and Cheung, 1990), which serve as the foundation for our work. This model was developed by Lee and

Cheung based on the work of Winiarski and Frick (Winiarski and Frick, 1976; Frick, 1984). JETLAG represents the 3D plume as a series of non-interfering elements. Grounded in the self-similarity of the plume along its trajectory, a top-hat hypothesis is embraced, assuming constant element properties (e.g. velocity) across cross-sections. This equals treating each element as a cylinder. It considers the ambient ocean current only along the x-axis, and introduces a time-varying entrainment coefficient, thus adapting the turbulent entrainment flow to the jet and ambient ocean conditions.

In (Lee and Cheung, 1990), a discretised formulation is given and the original differential equations are not published. The properties of each plume element at the k-th step are the position (x_k, y_k, z_k), velocity (u_k, v_k, w_k), temperature T_k, salinity S_k and density ρ_k, pollutant concentration c_k. Although this latter being one of the key parameters describing the plume, no definition is provided. The density of the oil-water mixture is calculated from temperature and salinity $\rho_k = \rho(S_k, T_k)$ (Bobra and Chung, 1986), but the explicit function used is not provided. Each cylinder has radius of b_k and thickness of $h_k = 0.1 V_k \Delta t$. Consequently, the mass of each cylinder is $M_k = \rho_k \pi b_k^2 h_k$.

The authors define a discrete increase in mass due to turbulent entrainment ΔM_k, defined as

$$\Delta M_k = \Delta M_f + \Delta M_s$$

being ΔM_s a shear and ΔM_f a forced contributions. The shear flux depends on the velocity shear between the two mixing fluids, while the forced flux is defined under the assumption of an ambient flow on the windward surface of the cylinder. To evaluate this contribution, the authors assume the cylinder is subject to bending, stretching and enlarging. Discrete modification of the other variables are provided in the paper, following conservation principles.

2.4.1 Oil and gas in shallow to deep waters

In (Yapa and Li, 1997), the authors improved the wastewater model JETLAG for oil and gas releases. In their model, the plume again comprises a series of non-interfering cylinders (of radius b and thickness h), adhering to the assumptions of self-similarity and top-hat profiles.

The conservation equations for cylinder mass m, momentum $m\vec{v}$, temperature T, salinity S, and oil concentration c are developed. The set of equations for the oil component only is:

$$\frac{dm}{dt} = \rho_a Q_e - \sum_i \frac{dm_i}{dt} - \frac{dm_d}{dt} \tag{2.30}$$

$$\frac{dm\vec{v}}{dt} = \vec{v}_a \frac{dm}{dt} + m\frac{\rho_a - \rho}{\rho} g\vec{k} - 2\rho bhC_D(|\vec{v} - v_a'|)^2 \frac{\vec{v}}{|\vec{v}|} \tag{2.31}$$

$$\frac{dmX}{dt} = X_a \frac{dm}{dt} - \rho_a K 2\pi bh \frac{X - X_a}{b} \tag{2.32}$$

where in Equation 2.30, $m = \pi b^2 h\rho$ is the element mass, and the ambient variables are defined by the subscript a. Q_e is the entraining water volume flux, $\frac{dm_i}{dt}$ and $\frac{dm_d}{dt}$ are respectively the oil dissolution and diffusion components. Equation 2.31 contains a first term for the entraining water momentum. The second term represents the buoyancy force due to the density difference between the ambient and plume density. The third term is the drag force, proportional to $\propto |v|^2$, with C_D being the drag coefficient. Equation 2.32 is the conservation law for a general variable X, representing T, S, or c respectively. It includes a term for the ambient entrainment and a diffusion term, with K_X being the respective diffusivity. No information is given for the diffusivity choice nor for dissolution mass transfer coefficients. In simulations, the authors neglect the drag force.

The authors modified Eqs. 2.30, 2.31, 2.32 to include a gas component to the system. When gas is present, evidence shows it occupies an inner core of the plume. This core has radius βb, with $0 < \beta < 1$. Typically, gas bubbles exhibit a greater

velocity owing to their higher buoyancy. A constant slip velocity $w_b \sim 0.25 - 0.35$ m/s is the velocity difference between the gas and oil components. The vertical

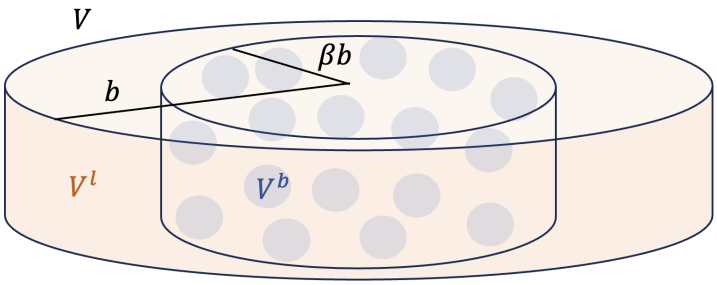

Figure 2.5: Plume element with liquid (oil + water) and gas components. Gas is found in inner core or radius βb. Gas bubbles have total volume V^b and the liquid part has volume V^l.

component of the momentum Equation 2.31 is adapted for gas bubbles (b), and liquid component (l):

$$\frac{d}{dt}[m_l w + m_b(w + w_{b)}] = \tag{2.33}$$

$$= w_a \frac{dm_l}{dt} + \frac{\rho_a - \rho_l}{\rho_l} g\pi b^2 h(1 - \beta^2\epsilon)\rho_l + \frac{\rho_a - \rho_b}{\rho_b} g\pi b^2 \beta^2 h\epsilon\rho_b \tag{2.34}$$

Eq. 2.34 contains the oil $m_l w$ and gas momentum $m_b(w + w_b)$, to which a (constant) slip velocity w_b is added. Two different buoyancies act on the two substances through a weight ϵ

$$\epsilon = \frac{\rho_l - \rho}{\rho_l - \rho_b} \tag{2.35}$$

so that the gas volume is $V^b = \pi b^2 h\beta^2\epsilon$ and the liquid volume is $V^l = \pi b^2 h(1 - \beta^2\epsilon)$, while $V = V^l + V^b$. The model provides the trajectory, envelope, density, oil concentration, temperature and salinity in time.

For deepwater releases, additional complexities arise due to the behaviour of gas under high-pressure and low-temperature conditions. Gas transformations influence buoyancy and, consequently, the overall evolution of the plume. In subsurface

oil and gas modelling, it is common to define shallow (0-100 m), intermediate (100-700 m), and deep waters (700-1500 m) (The discussed model (Yapa and Li, 1997) addresses oil and gas plumes in a shallow environment).

State-of-the-art models for multiphase plumes in deepwater blowouts are the Clarkson Deepwater Oil and Gas model (CDOG) (Zheng et al., 2003; Yapa et al., 2002), and Johansen's model DEEPBLOW (Johansen, 2000). In deepwater scenarios, specific gas transformations occur:

- Hydrates formation and decomposition
- Gas dissolution
- Vertical leakage of gas from bent plumes
- Non-ideal gas law

At great depths gas and water mixtures can transform into hydrates, solid-like structures of gas and ice. While hydrates have reduced buoyancy compared to pure gas, they still ascend in the water column. Upon reaching lower pressures and higher temperatures, they may dissolve back as free gas (see Figure 2.6).

Both models acknowledge the importance of gas dissolution. Unlike oil dissolution, which has a negligible impact, gas dissolution significantly reduces overall plume buoyancy. It intensifies with increasing pressure, making it a critical factor as it contributes to the formation of intrusion layers beneath the surface.

Another characteristic to be considered when simulating deepwater spills is the influence of cross-currents, which bend the plume while gas bubbles leak out. This process is marked by a critical separation height h_S (see Figure 2.7, (Socolofsky and Adams, 2002)). Moreover, the slip velocity w_b of the bubble component with respect to the oil droplets should not be constant as in (Yapa and Li, 1997) but dependent on the dissolution and hydrates dynamics and on bubbles size. Finally, while at shallow depths the ideal gas equation is valid, at greater depths we have

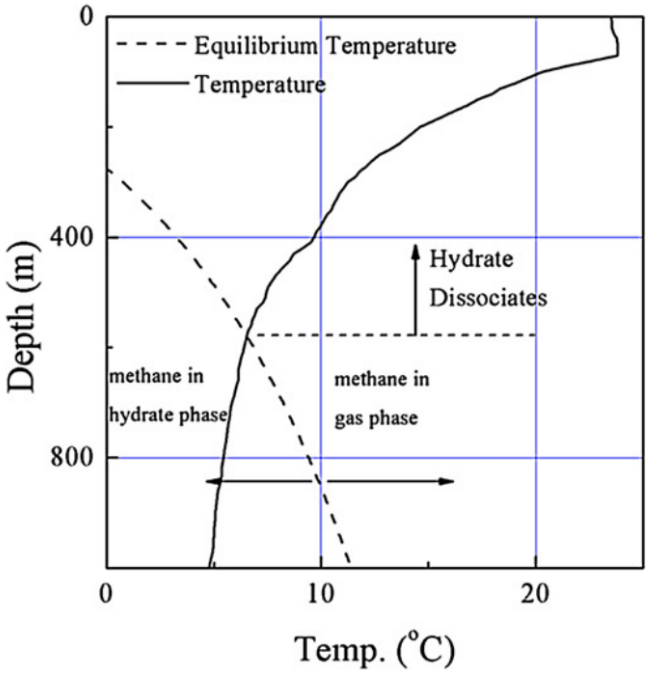

Figure 2.6: Thermodynamic equilibrium curve for a gas, methane, and a temperature profile for a location in Gulf of Mexico. The hydrate phase is below $z \sim 500$ m, while at shallower depths the hydrate component transforms in free gas. Courtesy of (Zheng et al., 2003).

a non-ideal gas behaviour. The depth-varying density of the gas, for this reason, is another competing factor in the overall plume buoyancy. The DEEPBLOW and CDOG models have been tested in the series of experiments known as Deepspill (Johansen et al., 2003).

The near-field model DEEPBLOW is integrated with Oil Spill Contingency and Response (OSCAR) (Reed et al., 1995), a 3D numerical model that merges physical and chemical behaviours in the far-field region with oil spill risk assessment for operational response. Similarly, the near-field model CDOG is coupled with the far-field model ADS (Advection-Diffusion Stage), with lagrangian simulations of gas bubbles and oil droplets. The coupling between the near and far field is not trivial and various solutions were proposed (Dasanayaka and Yapa, 2009). Another near-field multi-phase model is OILMAPDEEP, which is coupled with the far-field

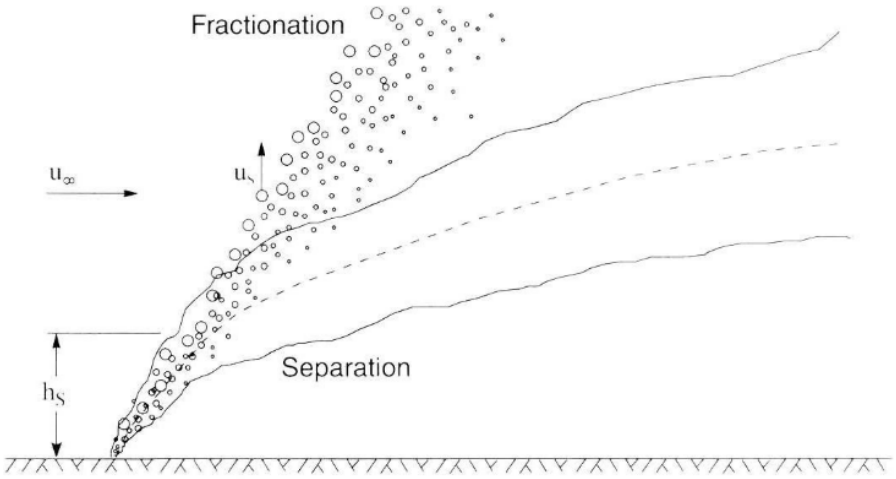

Figure 2.7: In deep waters, gas separation from the plume occurs as it is bent by strong cross-currents. Depending on their density and size, bubbles rise separately from the plume. Courtesy of (Socolofsky and Adams, 2002).

transport and fate model SIMAP/OILMAP (Spaulding et al., 2017). A review on gas and oil models in deepwater can be found in (Yapa et al., 2012).

Subsequent improvements have been made to these models. Following Johansen's work, Socolofsky introduced a multi-phase double plume model in (Socolofsky et al., 2008). After this work, the comprehensive Python-based Texas A and M Oilspill Calculator (TAMOC) was designed (Dissanayake et al., 2015). TAMOC's capabilities include multiphase plume modelling and double plume modelling. It also simulates changes in the chemical composition of released materials due to processes such as dissolution, evaporation, and chemical reactions.

2.5 Summary and conclusions

In the near-field phase, spilled oil droplets and gas bubbles ascend collectively in a coherent plume structure, mixing with the surrounding environment. Single-phase oil models encompass dimensional analysis predictions and Eulerian and Lagrangian integral models, accurately reproducing the dynamics. Due to their rapid implementation and higher accuracy, Lagrangian models have gained widespread adoption: the JETLAG model, initially designed for wastewater discharges (Lee and Cheung, 1990), has been later adapted for oil spills (Yapa and Li, 1997; Zheng and Yapa, 1998). Subsequently, other models were developed for oil and gas (multi-phase) discharges, successfully replicating both shallow and deepwater spills (Zheng et al., 2003; Johansen, 2000). A summary of the reviewed literature is presented in Table 2.3.

Recently, large eddy simulations (LES) have been applied to plume modelling (Yang et al., 2016b). LES models directly resolve large- and intermediate-scale turbulent motions, incorporating closure models to account for sub-grid-scale features. In an Eulerian framework, these models solve the incompressible Navier-Stokes equations for the water velocity field, and a advection-diffusion equation for the oil field.

Subsurface model	Method	Type of Discharge	Boundary environment	Processes included	Output
CORMIX	Dimensional Analysis of relevant variables	Conservative, degradable, heated, brine discharges or with suspended sediments. Single and multi-port.	Unbounded and bounded environment	Turbulent entrainment	Classification into 13 potential outcomes: steady-state values of geometry and dilution
CORJET	Eulerian Gaussian integral model	Positively-negatively buoyant discharges. Single and multi-port.	Unbounded with uniform or stable density stratification, stagnant or steady 2D currents	Azimuthal and stream-wise Entrainment and Terminal level	Trajectory, velocity, density, temperature, salinity, dilution
JETLAG	Lagrangian top-hat integral model	Wastewater discharges	Ocean salinity, temperature, 1D currents, stratification	Shear and Forces Entrainment	Element position, velocity, density, temperature, salinity, oil concentration, thickness, width
CDOG, DEEPBLOW	Lagrangian top-hat integral multi-phase model	Oil and gas discharges	Ocean salinity, temperature, 2D currents, stratification	Entrainment and Terminal level + Deep Gas phenomena (Cross-flow separation, Dissolution, Non-ideal behaviour and Hydrates dynamics)	Oil Plume trajectory, density, temperature, salinity, dilution, geometry + Gas bubbles fate and trajectories

Table 2.3: Primary subsurface blowout models include CORMIX (dimensional analysis), CORJET (Eulerian), JETLAG (Lagrangian), and CDOG, DEEPBLOW (multi-phase for deep-water).

Chapter 3

Modelling underwater near-field oil plume

3.1 Introduction

Subsurface oil spills pose significant challenges as they occur beneath the sea surface, making detection and mitigation more complex than surface spills. They can result from various sources, such as offshore drilling accidents, pipeline leaks, or underwater equipment failures. Subsurface spills can have long-lasting ecological impacts, as the oil can disperse widely before surfacing, affecting marine life at various depths.

Among blowouts and subsurface spills, the most notable is the BP Deepwater Horizon. The spill commenced on April 20, 2010, releasing a total of 680,000 tons of oil (Camilli et al., 2012; Lehr et al., 2011), with a continuous sustained discharge at a mean volume flux of 8000 tons per day (McNutt et al., 2011). After the initial gas separated from the plume, 17.4% of the total oil volume remained confined subsurface. A first intrusion level —indicating a balance between the oil's density and the surrounding water— was found approximately 200 meters above

the seabed of ∼1500 m. Then the oil was detrained from the primary plume and dispersed into multiple horizontal layers (North et al., 2011, 2015; French-McCay et al., 2021), covering distances of up to 100 km (Kessler et al., 2011).

However, despite occasional major accidents, blowouts happen infrequently, making it difficult to identify a clear pattern. In contrast, incidents stemming from pipeline damage have exhibited a consistent upward trend over the last decades (GESAMP, 2007). The combination of a growing number of offshore pipelines and the challenges posed by ageing and inadequate maintenance has contributed to this trend. Regions significantly impacted include the North Sea, the Gulf of Mexico (Jernelöv, 2010), and the Niger Delta (Nwilo and Badejo, 2005).

Addressing subsurface oil spills requires a comprehensive approach involving advanced monitoring technologies, effective spill response strategies, and ongoing research to understand the long-term environmental impacts. Additionally, subsurface oil spill models can aid in mitigating adverse effects by predicting the plume evolution from the release point and its dispersion at different depths.

The first interest in plume modelling dates back to the 1920s, when initial studies on convective plumes from heated bodies were developed by L. Prandtl and disciples. However, a milestone in this field is represented by the work of Morton (Morton et al., 1956), who first proposed the entrainment parameterisation of the turbulent convective processes at the plume edge.

Oil droplets and gas bubbles ascend together in a cohesive and self-similar structure from the depth of the release (Milgram, 1983). Typically, the term "jet" denotes the momentum-driven phase in proximity to the source. In instances where the discharge is lighter than the surrounding environment, as observed in oil spills, buoyancy acts as an additional source of momentum. This phase, commonly known as the "plume" (Lee et al., 2003; Lee and Cheung, 1991), dominates the motion furthest from the source.

The exit velocity v_0, nozzle diameter D_0, and the fluid kinematic viscosity ν de-

termine the turbulent versus laminar flow behaviour through the exit Reynolds number $Re = v_0 D_0/\nu$ (Fan, 1967). In fully turbulent flow ($Re > 10^3$), eddies form at the boundaries of the plume, leading to the entrainment of ambient water. The overall plume density increase causes the deceleration of the ascending buoyant motion. Depending on the release and boundary conditions, including ambient water current velocities and stratification, some plumes can reach the sea surface, while others become trapped at various depths (Socolofsky et al., 2008).

Within the framework of integral plume models, various perspectives have been considered (Socolofsky et al., 2016). Integral Eulerian models assess buoyancy, momentum, and volume fluxes along the plume's trajectory. Notably, McDougall (Mcdougall, 1978), Fannelop and Sjoen (Fannelop and Sjoen, 1980), and Milgram (Milgram, 1983) all proposed Eulerian models for vertical oil buoyant jets. They initially neglected the possible effect of ambient currents, which was subsequently incorporated (Schatzmann, 1979). Jirka (Jirka, 2004) proposed CORJET, a comprehensive and rigorous Eulerian plume model. This work outlined the principles and limitations of integral modelling and included verification using laboratory data. On the other hand, Lagrangian integral models treat the oil plume as a series of non-interfering moving elements (Winiarski and Frick, 1976). Frick (Frick, 1984) first introduced a 2D Lagrangian jet model for subsurface wastewater discharges called JETLAG. Later, Lee and Cheung (Lee and Cheung, 1990) introduced a more general model for buoyant jets with 3D trajectories.

Some years later, Yapa and Li developed ADMS/CDOG (Yapa and Li, 1997), a 3D multi-phase model for buoyant jets. This model can simulate leaks of oil, gas, or oil and gas mixtures and considers both the effect of ambient currents and stratification in plume dynamics. ADMS/CDOG has been extensively validated (Zheng and Yapa, 1998), including tests through the DeepSpill Experiment (Johansen et al., 2003). It has been extended from relatively shallow to deep water oil releases. Actually, in deep waters, other physical gas-related processes, such as hydrate formation, must

be considered (Yapa et al., 2002).

Another significant Lagrangian model for deepwater releases, called DEEPBLOW, was developed by Johansen (Johansen, 2000). This model also includes the capability to simulate hydrate formation and degradation, as well as gas bubble dissolution. Eulerian and Lagrangian formulations are considered equivalent (Frick et al., 1994). However, Lagrangian models incorporate the plume curvature effect along the trajectory, not present in Eulerian models.

Over time, plume models have undergone incremental adjustments, particularly in the incorporation of multi-phase and double-plume approaches, addressing deepwater specific dynamics such as hydrate formation and degradation. Examples are the TAMOC model (Dissanayake et al., 2015) and the OSCAR model (Reed et al., 1995; Barreto et al., 2021).

Our work designs the near-field component of an UnderWater Oil Release Model (UWORM-1), drawing inspiration from models outlined in Yapa and Li (1997) and Lee and Cheung (1990). UWORM-1 represents a pioneering effort, as it is the first openly accessible model of its kind featuring a systematic and consistent selection of variables and parameters. A significant aspect of our study focuses on the analytical examination of terminal levels, which includes defining a neutral level followed by determining a maximum rise level. The robustness of UWORM-1 is demonstrated through comprehensive testing, encompassing both laboratory experiments and large-scale field trials in the North Sea. Special attention is devoted to understanding the roles of different entrainment components in plume evolution, facilitating the calibration of the entrainment process. Moreover, UWORM-1 integrates ocean state data from the Copernicus Marine Service (CMEMS) as input.

In highly-stratified oceans, the near-field component can be coupled with far-field models, which simulate the transport of single oil droplets after the terminal level is reached. Alternatively, in low-stratified oceans, the plume reaches directly the surface, where a surface model such as Medslik-II can be coupled (De Dominicis

et al., 2013a,b).

This chapter is organised as follows: In Section 3.2, we present the model definitions and governing equations. In Section 3.3, we develop a numerical workflow to solve the model equations and update the system and ambient parameters. Section 3.4 characterises different flow regimes of the plume evolution through dimensional analysis. Following the state of the art, this method is useful to have an a-priori description of the subsurface spill. Sections 3.5 and 3.6 are dedicated to experimental validation using laboratory and in-situ data. For the large-scale NOFO experiment, we show a sensitivity analysis which enhances fit with observations. Section 3.7 contains a final discussion and future perspectives.

3.2 Model equations and variables

In this section, we describe the plume variables and their evolution through the near-field component of the UnderWater Oil Release Model (UWORM-1). UWORM-1 is

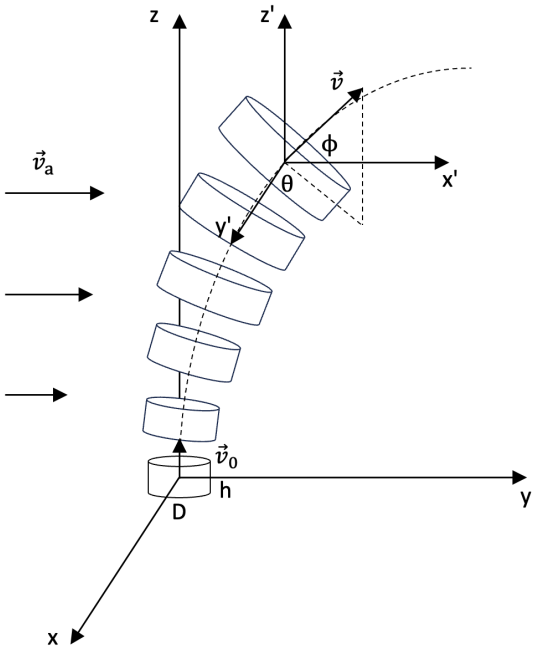

Figure 3.1: The plume is modelled as a series of independent cylinders, with diameter $D = 2b$ and thickness h. In a global cartesian coordinate system, $\vec{v}_0$ is the release velocity, and $\vec{v}_a$ is the ambient ocean velocity. In a local spherical coordinate system, each cylinder velocity is $(|\vec{v}|, v_\theta, v_\phi)$.

a Lagrangian integral plume model where non-interfering elements are modelled assuming self-similarity of the flow. Key properties of the discharged fluid, such as its velocity and oil concentration, maintain a similar cross-sections along the trajectory. Specifically, we assume that these properties are uniform in cross-sections (top-hat profiles). This hypothesis implies plume elements with cylindrical symmetry.

The model elements are shown in Figure 3.1, where a series of cylinders is released from the discharge location. Each cylinder is a mixture of oil and water, meaning it

	Name	Units
m	Oil and water mixture mass	kg
$c = m_{oil}/m$	Oil Mass Fraction	-
$\vec{v} = (u, v, w)$	Velocity	$\mathrm{m} \cdot \mathrm{s}^{-1}$
ρ_{oil}	Oil component density	$\mathrm{kg} \cdot \mathrm{m}^{-3}$
ρ_w	Water component density	$\mathrm{kg} \cdot \mathrm{m}^{-3}$
ρ	Oil and water mixture Density	$\mathrm{kg} \cdot \mathrm{m}^{-3}$
T	Temperature of the oil and water mixture	°C
S	Salinity of the of the oil and water mixture	PSU
$\vec{x} = (x, y, z)$	Position	m
h	Thickness of the cylinder	m
b	Radius of the cylinder	m

Table 3.1: The fifteen prognostic and diagnostic plume element variables: mass, oil mass fraction, 3D velocity, density, oil density, entrained water density, oil and water mixture density, temperature, salinity, 3D position, thickness, and radius.

	Name	Units
ρ_a	Ambient Density	$\mathrm{kg} \cdot \mathrm{m}^{-3}$
$\vec{v}_a = (u_a, v_a)$	Ambient Currents Velocity	$\mathrm{m} \cdot \mathrm{s}^{-1}$
c_a	Ambient Oil Mass Fraction	/
T_a	Ambient Temperature	°C
S_a	Ambient Salinity	PSU
N^2	Brunt-Väisälä frequency	s^{-2}

Table 3.2: Ambient ocean variables, considered as input to the plume model: ocean water density, 2D ocean currents velocity, oil mass fraction, ocean temperature, salinity and stratification identified by the Brunt-Väisälä frequency square.

has oil and water fractions. The cylinder mass is $m = \sum_i m_i$, where the subscript $i = \{oil, w\}$ refers to the oil and water masses inside the cylinder. The volume is $V = \sum_i m_i/\rho_i$ and the oil and water mixture density is therefore $\rho = m/V$. The oil mass fraction is $c = m_{oil}/m$, the radius of the cylinder is $b = D/2$, the thickness is h. The oil and water mixture in the cylinder has a specific temperature T and salinity S. All the plume and ambient water variables are reported respectively in Table 3.1 and Table 3.2. For each plume element, the conservation equations of mass, oil mass, momentum, heat and salinity, together with the cylinder position, the equation of states and the cylinder geometric dimensions, are:

$$\frac{dm}{dt} = \rho_a Q_e \tag{3.1a}$$
$$\frac{d(mc)}{dt} = c_a \frac{dm}{dt} \tag{3.1b}$$
$$\frac{d(m\vec{v})}{dt} = \vec{v}_a \frac{dm}{dt} + mg'\hat{k} \tag{3.1c}$$
$$\frac{d(mc_P T)}{dt} = c_P T_a \frac{dm}{dt} \tag{3.1d}$$
$$\frac{d(mS)}{dt} = S_a \frac{dm}{dt} \tag{3.1e}$$
$$\frac{d\vec{x}}{dt} = \vec{v} \tag{3.1f}$$
$$\rho_{oil}(T) = \rho_{ref}[1 - \beta_T(T - T_{ref})] \tag{3.1g}$$
$$\rho_w = EOS - 80(T, S) \tag{3.1h}$$
$$\rho = \frac{\rho_{oil} \cdot \rho_w}{\rho_{oil}(1-c) + \rho_w c} \tag{3.1i}$$
$$h = |\vec{v}|dt \tag{3.1j}$$
$$b = \sqrt{m(\rho\pi h)^{-1}} \tag{3.1k}$$

The system consists of 10 prognostic equations (3.1a)-(3.1f) and 5 diagnostic equations(3.1g)-(3.1k). The ambient variables are input to these equations, supposing the mixture of oil and water does not change the ocean water dynamics.

We describe now each equation from (3.1a) to (3.1k). Equation (3.1a) is the mass conservation equation, where the positive entrainment of seawater is considered by Q_e, the entraining volume flux. We are going to discuss this term in detail in Section 3.2.1. Turbulent mixing processes occurring at the plume edge are responsible for water entrainment and plume elements enlargement. Detailed parametrisations of the entrainment process are discussed in Section 3.2.1.

We chose not to include loss processes such as oil dissolution (Mackay and Leinonen, 1977b; Mishra and Kumar, 2015) and biodegradation (North et al., 2015), as these are typically negligible at this stage of evolution. They become significant in the far-field dynamics, where individual oil droplets are advected and diffused (Socolofsky

et al., 2008). However, for oil and gas discharges, it is necessary to consider loss processes also in the near field stages (while in the far-field gas bubbles are subject to very strong dissolution). Furthermore, in strong currents, the plume may lose a fraction of its mass as gas bubbles can detach due to their higher buoyancy (Spaulding et al., 2017), as we showed in Fig. 2.7.

Equation (3.1b) represents oil mass conservation, where the oil mass fraction dispersed in the surrounding ambient ocean is denoted as c_a. The entraining water mass, as described in Eq. (3.1a), progressively dilutes the oil concentration in the plume, leading to a change in its composition over time. Initially, with a composition of $c = 1$, the plume consists solely of oil, but this mass fraction undergoes a rapid decrease, resulting in a final composition predominantly of water.

Equation (3.1c) represents the momentum conservation of the plume element. It can be viewed as the momentum conservation of a body with time-varying mass, akin to the well-known physical case of a rocket, with the distinction that the cylinder mass is continuously increasing. In a manner similar to the rocket case, we can readily explain the first term on the right-hand side of Eq.(3.1c) by considering that the mass excess exerts a force on the body that is proportional to the velocity difference between the ambient fluid and the body itself. The second term on the right-hand side of Eq.(3.1c) corresponds to the buoyancy force, which is associated with the reduced gravity

$$g' = \frac{(\rho_a - \rho)}{\rho_{a0}} g \tag{3.2}$$

where g is gravitational acceleration and ρ_{a0} is a reference seawater density, often taken at the depth of the release.

Equation (3.1d) depicts the conservation of the cylinder heat content. In the absence of pressure work on the cylinders, the total cylinder internal energy is equal to the cylinder heat content, defined as $Q = mc_P T$, where c_P is the specific heat at

constant pressure. This internal heat content can only be changed in our model by the entraining water heat content, defined as $c_{Pa}T_a\frac{dm}{dt}$, with T_a being the ambient water temperature. For simplicity, we approximate the equality of specific heat coefficients $c_{P\,a} = c_P$.

The salt mass conservation equation (3.1e) is defined in a similar fashion to the oil conservation (3.1b), as both describe a mass conservation. The ambient ocean salinity profile S_a is given as input.

The 3D equations (3.1f) determine the position of the cylinders during their evolution.

The system is completed by the oil component equation of state (3.1g), the entrained ambient water equation of state (3.1h) and the oil and water mixture density (3.1i). The latter is the density $\rho = m/V$ of two non-miscible fluids in the volume V and the total mass m of the cylinders. It can be readily observed that the density in eq (3.1i) is a function of the oil mass fraction c, the oil density ρ_{oil}, and the entrained water density ρ_w. The oil density equation (3.1g) uses reference value $\rho_{ref} = \rho_{oil}(T_{ref})$, where $T_{ref} = 15.5°C$ (Lehr et al., 2002), and the thermal expansion coefficient $\beta_T = 7 \cdot 10^{-4\circ}C^{-1}$. The seawater density is the ambient water density that has been entrained in the cylinder and thus it is computed using the salinity and temperature of the cylinder. For this seawater we use the Equation of State of Seawater (EOS-80), (Fofonoff and Millard, 1983) which is normally used also for the ambient seawater.

To gain insights into the problem, it is valuable to examine a reduced physical case for which it is possible to find an analytical solution. In equations (3.1b), (3.1c), (3.1d), (3.1e), when we neglect the buoyancy term, the simplified equation for the generic X variable is

$$\frac{d(mX)}{dt} = X_a\frac{dm}{dt}$$

Considering the initial mass m_0 is trivial to find the analytical solution:

$$X(m(t)) = X_a\left[1 - \frac{m_0}{m(t)}\right] + X_0\frac{m_0}{m(t)}$$

At time $t = 0, X = X_0$. As $t \to \infty$, $m(t) \to \infty$ (because of continuous seawater entrainment), and the plume variable tends to the ambient one $X(t) \to X_a$. That means, if there aren't other processes, the plume variable X eventually approaches the ambient variable X_a. Thus the plume variables (velocity, oil concentration, temperature, and salinity) tend to the respective ambient values.

3.2.1 Seawater entrainment

The turbulent entrainment of ambient seawater into the plume was first successfully described by Morton in 1956 with the "entrainment hypothesis" (Morton et al., 1956). In the seminal work, the dilution rate, proportional to the seawater entrainment, was assumed to be proportional to the plume diameter and the velocity shear between the plume flow the and ambient flow. The turbulent vortices at the plume's edge were identified as the source of mixing between oil and water, leading to the entrainment of water into the plume. The shear entrainment was later complemented by forced entrainment, which is the water inflow directly induced by ambient currents (Hoult et al., 1969). In (Lee et al., 2003), these two entraining fluxes are respectively the shear flux Q_s and the forced flux Q_f. The component Q_s is primarily due to the shear between the two interacting fluid velocities, while the forced flux Q_f is a result of the incident ambient current flow onto the plume's lateral surface. Although the two mechanisms assumptions are well-established, there is no uniform agreement on how they should be combined. We choose the parametrisation where the total entrained flux is the maximum between the two contributions (Lee and Cheung, 1990):

$$Q_e = \max(Q_s, Q_f) \tag{3.3}$$

An alternative smoother transition between the two contributions is proposed in (Lee et al., 2008). We choose to maintain the maximum hypothesis first to understand the relative role of the two components.

We now define the ambient velocity projection $\vec{v}_a$ onto the plume velocity $\vec{v}$ as $v_{a\parallel} = (\vec{v}_a \cdot \vec{v})/|\vec{v}|$. The shear flux is proportional to the cylinder lateral surface and the difference between the plume velocity and the ocean projected velocity, with modulation given by the "entrainment coefficient" α:

$$Q_s = 2\pi bh\alpha(F, \vec{v}, \vec{v}_a)(v - v_{a\parallel}) \tag{3.4}$$

The shear volume flux is at its maximum when the injected flow and the ambient flow are perpendicular to each other and at its minimum when the two flows are parallel. In the case of a pure vertical discharge, where the entraining fluid and the ambient fluid flows are perpendicular, the shear is maximised. This happens because ocean currents typically have a significant horizontal component with a negligible vertical one. In such situations, the shear flux becomes the dominant component in the initial stage of plume evolution. Conversely, the shear is minimised when the two fluids move in the same direction and have similar intensities, often occurring during the bent-over secondary stage of plume evolution.

The entrainment coefficient α was estimated by comparing computations and field measurements in different ways. We adopt the one by (Yapa and Li, 1997; Zheng and Yapa, 1998):

$$\alpha(F, \vec{v}, \vec{v}_a) = \frac{a_1 + a_2 \frac{\sin v_\phi}{F_d^2}}{1 + a_3 \frac{v_{a\parallel}}{|\vec{v}| - v_{a\parallel}}} \tag{3.5}$$

where

$$F_d = \frac{v - v_{a\parallel}}{\sqrt{2g'b}} \tag{3.6}$$

is the densimetric Froude number, the ratio between momentum and buoyancy forces. The empirical coefficients a_1, a_2, a_3 adapted from (Yapa and Li, 1997), are given in Table 3.3. The forced flux Q_f is the currents-driven flow on the windward

Parameter Symbol	Default Value
a_1	0.081
a_2	0.098
a_3	5

Table 3.3: Shear entrainment optimal empirical parameters obtained from Yapa and Li (1997).

side A_a of each plume element (Lee et al., 2003). Given an ambient velocity $\vec{v}_a$, the forced flux is defined as:

$$Q_f = \int_{A_w} \vec{v}_a \cdot d\vec{A} \tag{3.7}$$

where A_w is the windward portion of the cylinder lateral surface. This value relies on the magnitude of ocean current velocity and the cylinder's alignment relative to the flow, which dictates the exposed surface of the cylinder facing the current.

The computation of Q_f becomes intricate when accounting for the distortion of the plume induced by the force of the ocean current. In fact, each cylinder undergoes virtual stretching, bending, and expansion during its development. The comprehensive derivation of forced entrainment accounts for the geometry of the plume-ocean system and is documented in Appendix A.1 Forced entrainment computation.

3.3 Numerical methods

UWORM-1 is coded in Python. In this section, the model inputs, numerical scheme, and outputs are described. As inputs, UWORM-1 requires the current velocity, temperature, and salinity 3D fields. These are obtained from general circulation operational model fields such as the Copernicus Marine Service (Traon et al., 2019). Density profiles are obtained from salinity and temperature data through the EOS-80 formula and the Brunt-Väisälä frequency is computed by finite differences in the input model eulerian grid. The input data are bilinearly interpolated at the latitude and longitude location of the release. Ambient input data could be alternatively provided by experimental observations.

UWORM-1 can simulate both instantaneous and continuous oil releases, being the continuous case obtained with a sequential release of cylinders, each of them carrying a certain amount of oil. Continuous release simulations are mandatory in the presence of time-varying ocean conditions, which can have varying impacts on different segments of the release.

Figure 3.2 represents the workflow implemented in our numerical simulation. The specific oil release provide the initial conditions for the 10 prognostic governing equations (3.1a-3.1f) and 5 diagnostic equations (3.1g-3.1k). The initial condition in top-hat assumption is provided by the discharged velocity v_0, the nozzle radius b_0 and the volume flux $Q_0 = \pi b_0^2 v_0$. Knowing the initial oil mass fraction $c_0 = 1$, the initial mass $m_0 = \rho_{oil}(T_0)\pi b_0^2$ is computed. The position of the release z_0 is also required.

The prognostic ordinary equations are numerically solved by a Runge Kutta IV integration scheme, with boundary conditions depending on the cylinder depth. After time stepping, the plume temperature T and salinity S are used to diagnose the oil and water densities in the plume. Finally, the entrainment coefficient, the reduced gravity, the plume, and ambient variables are updated. The proposed

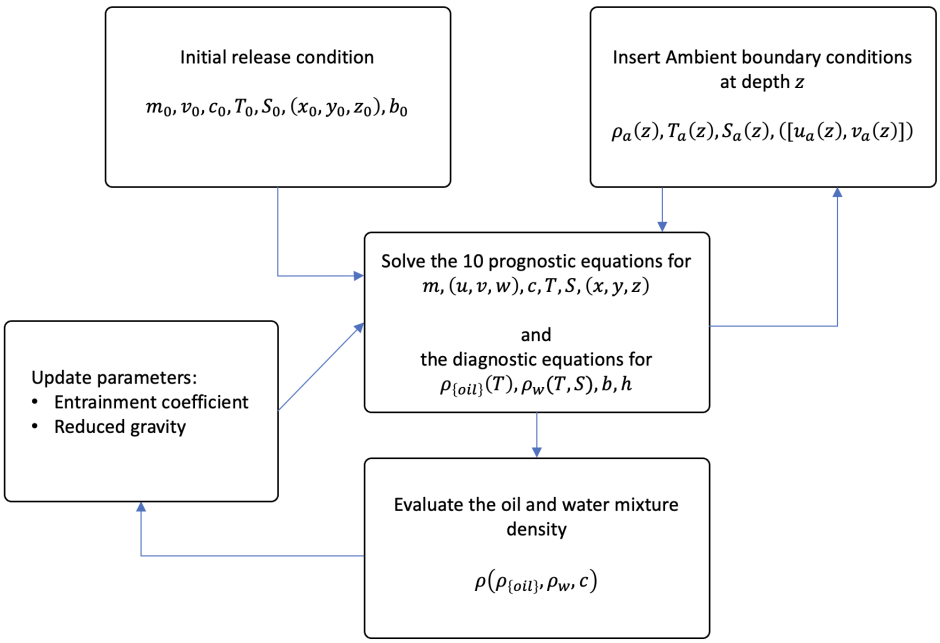

Figure 3.2: Numerical scheme workflow. The release variables serve as initial condition. At each time-step, the 10 prognostic equations and 5 diagnostic equations are solved. The ambient ocean profiles are interpolated at the cylinder depth and inserted in the equations. With the oil and entrained seawater density calculated from T and S, the density of the oil and water mixture is obtained. Finally, the reduced gravity and the entrainment coefficient are updated.

scheme is shown in Figure 3.2. The Euler discretisation of the set of 15 equations is reported in Appendix A.2 Plume model numerical discretization.

3.4 Jet / plume regimes

Different stages in the plume evolution are linked to different drivers of the motion. The initial and boundary conditions can provide general information about these different stages or regimes (Socolofsky and Adams, 2002; Socolofsky et al., 2016). Dimensional analysis enables us to identify characteristic length scales for different regimes. In this section, we discuss length scales that are commonly referenced in the field. Additionally, we include a concise derivation of these scales from (Lee et al., 2003).

An initial "jet phase" is driven by the momentum resulting from the discharge pressure. Subsequently the buoyancy force, due to the density difference between the jet and the water, comes into play, making buoyancy the primary driver of momentum. In this "plume-phase" the influence of the initial discharge diminishes. Other drivers are imposed by the environment: ocean currents are responsible for entraining water masses, but also impact on the horizontal plume momentum as shown in Eq.(3.1c). Ocean stratification determines the occurrence of a terminal level of transition between the near and far-field. In the following, we will explore how these forcings are connected to characteristic length scales of the plume's evolution.

Dimensional analysis allows us to express a general dependent variable, such as the maximum height of rise, the vertical velocity, or the oil concentration, as power laws of the initial release and boundary variables (Lee et al., 2003; Richards et al., 2014). In a cylindrical symmetry (top-hat profile) the initial volume flux Q_0, momentum flux M_0 and the buoyancy force flux B_0 are defined

$$Q_0 = v_0 \pi b_0^2$$

$$M_0 = Q_0 v_0$$

$$B_0 = Q_0 g_0' = Q_0 \frac{(\rho_{a0} - \rho_0)}{\rho_{a0}} g$$

where ρ_{a0} is the ocean density at the release depth and g' is the reduced gravity. Dimensions are $[Q_0] = L^3T^{-1}$, $[M_0] = L^4T^{-2}$, $[B_0] = L^4T^{-3}$, in units of length L and time T. The ocean current intensity has units $[v_a] = LT^{-1}$.

In the water column, the Brunt-Väisälä frequency $N^2 = -\frac{g}{\rho_0}\frac{\partial \rho_a}{\partial z}$ (with units $[N^2] = T^{-2}$) is a measure of stratification. With this definition $N^2 > 0$ corresponds to stable and $N^2 < 0$ to unstable water column.

During the jet-phase, we assume that the cylinder vertical velocity w_J is dependent only on M_0 and on the distance from the source z (as entrainment is dependent on z). Applying dimensional analysis it is readily found that $w_J \propto M_0^{1/2} z^{-1}$.

In a similar manner it is found that in the plume phase, w_P is dependent on B_0 and z according to the law $w_P \propto B_0^{1/3} z^{-1/3}$.

A possible way to define the transition between jet and plume is by finding the depth where the respective velocities become comparable. When $w_J \sim w_P$, the jet phase comes to an end, and the plume phase begins. This condition defines that the jet-plume transition occurs at the distance L_{JP} from the source:

$$L_{JP} \propto B_0^{-1/2} M_0^{3/4} \tag{3.8}$$

This scale can be also expressed in terms of the initial Froude number $F_{d0} = \frac{v_0}{\sqrt{g_0' D}}$ as $L_{JP} = (\frac{\pi}{4})^{1/4} D F_{d0}$. When L_{JP} is small (and so is the Froude number), the plume-phase dominates, whereas the jet-phase is very short. Conversely, when L_{JP} is large, the jet-phase dominates, the initial discharge drives the overall trajectory and buoyancy is limited.

Another characteristic plume regime is caused by ocean currents intensity $|v_a|$. As the plume evolves, the motion is influenced by the currents, which cause bending. When the vertical buoyancy and momentum -induced motion and the horizontal advection become comparable ($w_P \sim |v_a|$), the plume-ambient currents transition occurs, at a distance L_{PA} from the source:

$$L_{PA} \propto B_0 |v_a|^{-3} \tag{3.9}$$

If the jet phase is dominant with respect to the plume phase, currents act on the jet-phase. In this particular case ee define the transition distance L_{JA} from jet to ambient currents $w_J \sim |v_a|$:

$$L_{JA} \propto M_0^{1/2} |v_a|^{-1} \tag{3.10}$$

The proportionality coefficients in Eqs. (3.8),(3.9), (3.10) have been determined experimentally in numerous works (Richards et al., 2014; Bloomfield and Kerr, 2000).

In a stratified ocean, the mixture of oil and entrained seawater can reach a density equal to the ambient ocean density (not in a non-stratified where the plume remains lighter than surroundings at all depths). The dynamics is explained through the vertical component of Eq. (3.1c):

$$m\frac{dw}{dt} = -w\frac{dm}{dt} + m\frac{\rho_a - \rho}{\rho_{a0}}g \tag{3.11}$$

The first term on the right side is the inertia: with increasing mass, the velocity is progressively reduced. The second term is the upward buoyancy force, which reduces as the water entrains the plume and the overall density equals with the ambient density. When the plume, carrying denser water from the lower levels, has same density of the surroundings, a “neutral buoyancy” is reached, at distance L_{nb} from the source. As buoyancy switches to negative, it causes the cylinder to decelerate, defining a maximum height of rise L_{max} for $w \to 0$. Various definitions exist regarding the end of the near-field phase and no universally adopted criterion of the terminal level exists (Dasanayaka and Yapa, 2009). While an oscillatory behaviour is observed due to the alternation of positive and negative buoyancy, our simulations conclude upon reaching $|w| < 10^{-3}\text{ms}^{-1}$. The particular threshold is chosen for the stability of the simulation.

When the ocean stratification N acts on a plume-like phase (dominated by buoyancy B_0), the stratification scale can be expressed through dimensional analysis:

$$L_{nb} \sim L_{max} \propto B_0^{1/4} N^{-3/4} \tag{3.12}$$

The respective proportional coefficients have been found in experiments by (Richards et al., 2014):

$$\begin{cases} L_{nb} & \sim 2.7\, B_0^{1/4} N^{-3/4} \\ L_{max} & \sim 4.0\, B_0^{1/4} N^{-3/4} \end{cases} \tag{3.13}$$

3.5 Model validation in laboratory-scale experiments

In this section, we verify the model correctness and the capability to reproduce simple scenarios. To do so, UWORM-1 output is compared with laboratory-scale data in different conditions. We compare simulated trajectory and oil mass fraction with laboratory data from (Fan, 1967; Fan and Brooks, 1969) and (Wright, 1977b) considering unstratified/stratified ambient conditions in the presence of horizontal currents. In the stratified case, the terminal level is attained.

3.5.1 Unstratified flowing ambient

A lighter fluid is released into a flowing heavier ambient. The undergone regimes are the "jet", the "plume" and the currents-driven phase. So the relevant length scales are the jet-plume transition L_{JP}, and the jet-ambient current transition L_{JA}. Seven experiments are reported in Table 3.4. The ambient flow is along the x-axis $\vec{v}_a = (u_a, 0, 0)$. The ambient density is $\rho_a = 1022\,\mathrm{kg/m^3}$ for all the experiments. The released and ambient fluids share the same temperature, with density differences obtained with different salinities. The discharge radius is $b_0 = 0.0038$ m, and the release depth is $z_0 = -1$ m. Simulations are run for 0.13 min, with time-step $\Delta t = 0.005$ s.

The comparison between simulation and data is shown in Figure 3.3**a** (trajectories) and in Figure 3.3**b** (oil concentration). In general, simulations exhibit good agreement with data for all the experiments. As the currents decrease, trajectories have a greater vertical component and are less horizontally deviated. The diminishing

No.	v_0(m/s)	v_a(m/s)	$(\rho_a - \rho_{oil})/\rho_a$	L_{JP}(m)	L_{JA}(m)
1a	1.05	0.26	0.15	0.005	0.027
1b	1.05	0.13	0.15	0.005	0.054
1c	1.11	0.28	0.04	0.009	0.027
1d	1.11	0.14	0.04	0.009	0.054
1e	2.08	0.17	0.15	0.013	0.080
1f	1.63	0.41	0.02	0.022	0.027
1g	1.63	0.20	0.02	0.022	0.054

Table 3.4: Seven experiments in unstratified ($\rho_a = $ const) flowing ambient. Data from Fan (1967). The discharge parameters and ambient variables are indicated, together with the jet-plume scale and the jet-currents scale.

currents effect is evident in the experiments with the same L_{JP} : from 1a to 1b, from 1c to 1e, from 1f to 1g. At the same time, the jet-currents transition scale L_{JA} increases as currents effect is dominating later in the motion. The oil mass fraction is $c = 1$ at the discharge location (where the plume is composed by oil only) and decreases with time.

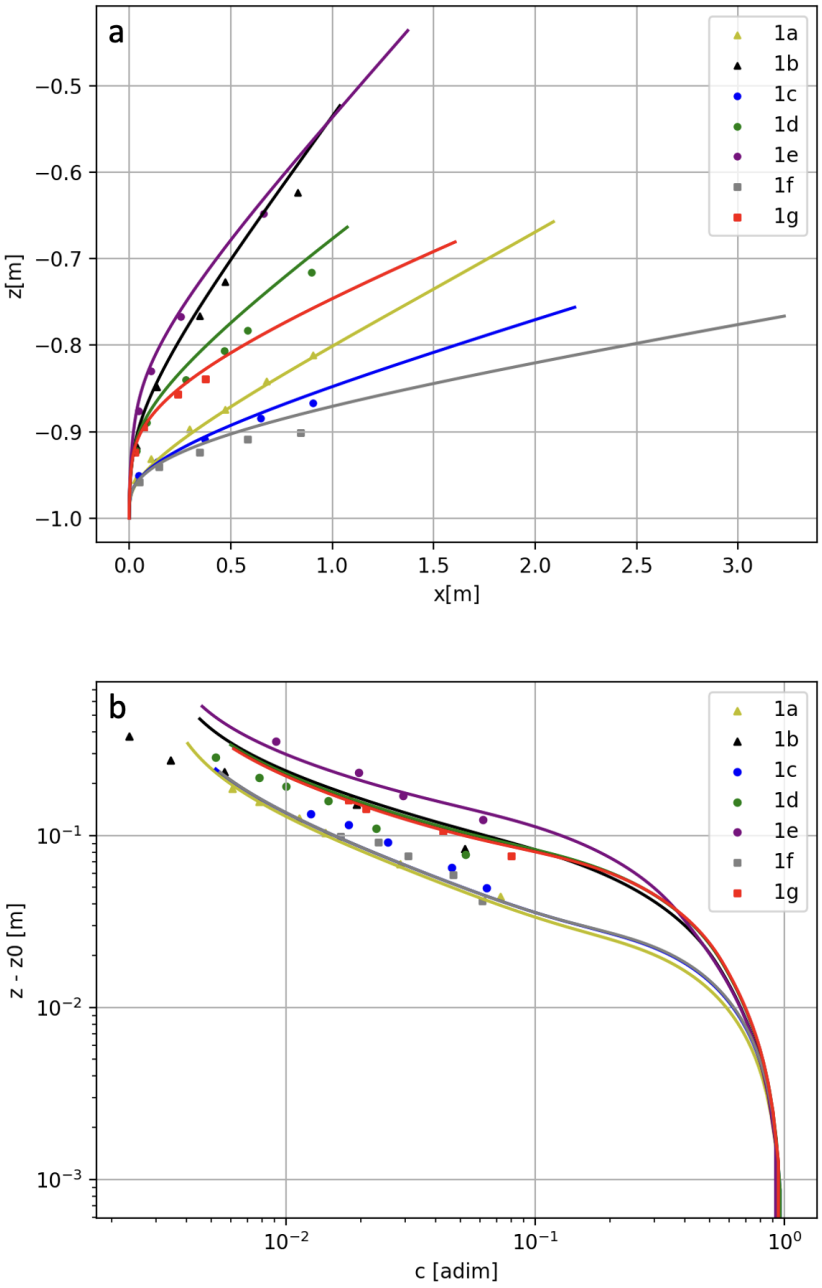

Figure 3.3: UWORM-1 simulation (solid lines) and laboratory data (markers) are compared in flowing unstratified ambient water. In **a** the x-z trajectories, in **b** the oil concentrations. The ambient parameters and release conditions in Table 3.4.

3.5.2 Stratified flowing ambient

No.	b_0 (m)	v_0(m/s)	v_a(m/s)	$\frac{\rho_{a0}-\rho_{oil}}{\rho_{a0}}$	$N^2(s^{-2})$	L_{max}(m)	$L_{max-exp}$(m)
2a	0.001	3.38	0.015	0.004	0.20	0.19	0.34
2b	0.001	4.08	0.014	0.004	0.20	0.20	0.38
2c	0.005	0.10	0.031	0.023	0.10	0.34	0.15
2d	0.005	0.08	0.016	0.027	0.11	0.32	0.23
2e	0.001	1.53	0.013	0.005	0.08	0.23	0.25
2f	0.001	2.07	0.013	0.005	0.08	0.24	0.30
2g	0.005	0.05	0.014	0.071	0.17	0.31	0.23
2h	0.002	0.57	0.020	0.023	0.09	0.36	0.23
2i	0.005	0.08	0.013	0.112	0.17	0.40	0.32
2l	0.005	0.08	0.013	0.112	0.17	0.40	0.32
2m	0.005	0.05	0.015	0.106	0.09	0.46	0.34
2n	0.005	0.07	0.016	0.106	0.09	0.49	0.36
2o	0.002	0.41	0.020	0.052	0.11	0.38	0.28
2p	0.002	0.47	0.025	0.052	0.11	0.39	0.27

Table 3.5: Fourteen experiments were performed in a stratified flowing ambient. Data from Wright (1977a,b). The initial discharge variables and ambient paramters are shown, alongside with L_{max} from dimensional analysis and the experimental value $L_{max-exp}$.

UWORM-1 is here applied to a stratified and flowing environment. The experiments conducted in a stratified water profile aim to assess the model's capability to predict the maximum height of rise. Data for validation are sourced from (Wright, 1977a,b). The initial release conditions as well as ambient conditions, including stratification N and currents $(v_a, 0, 0)$, are in Table 3.5. The experimental and theoretical (from dimensional analysis) L_{max} are also reported.

Fourteen cases are simulated to compare the modelled height of maximum rise with the experimental data. The comparison with simulation is shown in Figure 3.4**b**. While there is a general agreement, certain configurations (2a, 2b, 2e) exhibit better results than others. Even if an overall agreement is attained, this analysis

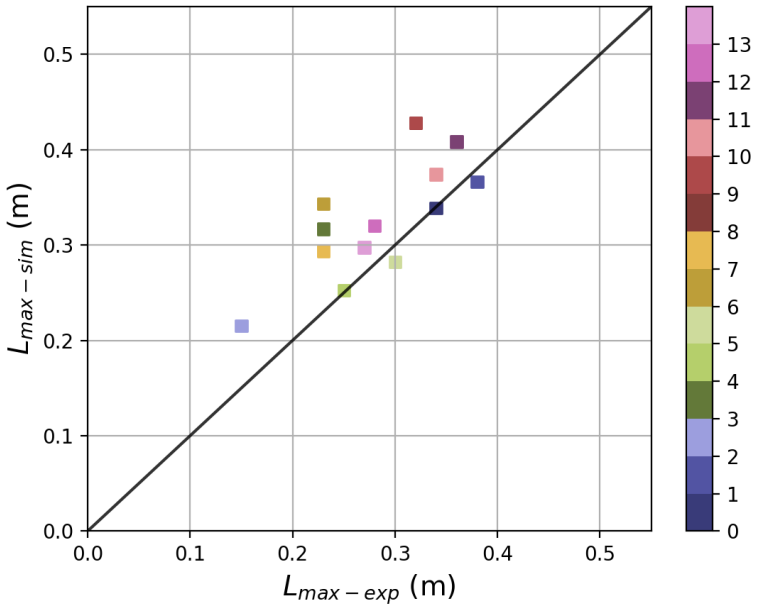

Figure 3.4: UWORM-1 simulation and laboratory data are compared in stratified ambient water. The simulated maximum height of rise is compared with the experimental value.

shows that in stratified conditions it is necessary to do calibration on the model parameters.

3.6 Model validation in large-scale North Sea exercise

In this section, we validate UWORM-1 comparing the numerical simulation with a large-scale experiment. We select an exercise conducted by IKU Petroleum Research and Norwegian Clean Seas (NOFO) in Norwegian seas during 1995-1996 (Rye and Brandvik, 1997; Rye et al., 1996, 1997), which constitutes an unique case for subsurface releases understanding and model validation.

In August 1995 was released oil, while in June 1996, a mixture of oil and gas, with

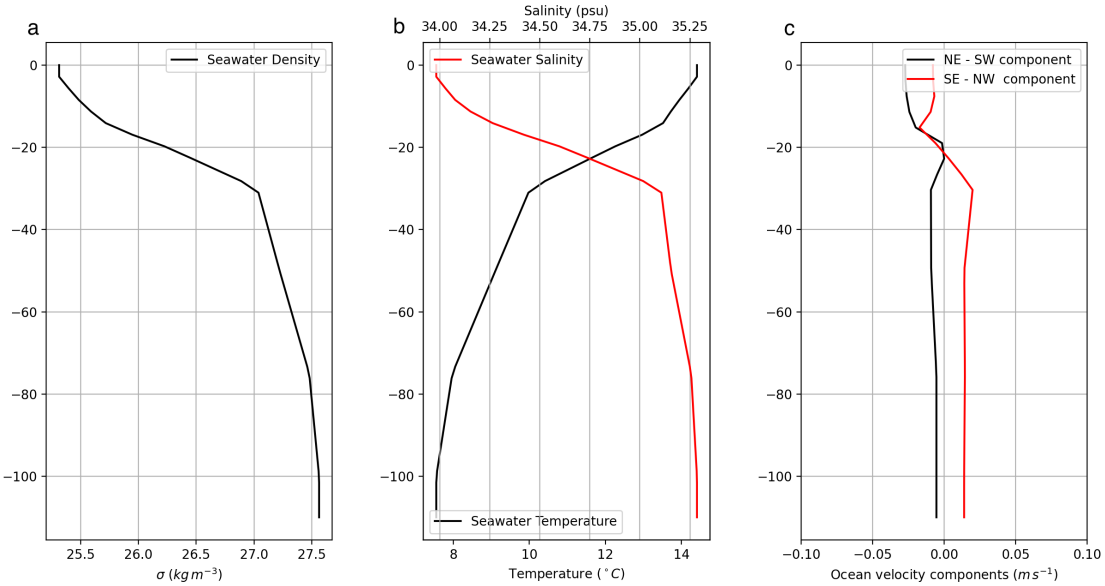

Figure 3.5: In **a**,**b** the ambient vertical profiles of seawater density, temperature, and salinity at the location and time of the oil release at the Frigg Field from the Copernicus Marine Service reanalysis fields. In **c**, the ocean velocity vertical profile, which vary over time. The depicted velocity components profiles are interpolated at 08:13 local time.

different gas-to-oil ratios (GOR) (Rye et al., 1997). UWORM-1 considers only oil releases and then our comparison will be done only with the 1995 experiment. A pipe was placed on the seabed, and a system of sonar and Remote Operating Vehicles (ROV) was employed to record the plume's position and width over time. The selected site was in the Frigg Field region at coordinates 60° 1' N, 2° 33' E. The oil was released from a depth of $z_0 = -107$ m, commencing at 08:13 local time, with measurements of width and position recorded at 10 m depth intervals. Due to the specific ocean conditions and stratification, the buoyant oil rose as a plume until it reached zero buoyancy and came to a stop at an intrusion level. After this near-field behaviour, the plume transitioned into a cloud of individual droplets, commonly referred to as far-field behaviour. The first surfacing of these droplets was recorded at 08:25:30 local time.

The release consisted of heavy Nigerian crude oil. According to the ADIOS oil database (Lehr et al., 2002), the oil's reference density at temperature $T_0 = 15.5°C$ is $\rho_{oil}(T_0 = 15.5°C) = 893$ kg m^{-3}. In our simulation, oil density decreases its temperature according to the thermal expansion Eq.3.1g, with $\beta_T = 7 \cdot 10^{-4 \circ} C^{-1}$. A total volume of 25 m^3 was released in about 25 min, therefore with an initial volume flux $Q_0 = 1$ m$^3 s^{-1}$. The nozzle radius was $b = 0.0508$ m, giving an initial exit velocity of $\vec{v}_0 = 2.1$ ms^{-1}. The initial temperature and salinity of the jet at the source are set to $T_0 = 10°$C and $S_0 = 0$ PSU. These values pertain to the oil only since no water is entrained yet.

The ocean state at the release location is obtained from the Copernicus Marine Service reanalysis fields. In particular, the North West Shelf product is used, with a horizontal resolution of 0.111×0.067, 24 σ-vertical levels, at a daily frequency. Density, salinity, and temperature fields are bi-linearly interpolated on the lat-lon of the release location (Fig.3.5a and Fig.3.5b) and are assumed constant throughout the entire experiment, which last less than 10 min. Ocean velocity components are shown in Fig. 3.5c.

Table 3.6 provides a summary on the experiment's initial and boundary conditions: the nozzle radius, the vertical exit velocity, the oil density, the relative buoyancy difference, the depth-averaged Brunt-Väisälä frequency N^2 (over the near-field region), and the densimetric Froude number F_d.

b_0(m)	v_0(m s^{-1})	ρ_{oil0}(kg m^{-3})	$(\rho_{a0} - \rho_{oil0})/\rho_{a0}$	$\bar{N^2}$(s^{-2})	F_{d0}
0.0508	2.10	896.4	0.128	$7 \cdot 10^{-5}$	18.1

Table 3.6: North Sea experiment initial release variables and ambient ocean conditions.

The small Brunt Vaisala frequency value suggests a minimal stratification effect. The importance of buoyancy is demonstrated by the high Froude number. The ambient currents are relatively weak in comparison to the vertical exit velocity.

The numerical simulation is run for $\sim$ 6 min, with a time step $\Delta t = 0.01$ s. Validation data (Rye et al., 1996, 1997) is the intrusion terminal level, the plume position in time, the width of the plume. No information on the evolution of oil concentration, plume temperature and salinity is provided.

Our comparative analysis focuses on examining the intrusion levels, plume shape, and plume velocity.

First, we investigate the intrusion levels: the height of maximum rise ($w = 0$) and the neutral buoyancy level ($\rho = \rho_a$) showed in Fig. 3.6. Table 3.7 gives a comparison between dimensional analysis, UWORM-1 simulation, and data. Optimal agreement with data is found for L_{max} while no in-situ data is available for L_{nb}. Dimensional analysis offers a good prediction of both L_{max} and L_{nb}. This suggests that stratification is dominant, while the jet-effect and the currents effect are negligible.

Next, we analyze the plume shape in Fig.3.7**a** and Fig.3.8. While there is reasonable agreement between UWORM-1 and the simulation by Yapa et al. (1999), there is evident underestimation of the plume diameter, approximately $\sim 50\%$, compared to data. Finally, we evaluate the plume velocity. In Fig.3.7**b**, we depict the plume's position over time. The rising velocity is overestimated: UWORM-1 plume is $\sim 48\%$ faster than data.

	data	dim analysis	UWORM-1 sim
L_{JP}(m)	-	-106.4	-
L_{PA}(m)	-	above surface	-
L_{nb}(m)	-	-69.71	-66.61
L_{max}(m)	-50 ± 5	-51.75	-54.16

Table 3.7: Transition scales and intrusion levels from the NOFO Experiment are compared with dimensional analysis and UWORM-1 output.

In summary, our model accurately determines the intrusion level, but there is an

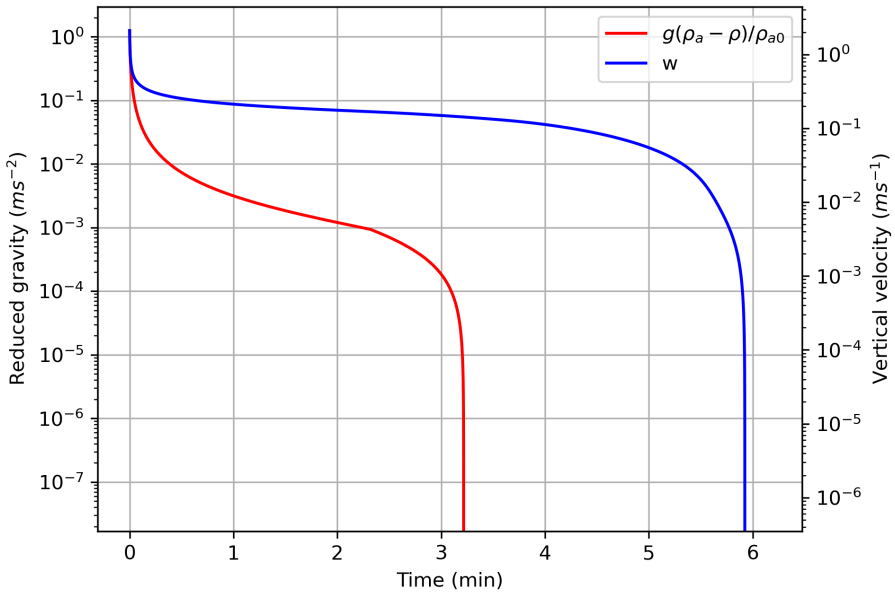

Figure 3.6: North Sea Experiment: the neutral buoyancy level is linked to reduced gravity $\to 0$ (red) and the maximum height with $w \to 0$ (blue).

underestimation of the plume volume and an overestimation of the vertical velocity. The most significant contributors to the entrainment error are the parametrisation of shear coefficients (specifically, the experimental coefficients a_1, a_2, a_3) and the accuracy of ocean currents. Ocean currents impact both the shear and forced components of entrainment and also influence the horizontal momentum equation, leading to variations in plume bending. The presence of a terminal level depends on the accuracy of temperature and salinity fields, which combine to determine ambient water density. These aspects will be discussed in the next section, where a sensitivity analysis on entrainment will be presented.

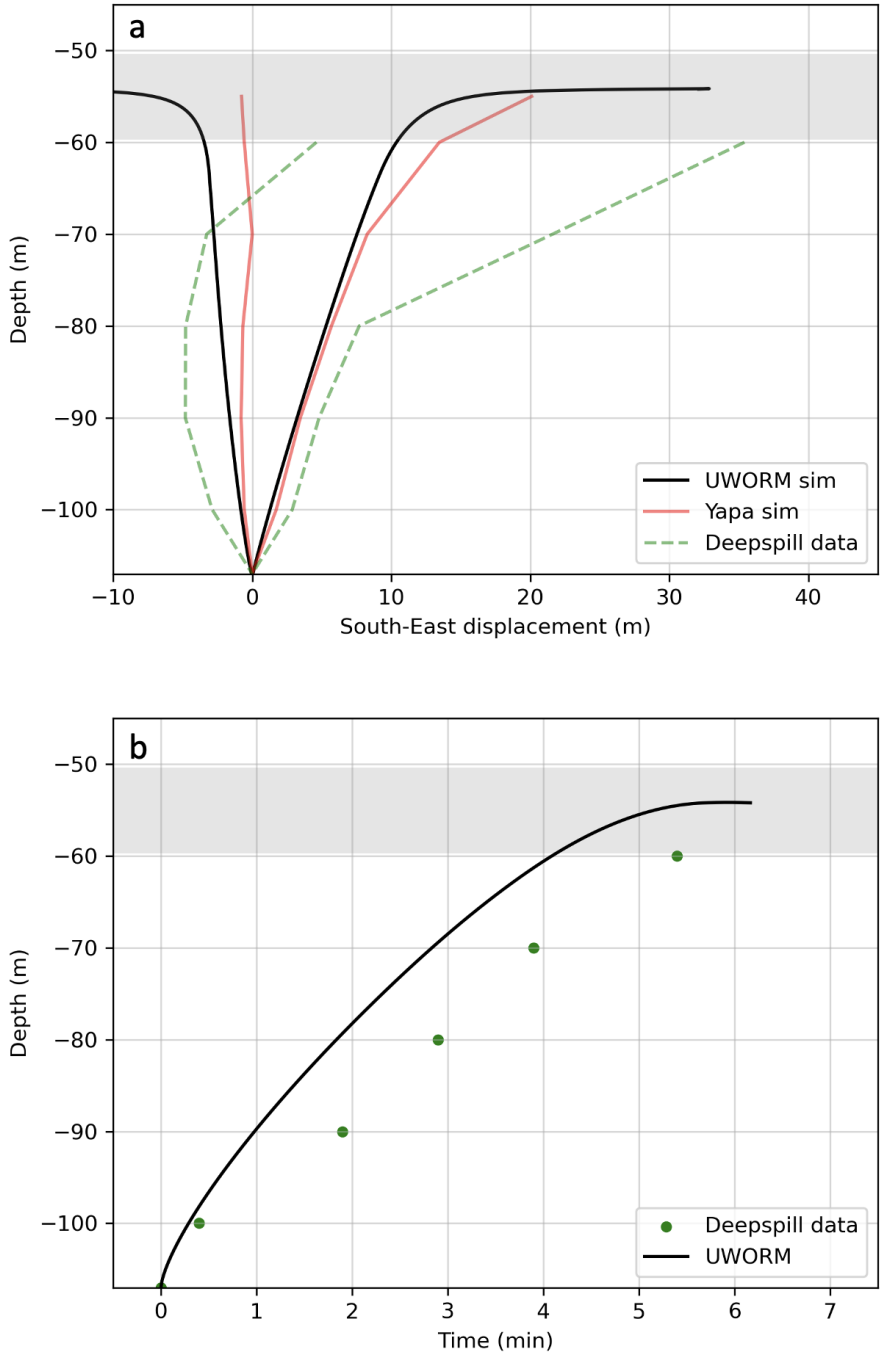

Figure 3.7: North Sea Experiment: in **a** the plume envelope, in **b** the plume centerline position in time. A comparison between simulations (UWORM-1 in black and (Yapa et al., 1999) in red) and data (green) is shown. Observed terminal range (grey).

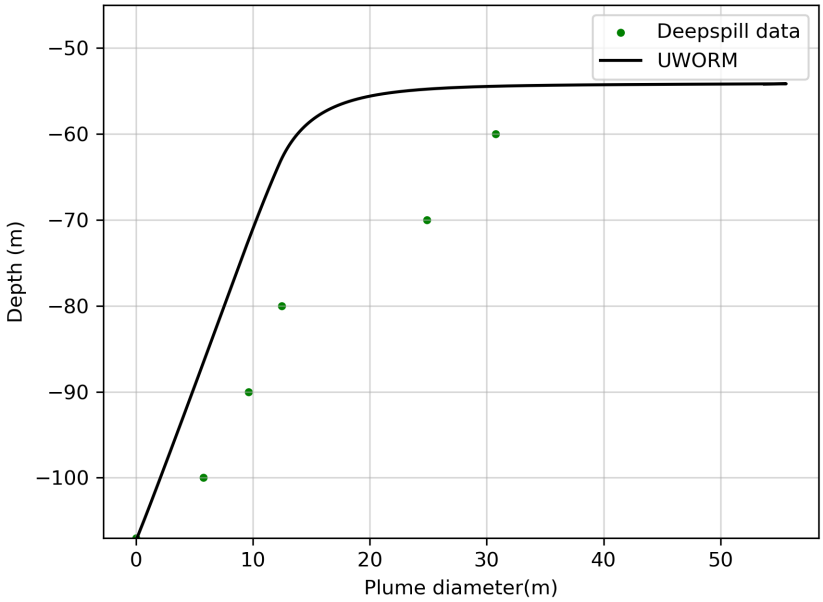

Figure 3.8: North Sea Experiment: Plume diameter comparison between UWORM-1 and data. With the entrainment coefficient in (Yapa et al., 1999) diameter is underestimated.

Sensitivity to entrainment parametrization

The entrainment parametrization by Yapa and Li (1997), despite predicting the intrusion level, uncovered key discrepancies: an underestimation of the plume diameter and an overestimation of the plume velocity.

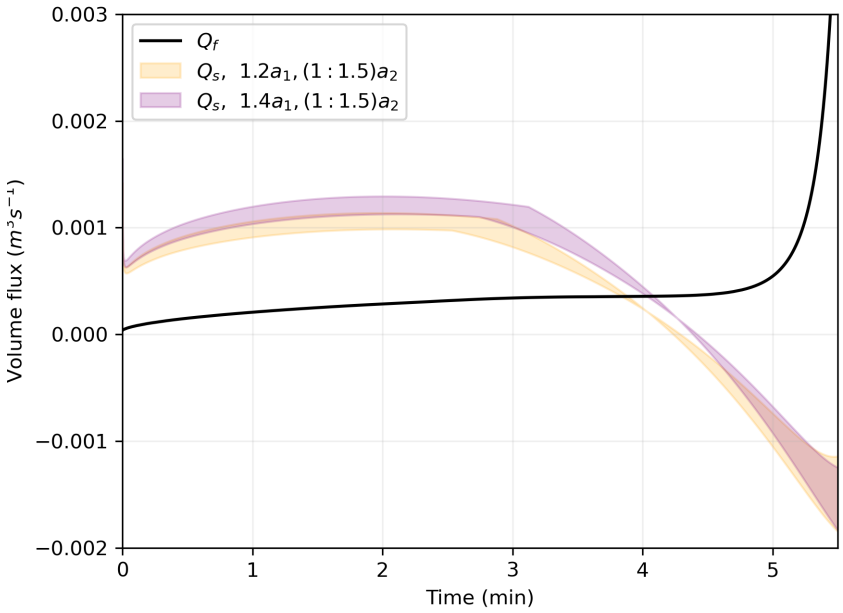

Figure 3.9: North Sea experiment calibration: the shear (orange-purple) component can be tuned via the entrainment coefficient α, while the forced (black) component is fixed.

Some considerations can be drawn in the limiting case $u_a = 0$, where $Q_f = 0$, the plume trajectory is purely vertical $(v_\phi = 0)$, and the volume flux entering the plume is only the shear one. This one simplifies to $Q_s = 2\pi bh\alpha|\vec{v}|$, and the entrainment coefficient α becomes:

$$\alpha = a_1 + a_2 F_d^{-2} = a_1 + a_2 \frac{g'b}{|v|^2}$$

Without ocean currents, the entrainment is inversely proportional to the squared Froude number (# would be interesting to plot F). The two parameters a_1 and

a_2 are the intercept and the slope. The first parameter, a_1, determines when the entrainment is zero, delaying the entrainment/detrainment transition. The second parameter a_2 tunes the magnitude.

With currents, the shear entrainment coefficient becomes $\alpha(a1, a2, a3)$ as in Eq. 3.4. Beyond the shear, the presence of ocean currents gives a forced flux Q_f. The total flux is $Q_e = \max(Q_s, Q_f)$. It is interesting to assess the predominancy of the fluxes Q_s and Q_f in time: in proximity to the discharge (in the first stage) or in presence of very weak currents, the shear flow dominates. By comparing Fig. 3.9 and Fig. 3.6, the shear vanishes after the neutral buoyancy condition and before the terminal level. Here we find the transition from shear-dominated to forced-dominated (at $\sim$4 min).

Then the forced flux takes over, as the windward portion of the plume surface enlarges. The forced flux contribution prevents the overall flux from turning negative (in other words there is no detrainment; rather, only positive entrainment). Since we want to calibrate the near-field phase, we need to adjust the shear entrainment. By tuning the coefficients a_1 and a_2 in Eq.3.4, we are able to delay the shear-forced transition, and to amplify the shear contribution. Figure 3.9 illustrates the shear flux, forced flux, and the total volume flux, with corrections applied on a_1 and a_2.

To address the underestimation in entrained mass we apply the following corrections (the parentheses [:] are intervals):

$$\begin{cases} a_1' &= [1.2 : 1.4]a_1 \\ a_2' &= [1 : 1.5]a_2 \\ a_3' &= a_3 \end{cases} \tag{3.14}$$

These corrections reflect in enlarged plume diameter (Figure 3.11 and Figure 3.10a), resulting in a better alignment with observations. Additionally, the plume's ascent is decelerated (Figure 3.10b).

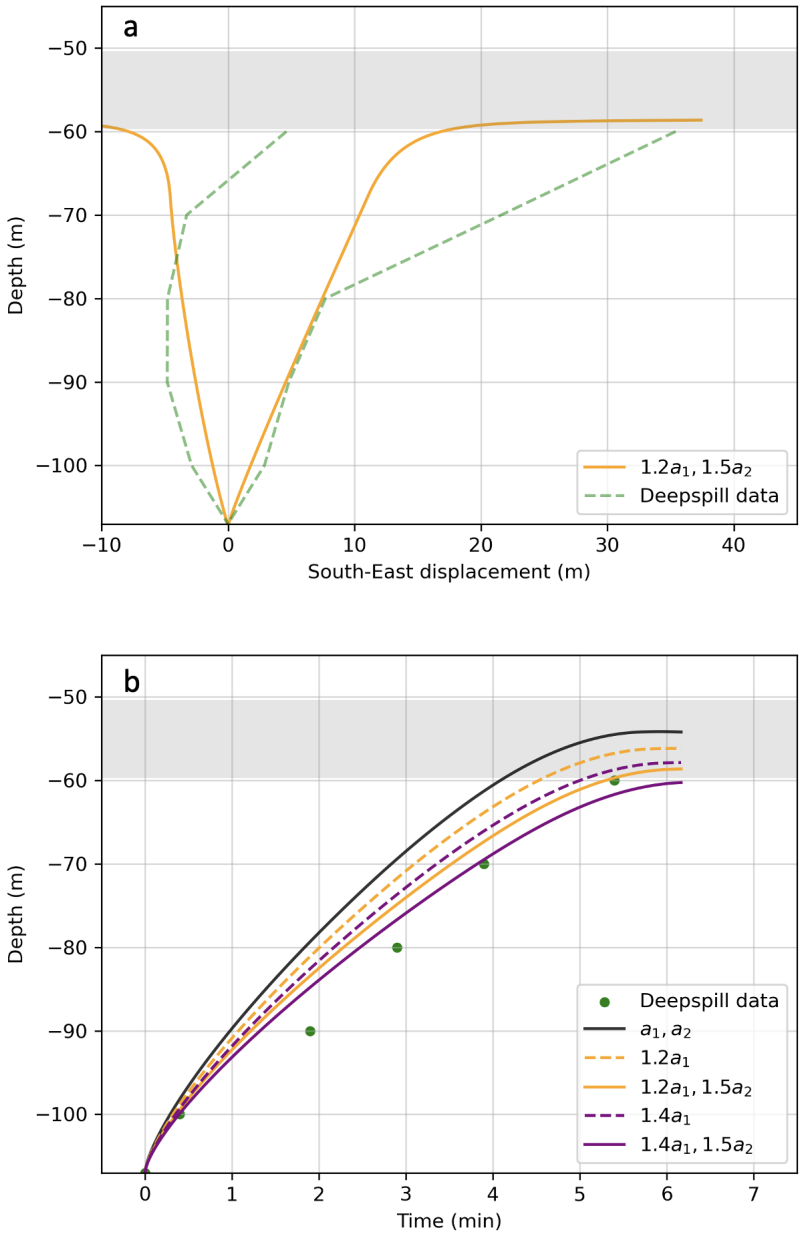

Figure 3.10: North Sea Experiment calibration: in **a**, the plume envelope, in **b**, the plume centerline position in time. Again, a comparison between UWORM-1 (black), data (green) is displayed. With calibration, the plume entrains more water, resulting heavier and slower.

In conclusion, we underline a potential underestimation of ocean currents from the CMEMS. While the plume diameter now matches the observed data, the trajectory

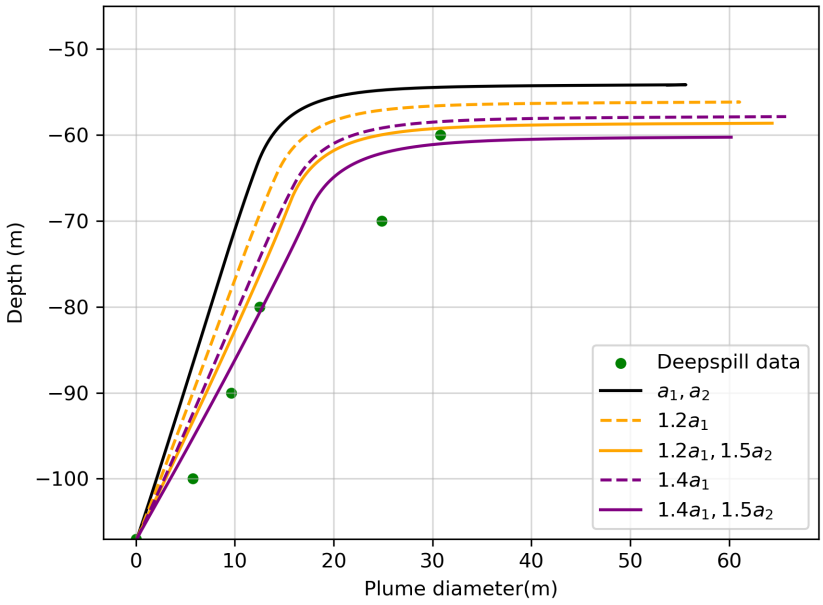

Figure 3.11: North Sea Experiment calibration: comparison of plume diameter from UWORM-1 and data. Augmented plume width.

should exhibit a greater curvature. Enhancing the currents could increase the total entrainment due to the higher forced flux.

3.7 Summary and conclusions

This chapter focused on the numerical modelling of subsurface oil spills in the near-field region via a plume model approach. We discussed the numerical modelling choices of a free-source UnderWater Oil Release Model (UWORM). UWORM is a Lagrangian elements plume model which captures the evolution of each element's properties over time, yielding outputs such as trajectory, shape, and oil concentration.

The model incorporates a parameterisation of turbulent seawater entrainment through 'shear' and 'forced' fluxes hypotheses. This causes the plume to entrain water, reducing the oil mass fraction and overall buoyancy. Subsurface released oil undergoes distinct phases, transitioning from a jet momentum-driven to a plume buoyancy-driven phase and eventually to a currents-driven phase. In stratified ocean conditions, the plume reaches a terminal level below the surface, concluding the near-field simulation when the plume element's vertical velocity becomes zero. A Python-based model was designed, employing initial and boundary conditions from CMEMS data interpolated at the plume location. The governing equations are solved using an RK-IV scheme. Validation of the near-field component of UWORM involved laboratory-scale cases in unstratified and stratified ambient, ensuring agreement in trajectory, oil concentration, and terminal level. Subsequently, simulations were compared with data from the NOFO experiment, allowing for the calibration of the inflowing shear flux.

In conclusion, the development and validation of UWORM could make significant contributions to rendering subsurface oil spill modelling universally accessible through the establishment of a clear and well-defined model.

In the existing literature, several plume models have undergone extensive validation and improvements. To align our model with the current state-of-the-art, the next step for UWORM will involve incorporating a gas component.

The simplicity of these models is advantageous, albeit with a few drawbacks. The coarse parametrisation of fluid dynamics hinders the resolution of unsteady flow features and reduces reliability as the terminal level is reached. Real oil plumes in the ocean exhibit intricate dynamics, involving processes such as detrainment. To address such complexities, alternative approaches have been employed (Yang et al., 2016b). While plume modelling is just a parametrisation of the real processes, it can be more effective in managing actual oil spill disasters due to its rapid adaptability to the specific accidental case.

Chapter 4

Far-field modelling and linking near-far field dynamics

4.1 Introduction

This chapter describes the far-field behaviour of a subsurface spill plume. Beyond a critical depth, termed the 'intrusion depth', the oil no longer ascends as a coherent self-similar structure (the UWORM Near field component of Chapter 3). Instead, the collective oil spill motion dissolves, and becomes a source of oil droplets that are transported by three-dimensional ocean currents.

The plume model output at the intrusion depth serves as the initial condition for a new component of UWORM, so called UWORM far-field model, which consider oil droplet transport dynamics. The near-field and far-field model components are coupled producing the simulation of the whole structure of a subsurface release from the jet to the plume to the oil slicks dynamics at different depths.

For the oil droplets dynamics, the model considers the fundamental advection-diffusion processes, which considers the three dimensional flow field. In addition, the oil droplets vertical advection should consider the vertical velocity associated

with the buoyancy forces determined by the specific size of the particles involved. In Section 4.2 we describe the Lagrangian Particle Tracking (LPT) for oil droplets in the far-field. In Section 4.3 we describe how we designed the coupling between near and far field regions, and the particular choice we made for DSD in this work. Finally, in Section 4.4 we present a coupled near and far-field simulation for a realistic hypothetical scenario in the Southern Adriatic Sea. A discussion and conclusion section completes the chapter.

4.2 Lagrangian Particle Tracking for oil spills

The primary drivers of particle movement in the ocean are currents. These impact particle transport through advection and turbulent diffusion. If the particles are buoyant, buoyancy must also be considered. The physical representation of this problem is the evolution equation of particle concentration, specifically, the advection-diffusion equation, which can be modified to include buoyancy effects. Various numerical methods, such as finite difference and finite element methods, can be used to solve this equation, but they often face stability issues due to numerical diffusion and struggle with non-uniform flow fields (Bennett and Clites, 1987). Moreover, they can be computationally intensive. In contrast, Lagrangian Particle-Tracking (LPT) methods accurately represent the physical diffusion processes and are computationally efficient. They in fact provide higher-resolution of the transported concentration compared to Eulerian models, limited by the mesh resolution of the Ocean General Circulation Model (OGCM) advecting velocity field. Secondly, they are faster as focusing only on the region affected by particle presence rather than the entire domain.

Initially applied to ocean and atmospheric transport (Csanady, 1973), LPT methods have since been employed for tracking various passive tracers in the ocean, including pollutants like oil (Elliott, 1986; Johansen, 1984; Al-Rabeh et al., 1989), plastic, biological particles such as larvae and phytoplankton, as well as sediments originating from land. LPT has gained popularity for addressing these diverse issues, other than for its compatibility with ocean hydrodynamics models. Passive parcels are assumed to be small compared with the smallest dynamical scales and neutrally buoyant, so that are transported by the Eulerian current fields, at a specified resolution. Therefore, the resolution of the Ocean General Circulation Model (OGCM) plays a crucial role, as initial errors tend to amplify.

The LPT approach follows the trajectories of individual particles over time, pro-

viding insights into turbulent dispersion (through a random-walk process) and transport. As a first-order approximation, particles are treated as passive tracers subject to transport and diffusion. However, this approximation is inadequate in our case, as the specific behaviour of oil is crucial. Surface weathering processes, such as evaporation, emulsification, and dispersion, significantly alter the chemical and physical properties of an oil slick. Early oil spill models used Mackay's weathering algorithm (Mackay and Leinonen, 1977a), as demonstrated by Lardner in a simulation of the Arabian Gulf (Lardner et al., 1988). Subsequent models, like OILPOL (AI-Rabeh et al., 1995) and OILMAP (Spaulding et al., 1994), evolved from this approach. Medslik-II (De Dominicis et al., 2013a,b) introduced a two-step algorithm: a smaller step for the advection and diffusion of individual particles (via a Lagrangian stochastic equation) and a larger step for the overall slick fate processes. In subsurface spills, buoyancy is a critical factor to consider. Oil parcels are not neutrally buoyant, as their density is typically lower than that of seawater. Beneath the surface, the primary deviation from seawater particles stems from the specific oil density, introducing a buoyant drift to the vertical motion (Yapa et al., 1999) (Dasanayaka and Yapa, 2009). In the following, we describe briefly the LPT method, applied to the advection and diffusion equation.

Advection-diffusion equation

Let us consider a scalar field $C(\vec{x}, t)$, representing the probability density function of a particle position in time. If the particle is immersed in a moving fluid, it will be subject to a drift force and molecular diffusion resulting from collisions with the fluid particles. In the ocean, the Reynolds approximation allows to write the equation for the mean component of C, while smaller turbulent components are parametrised as turbulent processes. Therefore, the turbulent diffusion term substitutes the molecular one which is several orders of magnitude smaller (Fischer

et al., 1979).

Being the 3D flow field $\vec{v}_a(\vec{x},t)$, and the diffusivity tensor, symmetric and positive definite **D**, and the buoyant velocity w_b, the advection-diffusion equation is

$$\partial_t C + \nabla \cdot [(\vec{v}_a + w_b\hat{k})C] = \nabla \cdot (\mathbf{D}\nabla C) \tag{4.1}$$

The PDE (4.1) of advection-diffusion for the concentration field, can be interpreted as a Fokker-Planck equation for the probability density field. This one is equivalent to a stochastic differential equation (SDE) for single-particle evolution or Langevin equation (Gardiner et al., 1985). While the former is solved using Eulerian methods, the latter is addressed with Lagrangian approaches (Hunter, 1987).

In LPT, diffusion is represented as a random-walk (generally a white noise term) in the position equation:

$$\frac{d\vec{x}}{dt} = \vec{\xi}(t) \tag{4.2}$$

where $\vec{\xi}$ is the 3D white noise, with mean $< \vec{\xi}(t) >= 0$ and autocorrelation $< \vec{\xi}(t)\vec{\xi}(t') >= \delta(t-t')$. Applying the Itô hypothesis for the noise, and considering buoyancy, the SDE for the particle position is (Shah et al., 2011):

$$d\vec{x} = (\vec{v}_a + w_b\hat{k} + \nabla \cdot \mathbf{D})dt + \sqrt{2}\mathbf{V}\, d\vec{W}(t) \tag{4.3}$$

being the 3D Wiener increment $d\vec{W}$ normally distributed (for each component i, the mean is $< dW_i = 0 >$ and variance is $< dW_i^2 >= dt$), while $\mathbf{V}\mathbf{V}^T = \mathbf{D}$. In general, **D** is space-dependent and is needed also in the advection term Gräwe (2011). In the simplified case where **D** is diagonal and spatially-constant, we can write

$$d\vec{x} = \begin{bmatrix} u_a \\ v_a \\ w_a \end{bmatrix} dt + \begin{bmatrix} 0 \\ 0 \\ w_b(d,\rho_{oil}) \end{bmatrix} dt + \begin{bmatrix} \sqrt{2D_h} & 0 & 0 \\ 0 & \sqrt{2D_h} & 0 \\ 0 & 0 & \sqrt{2D_v} \end{bmatrix} d\vec{W}(t) \tag{4.4}$$

We indicated the dependency of the vertical buoyant velocity on the droplet diameter d and the oil density ρ_{oil}.

The diffusivity values are often retrievable from Ocean General Circulation Models (OGCM) or can be calculated with dedicated turbulence models. In general, on large scales (or coarse resolution OGCMs), we should consider a high horizontal diffusivity D_v. The scale of the modelled process, in our case of the oil slick, should therefore be compared with the scale of the ocean model in order to assess the horizontal diffusion value (Nepstad et al., 2022). For the vertical diffusion D_v, it is important to consider a reduced mixing where the vertical density gradient is high. This results in a step-function, with a higher value in the mixed layer and a smaller value in the stratified region (within the pycnocline) (Nordam et al., 2021). Diffusivities for oil spills, provided by (De Dominicis et al., 2013a), are $D_h = 1 - 100\,\mathrm{m^2 s^{-1}}$ for the horizontal component, and

$$D_v = \begin{cases} 0.01\,\mathrm{m^2 s^{-1}} & \text{above thermocline} \\ 10^{-4}\,\mathrm{m^2 s^{-1}} & \text{below thermocline} \end{cases} \tag{4.5}$$

for the vertical component.

The horizontal currents velocity $\vec{v}_a = (u_a, v_a)$ at the particle position is interpolated from the OGCM mesh. Most ocean models assume incompressible flow, therefore the vertical velocity component w_a can be computed via the continuity equation (see Appendix A.3 Ocean vertical velocity computation). We calculated the ocean vertical velocity w_a for a given date in the Mediterranean Sea in Figure 4.1. As we can note, it ranges between $10^{-7} - 10^{-5}\ \mathrm{m\,s^{-1}}$ (several orders lower than the horizontal velocity $10^{-2} - 1\ \mathrm{m\,s^{-1}}$).

The numerical model used to solve equation (4.4) for the far-field dynamics is OceanParcels (Lange and Van Sebille, 2017), an advanced simulation tool to model the movement of particles through marine environments. This Python-based framework allows for Lagrangian particle tracking, leveraging oceanographic data from sources like satellite feeds or ocean circulation models to predict trajectories

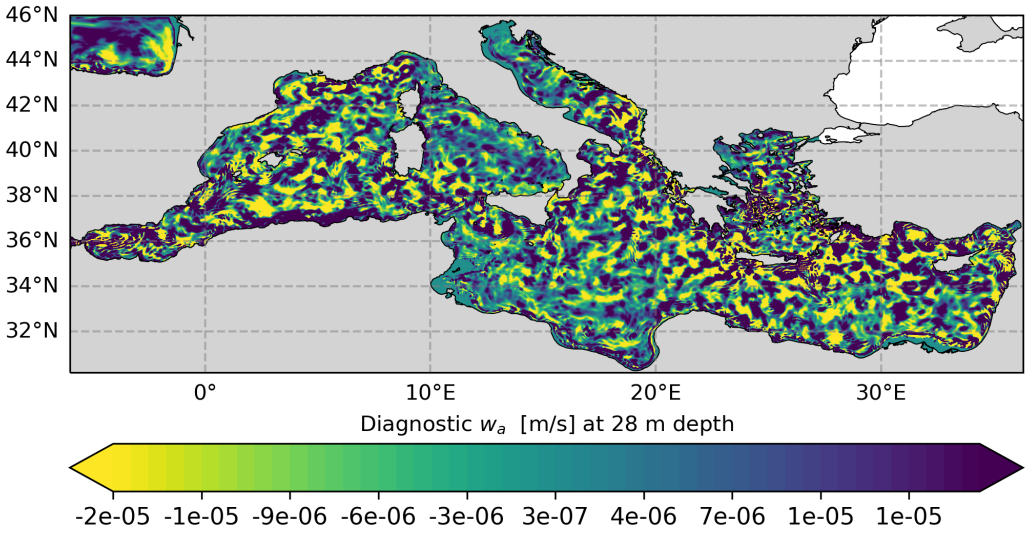

Figure 4.1: Ocean vertical velocity in the Mediterranean Sea, computed from the horizontal velocity components through the continuity equation for August 1,1995 retrieved from Copernicus Marine Service (Coppini et al., 2023).

affected by currents and other forces. It is highly customisable, enabling users to simulate complex biological behaviours and chemical processes. It is applied to phenomena ranging from plastic pollution dispersal to larval fish migration. This allowed us to inserting a buoyant vertical velocity term into the model, calculated from droplet sizes. OceanParcels is able to use ocean model data with different meshes, from Arakawa-A to Arakawa-C grid and offers capability of integrate the horizontal motion or adding the vertical ocean velocity component. The SDE is solved using an Euler-Maruyama (EM) scheme or a Milstein scheme.

4.3 Coupling near and far-field dynamics

In this section, we elucidate the coupling between the near-field plume model and the far-field Lagrangian model. In a stratified ocean, the oil plume gradually entrains seawater until it attains neutral buoyancy, then decelerating to a terminal

maximum level. In the far-field, a cloud of individual parcels is modelled.

Oil droplets, formed at the source level, are size-distributed depending on flow and ambient conditions, as detailed in Section 4.3.2. The mean diameter in the Deepwater Horizon spill, assuming that the oil was not treated with dispersants, would have been in the range of 800 to $10,000 \mu$m (Li et al., 2017). For example, if we consider $d = 1$ mm, then the droplet mass is approximately 1 g. For a typical oil spill of 10,000 tons, the total number of such droplets is of the order of $\sim 10^{10}$. This number is incredibly high and not applicable in simulations; it is not even useful. In this work, we make the assumption of super-particles. A super-particle has the same physical properties as the real droplet (size, density), but it represents a group of them. With a total number of super-particles $N = 10,000$, each super-particle represents $10^{10}/10^4 = 10^6$ or 1 million real droplets. The information on the representative amount is crucial for oil mass conservation: in this way, by knowing the total number of super-particles on the shore or under the surface, we can determine the total oil affecting those areas. In the subsequent discussion, we will refer to these entities as "super-particles" or simply "particles" within the scope of our modelling approach.

The depth of the terminal level serves as the initial depth for the far-field simulation, marking the initial position of the oil parcels. Given a number of oil particles N, the initial condition velocity is given by the interpolated fluid velocity at the initial position,

$$(\vec{x}_0^i, \vec{v}_0^i), i = 1...N$$

Oil particles are arranged at the intrusion depth in a horizontal circular area corresponding to the last cylinder circular face from the plume model. The diameter of such cylinder is less than few 100 meters. The cylinder thickness is of order 10^{-3} m and is neglected. The horizontal initial positions of the particles, represented by (x_0^i, y_0^i), are considered to be uniformly distributed in the cylinder area. Alternative modelling choices, such as a x-y bivariate Gaussian distribution, can be considered

to account for a more realistic assumption. The uniform distribution is expressed as

$$\begin{cases} x_0^i &= r^i \cos(\gamma^i) \\ y_0^i &= r^i \sin(\gamma^i) \\ z_0^i &= Z_0 + L_{max} \end{cases} \tag{4.6}$$

where r^i is a random value between 0 and r_f, the final cylinder radius, γ^i is a random number between $0, 2\pi$, Z_0 is the release depth, and L_{max} the distance covered in the near-field ascent. While the horizontal velocity components are

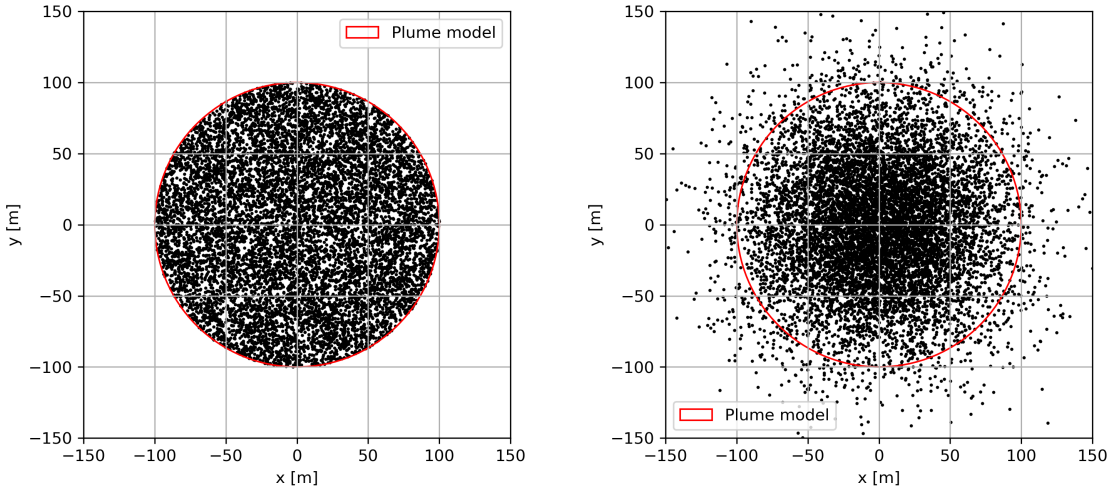

Figure 4.2: Initial particles position: (left panel) uniform distribution, (right panel) normal distribution. The plume final radius is marked in red.

simply the fluid velocity at the terminal depth, the vertical velocity is the sum of the fluid velocity and a buoyancy term w_t

$$w_0^i = w_{a0}^i + w_t^i \tag{4.7}$$

Considering that the resolution of available OGCM models is approximately on the order of ∼km, and given that the final plume cylinder radius is about ∼100 m, it is typically observed that the particles share a similar initial drift velocity as they are all located within the same OGCM grid cell ($\vec{v}_a^i = \vec{v}_a$ for all i in N). As the particles

begin to spread over, and with the use of progressively higher resolution models, each particle will be driven by different ocean velocities.

4.3.1 Droplets buoyant velocity

Oil droplets exhibit a buoyant vertical velocity arising from the lower density of oil compared to the surrounding water. A buoyant droplet ultimately attains a constant terminal velocity as described by the Stokes law, where the drag force opposing motion through water balances the upward buoyancy force. The mass of a spherical droplet with diameter d and density ρ, is given by $m = \rho\frac{1}{6}\pi d^3$. In ambient water density ρ_a, the droplet experiences a buoyancy force characterised by:

$$F_b = mg' = \frac{1}{6}\pi d^3(\rho - \rho_a)g \tag{4.8}$$

On the other hand, the drag force depends on the body velocity, denoted as $|\vec{v}| = v$, and it varies linearly or quadratically based on the flow's turbulent or laminar nature. It is defined as:

$$F_D = -\frac{1}{2}\rho C_D A w^2 \tag{4.9}$$

where C_D is the drag coefficient and A is the cross-sectional area of the body. For a spherical object of diameter d, the drag force is $F_D = -\frac{1}{2}\rho C_D \pi \frac{d^2}{4} w^2$. Computing the balance $F_D + F_b = 0$, the terminal vertical velocity is found to be (Zheng and Yapa):

$$w_t = \left[\frac{4}{3}\frac{d}{C_D}(1 - \frac{\rho_a}{\rho})g\right]^{1/2} \tag{4.10}$$

To define the drag coefficient, we introduce the Reynolds number, commonly employed as an indicator of fluid turbulence. This dimensionless number, representing the ratio of inertial to viscous forces, can be expressed as:

$$Re = \frac{w^2/d}{\nu w/d^2} = \frac{wd}{\nu} \tag{4.11}$$

where $\nu\,[\mathrm{m}^2/\mathrm{s}]$ is the kinematic viscosity and d is the diameter of the droplet, considered to be a sphere. Experimental measurements of the drag coefficient

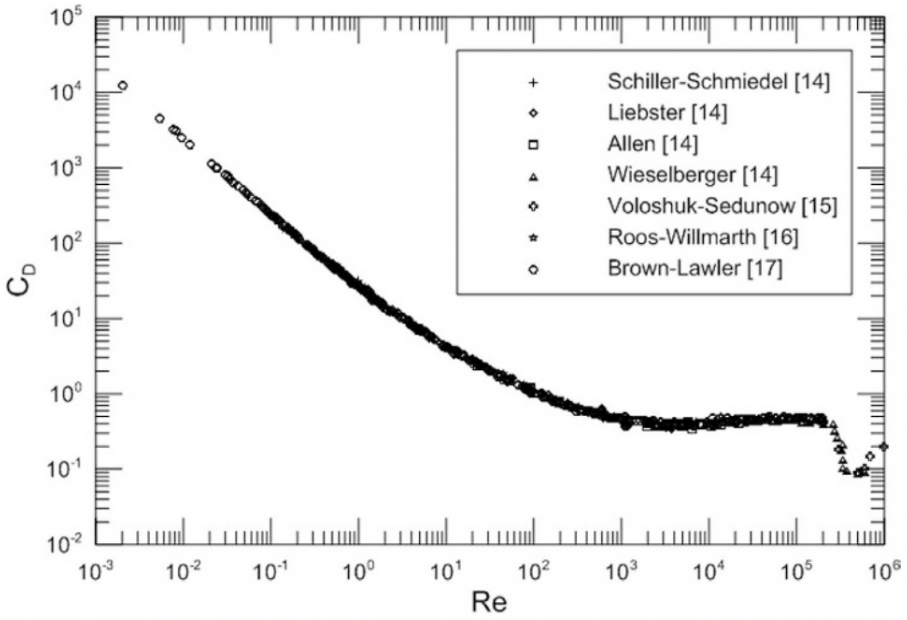

Figure 4.3: Customary drag coefficient for spheres as a function of the Reynolds number, from (Duan et al., 2015). The transition from a laminar to a turbulent regime is for $Re \sim 3 \cdot 10^5$.

(Bello and Idigbe, 2015) extensively show a dependence on the Reynolds number of the type reported in Fig.4.3. For a laminar flow $(Re < 10^5)$, the drag coefficient is about inversely proportional to the Reynolds number $C_D \sim 24Re^{-1}(1+0.15Re^{0.687})$, whereas for a turbulent flow $(Re > 10^5)$ it is approximately constant $C_D \sim 0.44$ (Delnoij et al., 1997). The laminar to turbulent transition can be expressed, in particular, in terms of the sphere dimensions. Therefore, with equal parameters, a laminar regime corresponds to small droplets, a turbulent regime to large droplets. For the two cases, the terminal velocity is:

$$\begin{cases} w_t &= \frac{gd^2(1-\rho/\rho_a)}{18\nu} \text{ for } \quad d < d_c \\ &= \left[\frac{8}{3}gd(1-\rho/\rho_a)\right]^{1/2} \text{ for } d > d_c \end{cases} \tag{4.12}$$

Transition occurs for $Re \sim 10^5$. By equating the two formulations for the drag in the two regimes, it is straitghforward to find the critical diameter (Aravamudan et al., 1982):

$$d_c = \frac{9.52\nu^{1/3}}{g^{1/3}(1-\rho_d/\rho_a)^{1/3}} \tag{4.13}$$

In conclusion, the vertical buoyant velocity hinges on both particle density and diameter.

4.3.2 Droplets size distribution

Accurately determining the oil droplet size distribution (DSD) is crucial for ocean oil spill models, significantly impacting the overall model prediction (North et al., 2011). While early oil spill modelling often overlooked this aspect, recent decades have seen substantial progress in assessing oil droplet size (Nissanka and Yapa, 2018). First size distributions were inferred for oil slicks under breaking waves (Delvigne and Sweeney, 1989), while later also for subsurface oil spills.

Subsurface released oil undergoes fragmentation into smaller droplets due to interfacial instabilities, with this process continuing and influenced by turbulence until it reaches a near-steady distribution. Two common approaches to droplet size distribution modelling exist. The first category comprises "equilibrium models", predicting a stable droplet size after breakup evolution concludes (Wang and Calabrese, 1986; Hinze, 1955; Johansen et al., 2013; Chen and Yapa, 2007). The second category includes "population dynamic" or "phenomenological" models, capturing time-varying breakup and coalescence processes (Bandara and Yapa, 2011), with the widely known VDROP-J model falling into this group (Zhao et al., 2014).

Each category has its own set of advantages and disadvantages. In this study, we adopt an equilibrium model as our initial approach. Equilibrium models determine

a single distribution, regarded as the steady-state oil droplet size distribution (DSD). Typically, these models are developed by fitting a statistical distribution (e.g., Rosin-Rammler, log-normal) to experimentally observed oil DSD, as the ones in Masutani and Adams (2001). While early stages utilised uniform distributions (Proctor et al., 1994), continuous refinement has led to more sophisticated and suitable choices. Common DSD for subsurface oil blowouts are Rosin-Rammler (or Weibull) distribution and the log-normal distribution. Both have been used in subsurface blowouts contexts as they give good fit with observed data (Lefebvre, 1989). The Rosin-Rammler and the log-normal distributions have been tested by Brandvik et al. (2013) on data from tower tank experiments conducted by SINTEF. In Li et al. (2017) the log-normal distribution was calibrated for the DeepWater Horizon accident and the Deepspill experiments and validated through 23 tests from Tower Basin SINTEF experiments. If d is the diameter, the log-normal distribution is:

$$f(d) = \frac{1}{\sqrt{2\pi} d\hat{\sigma}} \exp\Big[- \frac{(\ln d - \hat{\mu})^2}{2\hat{\sigma}^2} \Big] \tag{4.14}$$

This is a two-parameters distribution. In fact it is characterised via the two parameters $\hat{\mu}$ and $\hat{\sigma}$, which are empirically evaluated. This distribution has the peculiarity of median $d_{50} = e^{\hat{\mu}}$. Therefore $\hat{\mu}$ value can be empirically estimated (considering disruptive and restorative forces of the release) via a characteristic diameter $\bar{d} = d_{50}$. The Weber number is the ratio between inertial forces (disruptive) and surface tension (restorative):

$$We = \frac{w^2/d}{\sigma/(\rho d^2)} = \frac{\rho w^2 d}{\sigma} \tag{4.15}$$

A higher Weber number is correlated with high surface instabilities which lead to ligaments and droplets formation.

The Ohnesorge number accounts for the viscosity effect and it can be expressed as combination of the Reynolds and Weber numbers:

$$Oh = \frac{\sqrt{We}}{Re} = \frac{\sqrt{\rho d/\sigma} u}{ud/\nu} = \frac{\mu}{\sqrt{\rho \sigma d}} \tag{4.16}$$

where μ is the dynamic viscosity $[\mathrm{kg}/(\mathrm{m}\cdot\mathrm{s})]$. An escalation in viscosity, signifying a greater resistance to droplet breakup, is manifested by elevated Ohnesorge numbers. In Fig.4.4 it is shown how the Ohnesorge and Reynolds numbers vary with the initial volume flux and nozzle diameter.

Among these three numbers (Re, We, Oh), just two of them are independent and

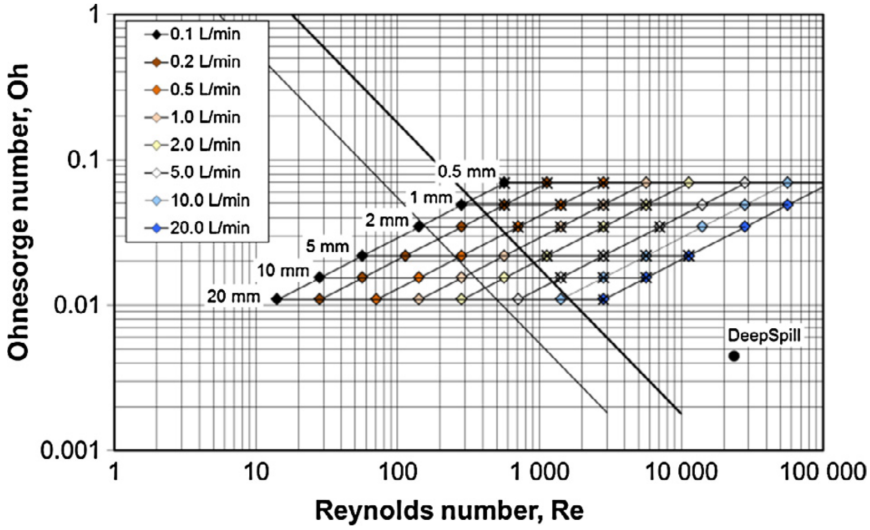

Figure 4.4: Diagram showing different initial volume fluxes (see colour legend) and nozzle diameters (Johansen et al., 2013) Different Ohnesorge and Reynolds numbers are obtained, with a transition between laminar and turbulent flow (solid diagonal line). On the bottom right, the DeepSpill experiment.

can be used to define a characteristic droplet diameter during a blowout release. For this work, we selected the one proposed by (Li et al., 2017), which has been empirically validated and proven satisfactory (Chiri et al., 2020)

$$\bar{d} = r \cdot d_0(1 + 10 \cdot Oh)^p We^q \tag{4.17}$$

with the parameters $r = 1.791, p = 0.460, q = -0.518$ determined through calibration in laboratory and real-scale experiments. This empirical definition state that droplet characteristic diameter increases with viscosity (through Oh numerator)

and surface tension (We denominator), while decreases with inertial forces. Finally, a maximum possible diameter d_0

$$d_0 = \min\left[D_0,\ 4\sqrt{\frac{\sigma}{(\rho_a - \rho)g}}\right] \tag{4.18}$$

is defined as the minimum between the Raileigh-Taylor instability diameter and the nozzle diameter. Both the distributions (Rosin-Rammler and log-normal) have been tested on a variety of data. In Figure 4.5, cumulative distributions are compared for different datasets, among the Deespill experiment, the DWH JF3 cruise and tank experiments (UH and BIO) (Li et al., 2017).

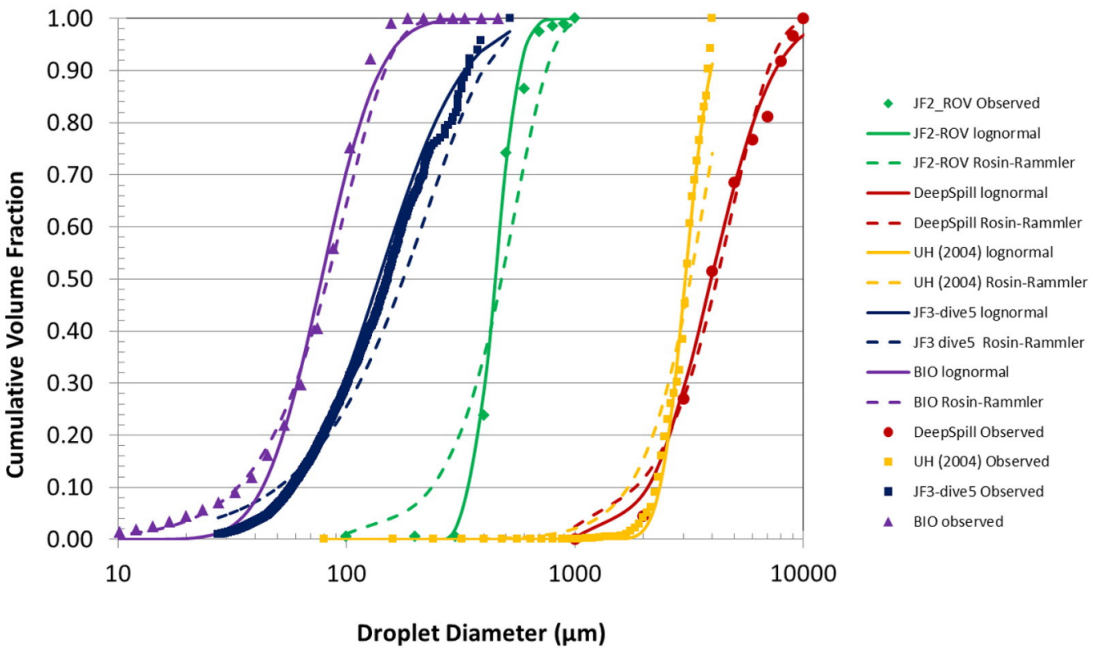

Figure 4.5: Summary of observed cumulative droplet size distributions of five different data sets, with the associated lognormal and Rosin-Rammler distribution fits to the droplet size data. (Li et al., 2017).

4.4 Deep-release scenario in the Southern Adriatic Sea

We qualitatively assess the UWORM simulation with coupled near and far field components with a case study involving a release scenario from the decommissioned Aquila 2 ENI oil platform (DGS-UNMIG, 2017), in the Southern Adriatic Sea.

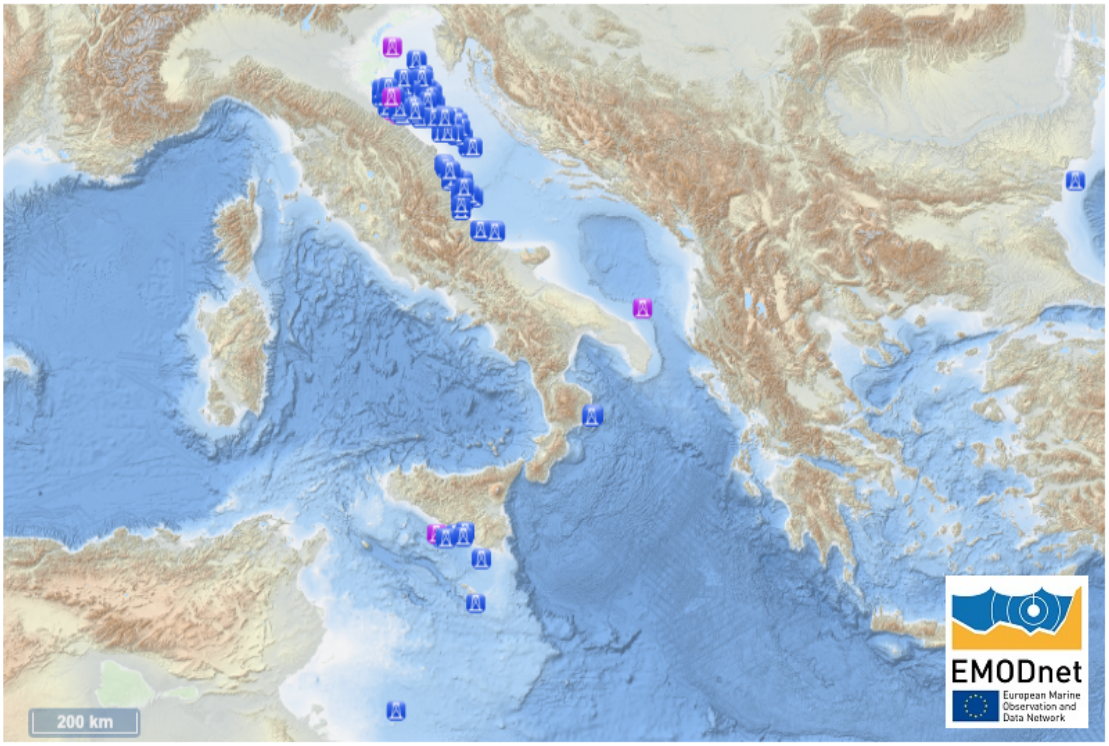

Figure 4.6: Offshore crude oil installations in the Adriatic Sea area. In purple, the dismissed platforms, in blue, the ones operational. Off Brindisi coast, the selected site Aquila 2 ENI platform (40.93018 ºN 18.32711 ºE). Courtesy of Emodnet.

Selected for its depth, the drilling rig, inactive since 2019, is situated offshore of the Brindisi coast, approximately 50 km from the coast. Situated in the Southern Adriatic Sea near the Otranto Strait, the site boasts an average depth of approximately 1000 m. In Figure 4.7 the Adriatic Sea circulation is portrayed. At the basin

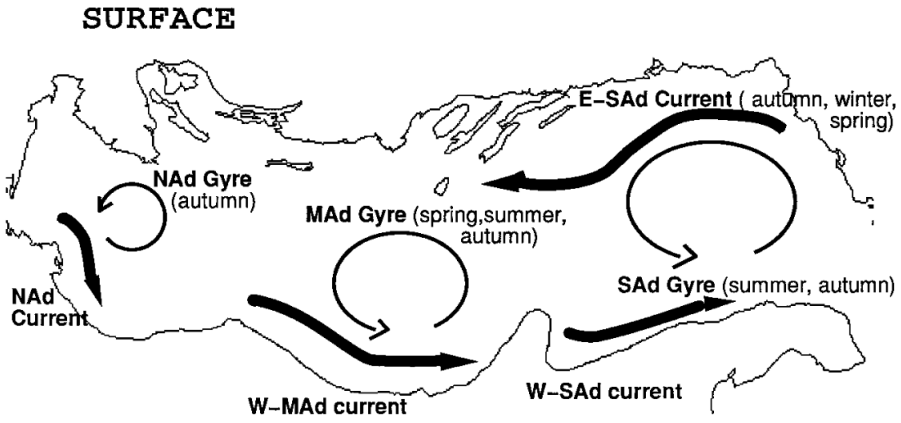

Figure 4.7: Schematics of the Adriatic Sea surface circulation from (Artegiani et al., 1997).

scale, the area experiences a prevailing cyclonic circulation, characterised by the Western Adriatic Coastal Current (WACC). This circulation is further intensified by the Southern Adriatic gyre (SAd), resulting in an overall southeastward current flow near the site.

In Table 4.1, the initial conditions are listed, including the nozzle radius b_0, discharge velocity V_0, oil concentration c_0, oil temperature, oil density ρ_{oil} at a reference temperature of $15.5°$C, the initial density difference with the ambient ρ_{a0}, and the depth-averaged stratification N^2 and Froude number F_0. While the platform coordinates and depth are retrieved from data ((DGS-UNMIG, 2017)), the information on the nozzle radius, the type of oil (crude oil), and the discharge velocity are assumed. These values are chosen based on a hypothetical scenario while maintaining realism. The relatively high Froude number signifies the importance of buoyancy compared to initial momentum. The release duration considered is 10 minutes, with the near-field simulation using a time-step $\Delta t = 0.25$ s. Given the discharge properties, the volume flux is $Q_0 = 0.016$ m^3/s, resulting in a total oil volume of approximately $V = 9.4$ m^3. The simulation commences on August 1st, 1995, at 12:00 CET. This timeframe was selected due to the significant extraction activity taking place at the Aquila2 platform during this period, thereby increasing

the risk of oil spills. The ocean data for the near and far models is the daily reanalysis provided by the Mediterranean Forecasting System Monitoring and Forecasting Center (Coppini et al., 2023).

In Table 4.1 are shown the initial conditions, including the nozzle radius b_0, discharge velocity V_0, oil concentration c_0, temperature T_0, oil density ρ_{oil} at reference temperature $15.5°$C, the initial density difference with ambient ρ_{a0}, and the depth-average N^2. These values are chosen accordingly to hypothetical scenario but with the constraint of being realistic. The relatively high Froude number indicates the effect of buoyancy with respect to initial momentum.

We consider a 10 min release and the near-field simulation is run with a time-step $\Delta t = 0.25$ s. Given the discharge properties, the volume flux is $Q_0 = 0.016\, m^3/s$, total oil volume is $V_{oil} \sim 9.4\, m^3$. The simulation starts on August, 1st 1995 at 12:00 CET. This timeframe is selected because it corresponds to the years when significant extraction activity was underway for the Aquila2 platform, and oil spill risk was higher. The ocean data for the near and far models is the daily reanalysis provided by a the Mediterranean Forecasting System Monitoring and Forecasting Center (Coppini et al., 2023).

The horizontal resolution is 0.042×0.042 (ca 4-5 km), while the vertical grid holds 141 unevenly distributed z* levels. Temperature, salinity, zonal and meridional velocity components are bi-linearly interpolated at the platform location giving the depth-profiles in Figures 4.8 and 4.9. Ocean vertical velocity component is computed diagnostically as shown in Appendix A.3 Ocean vertical velocity computation. The ocean density is calculated with the EOS-80 formula (Fofonoff and Millard, 1983).

The near-field model output is shown in Figures 4.10 and 4.11. In Figure 4.10 the plume envelope and center-line trajectory are displayed, together with the neutral buoyancy level and the maximum level of rise.

z_0	b_0	V_0	c_0	T_0	ρ_{oil0}	$\frac{\rho_{a0}-\rho}{\rho_{a0}}$	$\bar{N}^2$	F_0	Duration	Total oil
m	m	$\mathrm{m\,s^{-1}}$	/	$^\circ C$	$\mathrm{kg\,m^{-3}}$	/	$\mathrm{s^{-2}}$	/	min	$\mathrm{m^3}$
820	0.05	2.0	1	13	890	0.128	$7 \cdot 10^{-5}$	5.2	10	9.4

Table 4.1: Release and ocean variables: depth, nozzle radius, velocity, initial oil density, buoyancy, stratification, Froude number, total spill duration and oil volume.

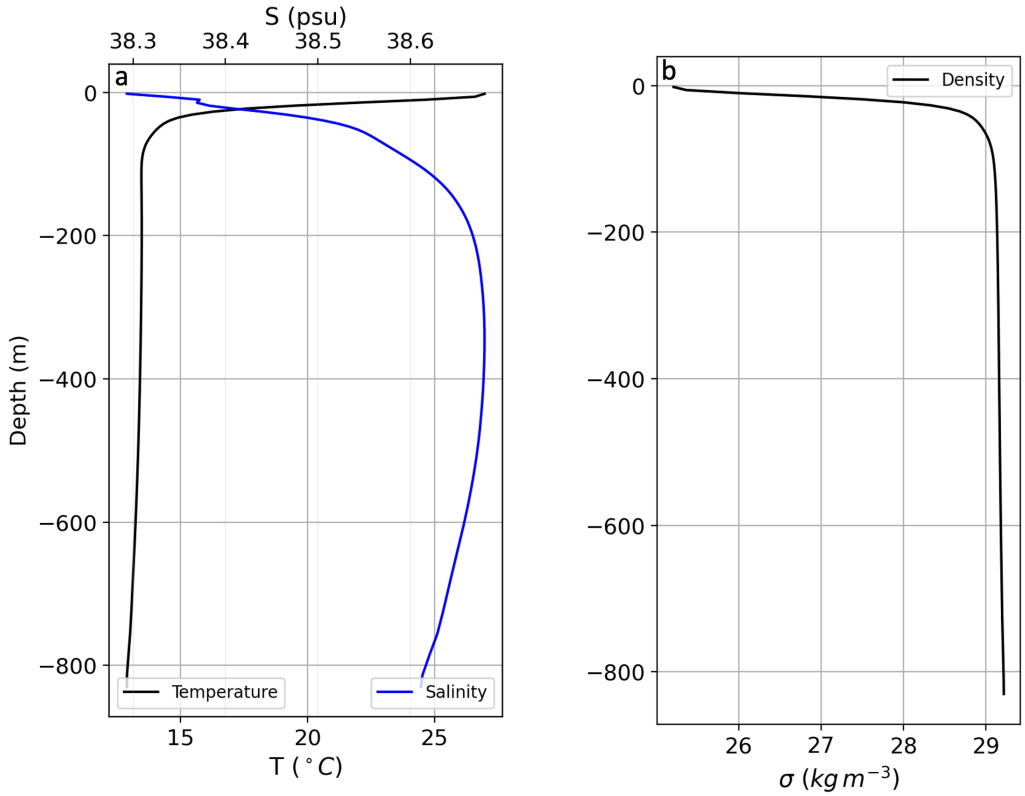

Figure 4.8: Ambient profiles of seawater temperature, and salinity (**a**), and density (**b**), on 01/08/1995 from interpolation at the release location.

In Figure 4.11 the reduced gravity, vertical velocity and position and oil concentration are shown. The reduced gravity and vertical velocity mark the neutral buoyancy and maximum level. Related correspondence is illustrated between Figure 4.10 and Figure 4.11. Neutral buoyancy is observed 1.9 hours after the first release, at a depth of ~ -189 m. The maximum level is reached 2.7 hours after the

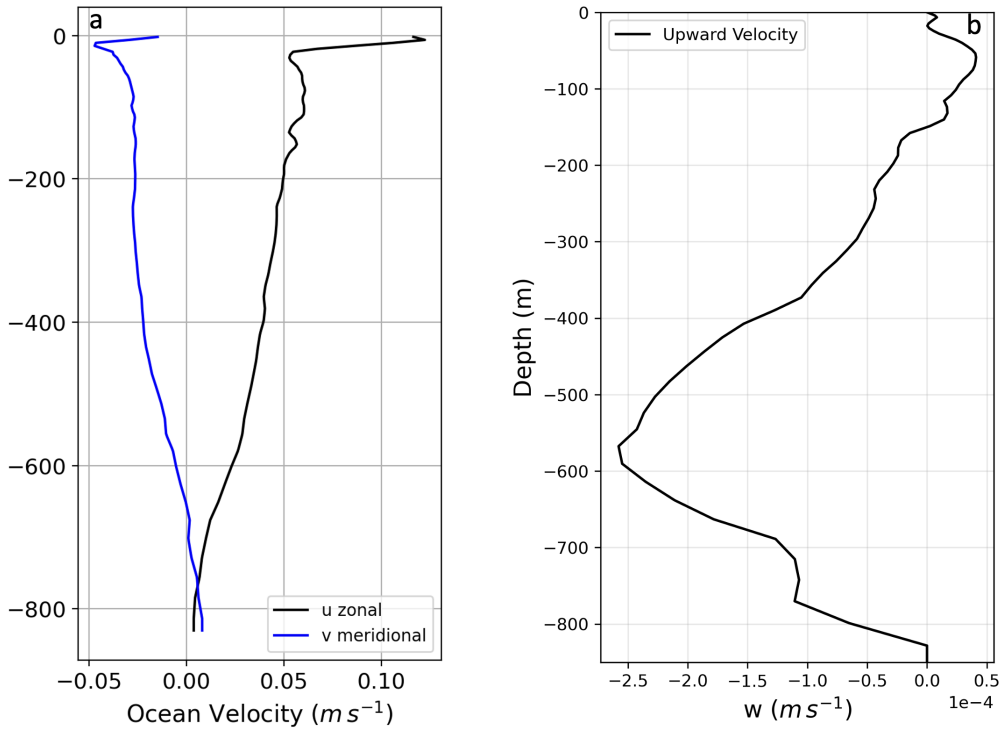

Figure 4.9: Ambient profiles of zonal and meridional velocity components (**a**), and upward vertical component (**b**), on 01/08/1995 from interpolation at the release location. The vertical velocity is computed diagnostically.

first release, at a depth of ~ -134 m. At this depth, the plume diameter is ~ 600 m, with south-eastward displacement due to ocean currents, with respective zonal and meridional $\Delta x \sim 300$ m and $\Delta y \sim -120$ m. Over time, the oil mass fraction, starting at 1 (indicating an entirely oil-composed plume), progressively diminishes as seawater entrains and mixes with the oil during the plume's ascent. Final state of the near-field is summarised in Table 4.2.

The final state of the near-field simulation serves as the initial condition for the far-field simulation. Each particle is assigned a size according to the log-normal distribution detailed in Section 4.3.2 (with parameters $\hat{\mu} = \ln d_{50}$ and $\hat{\sigma} = 0.5$). The median diameter d_{50} is calculated using Eq.4.17, with values from Table 4.1, interfacial tension of oil-water $\sigma = 0.019$ Nm^{-1}, dynamic viscosity $\nu = 0.009$ m^{2}s^{-1}

	z(m)	Δx(km)	Δy(km)	radius b (km)	time (hours)
Initial state	-820	0	0	$5 \cdot 10^{-5}$	0
End of near/Start of far	-134	0.30	-0.12	0.30	2.7
Surface state	0	4.06	-1.18	2.75	11

Table 4.2: Summary of initial state, intermediate (end of near and start of far field) and final state.

from Li et al. (2017). The DSD is shown in Figure 4.13**a** and the associated vertical velocity in Figure 4.13**b**, computed using Eqs. 4.12. A critical size d_c distinguishes the ensemble into a small size group ($d < d_c$) and a large size group ($d > d_c$). In the OceanParcels framework, a new kernel is implemented to accommodate particle behaviour, with buoyant velocity assigned to each particle based on size. With a typical diameter $d_{50} \sim 4$ mm, and being the total spilled volume $V_{oil} = 9.4\, m^3$, the number of real oil droplets would be approximately ~ 3 millions. A total of $N = 2500$ super-particles are chosen in this numerical simulation, each of them representing $\sim 100,000$ oil droplets and a volume of ~ 30 cm^3. The particles are sequentially initialised at the final plume depth, uniformly distributed within a radius equal to the final plume radius.

The far-field simulation spans approximately 9 hours, with a time-step $\Delta t = 5$ minutes. The daily reanalysis ocean data is interpolated at particles position. The horizontal eddy diffusion coefficient is set to $D_h = 10$ m^{2}s^{-1}, while no vertical diffusion is applied.

In the vertical, the buoyant velocity (Fig. 4.13**b**) is added to the ocean vertical velocity (Fig. 4.9**b**) as in Eq. 4.7. In the far-field interval -130 m $< z < 0$ m, the ocean velocity is upward and enhances the ascending buoyant motion. But the effect is limited due to the order of magnitudes involved ($w_a < 10^{-4}$m/s and $w_t > 10^{-3}$m/s), having an impact only for small particles.

In Figure 4.14 and 4.15 3D snapshots of the droplet cloud are displayed. The particles are initialised in the area marked by a circle (end of near-field state). particles are assigned a colour according to size in histogram Fig.4.13. The related Lat-Lon view is shown together with the ocean currents at depth.

After 15 (Fig.4.14 **A1-B1**) and 30 minutes (Fig.4.14 **A2-B2**), larger particles ($d >$ 4 mm) have emerged at the surface, while smaller ones ($d < 4$ mm) remain subsurface. The gradual ascent of particles is size-dependent, with complete resurfacing taking $\sim$ 8 hours (Fig.4.15 **A4-B4**). The horizontal displacement in the far-field simulation (before reaching the surface) ranges from hundreds of meters for the larger particles to $\sim$4 km in the south-east direction for the smaller particles. Results are summarised in Table 4.2.

In the future, work is to be done on statistics of the resurfacing and on uncertainties in simulations parameters (like particles number). The relatively low intensity of currents (see Fig. 4.12) during the selected time of year and location does not result in significant stretching and dispersion of the oil slick. Future work will involve trials with different ocean conditions and more accurate oil rig parameters.

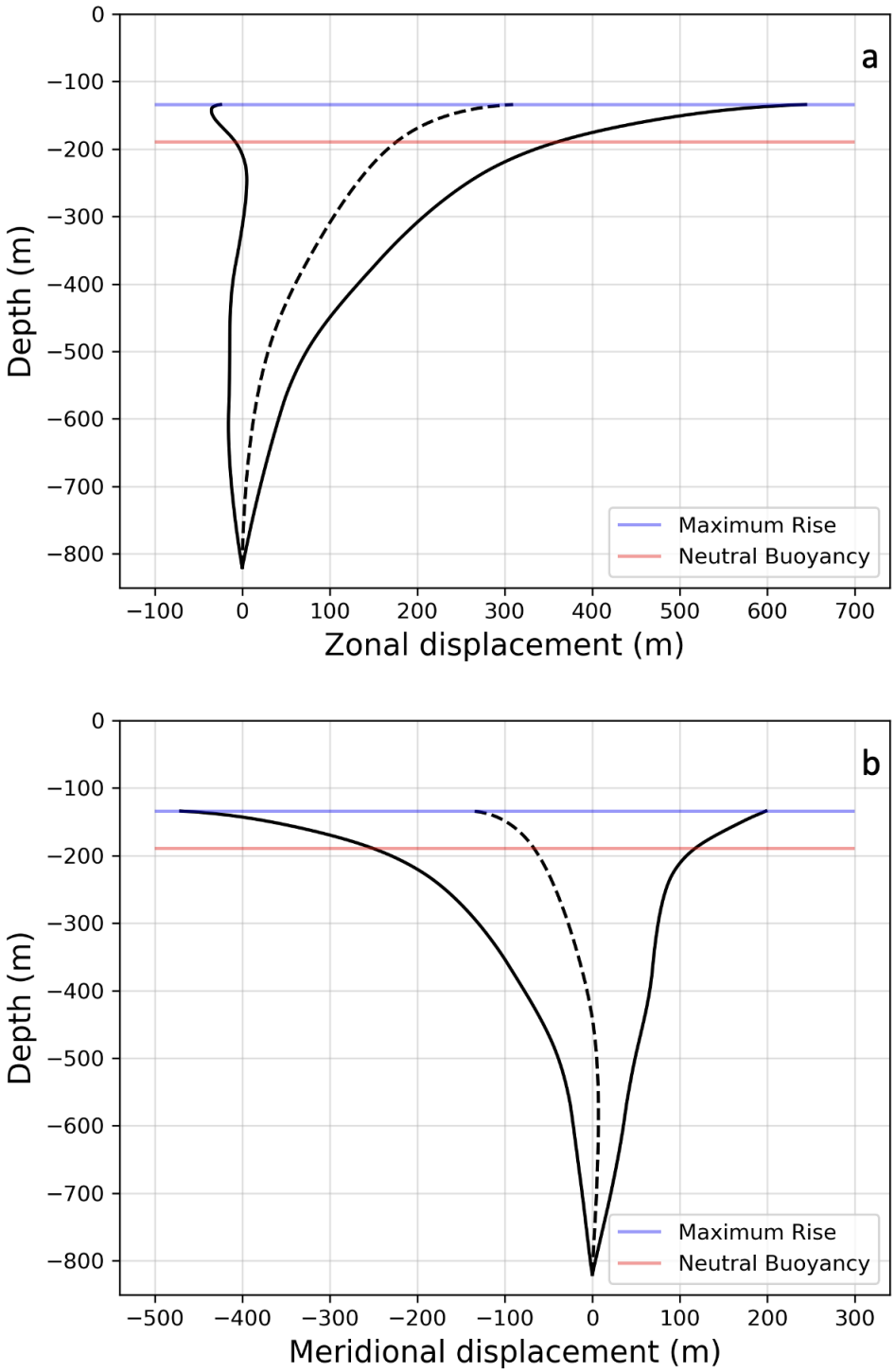

Figure 4.10: Southern Adriatic Sea near-field simulation: zonal (**a**) and meridional (**b**) transects of plume envelope and center-line trajectory. In (red), the depth of neutral buoyancy, in (blue), the maximum height of rise.

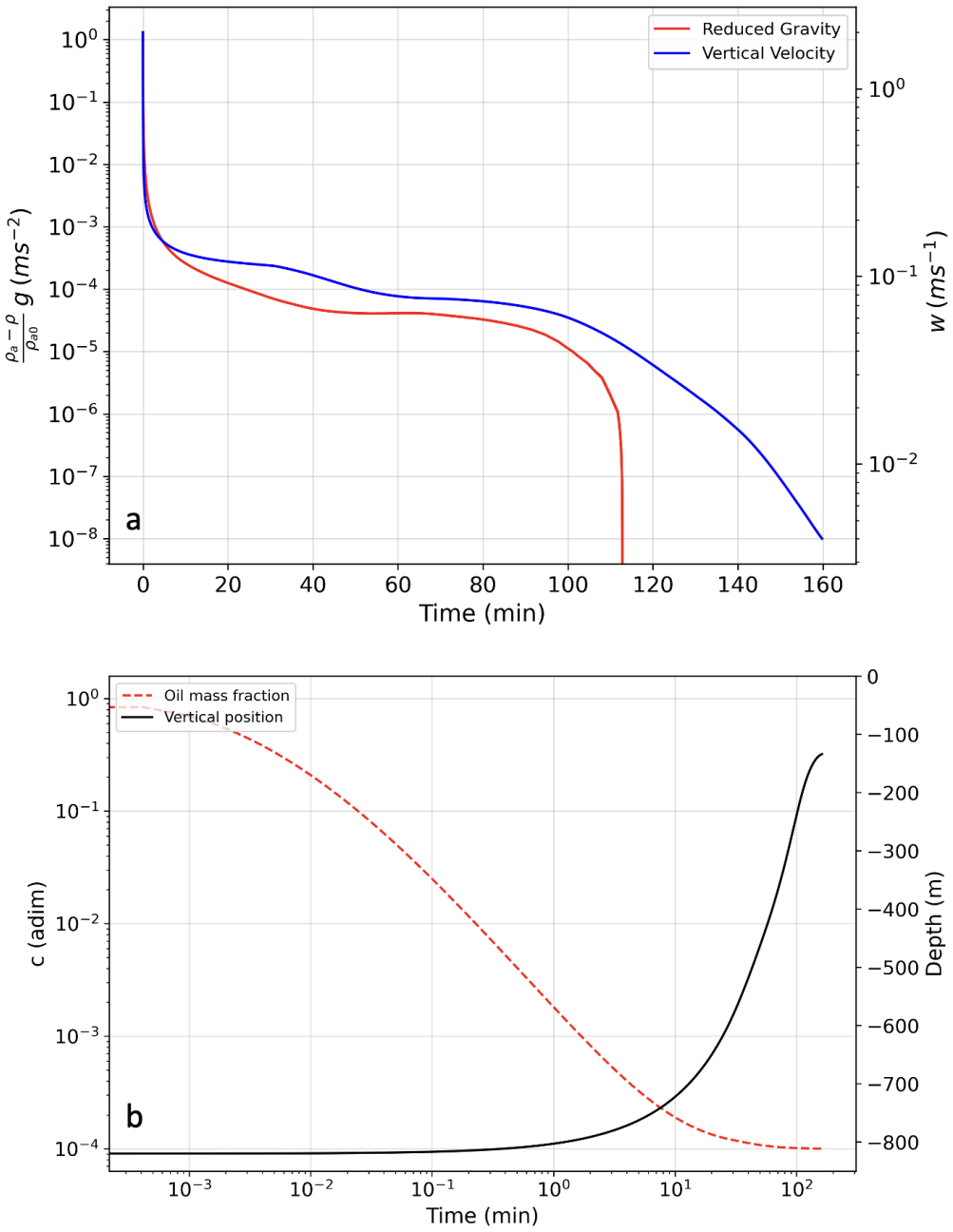

Figure 4.11: Southern Adriatic Sea near-field output: the evolution in time for (**a**), reduced gravity (solid red) and plume vertical velocity (solid blue), for (**b**), oil mass fraction c (dashed red) and vertical position (solid black). See correspondence with Figure 4.10 for neutral buoyancy and maximum rise level.

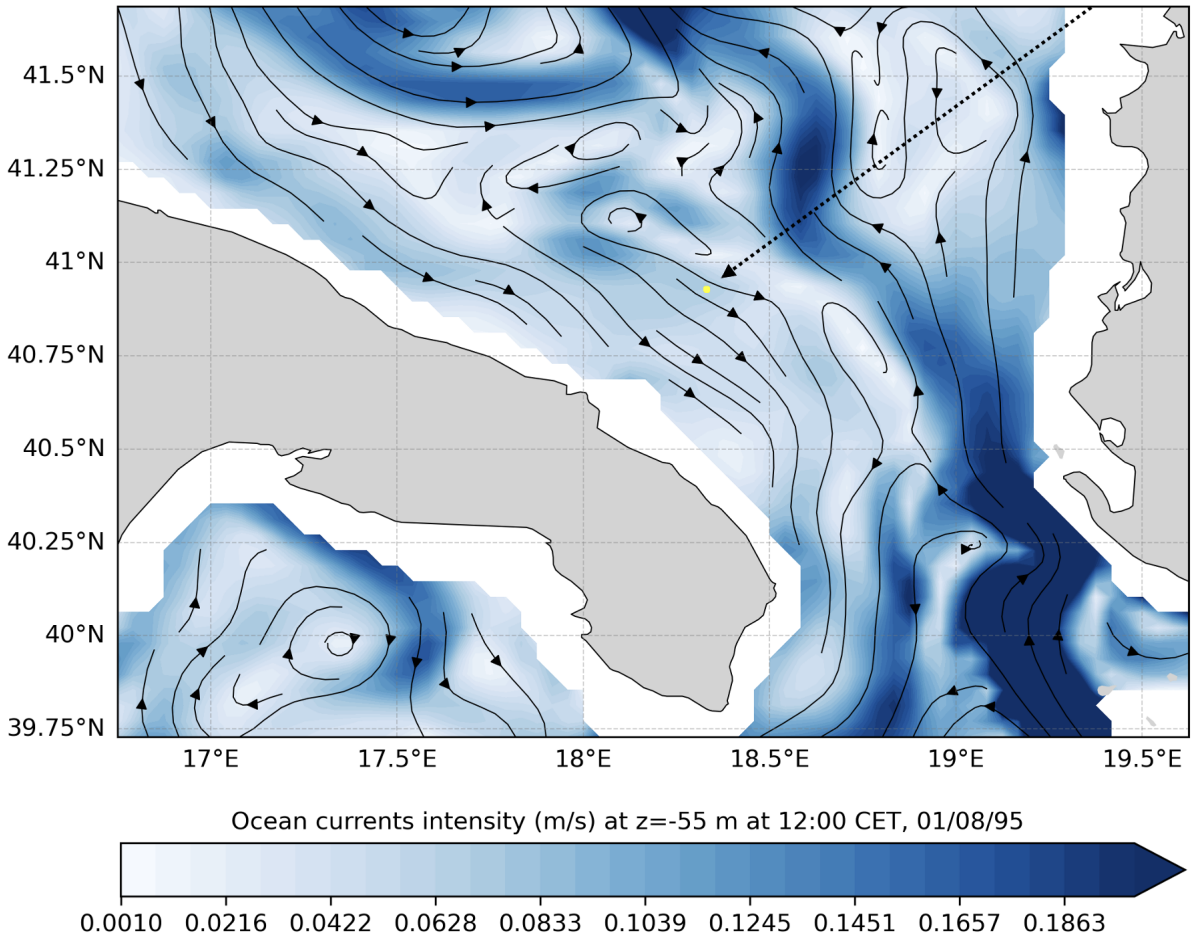

Figure 4.12: Southern Adriatic Sea ocean currents from CMEMS (Coppini et al., 2023) on 01/08/1995. In yellow, the final state of the near-field and initial state of the far-field, at depth z = -134 m.

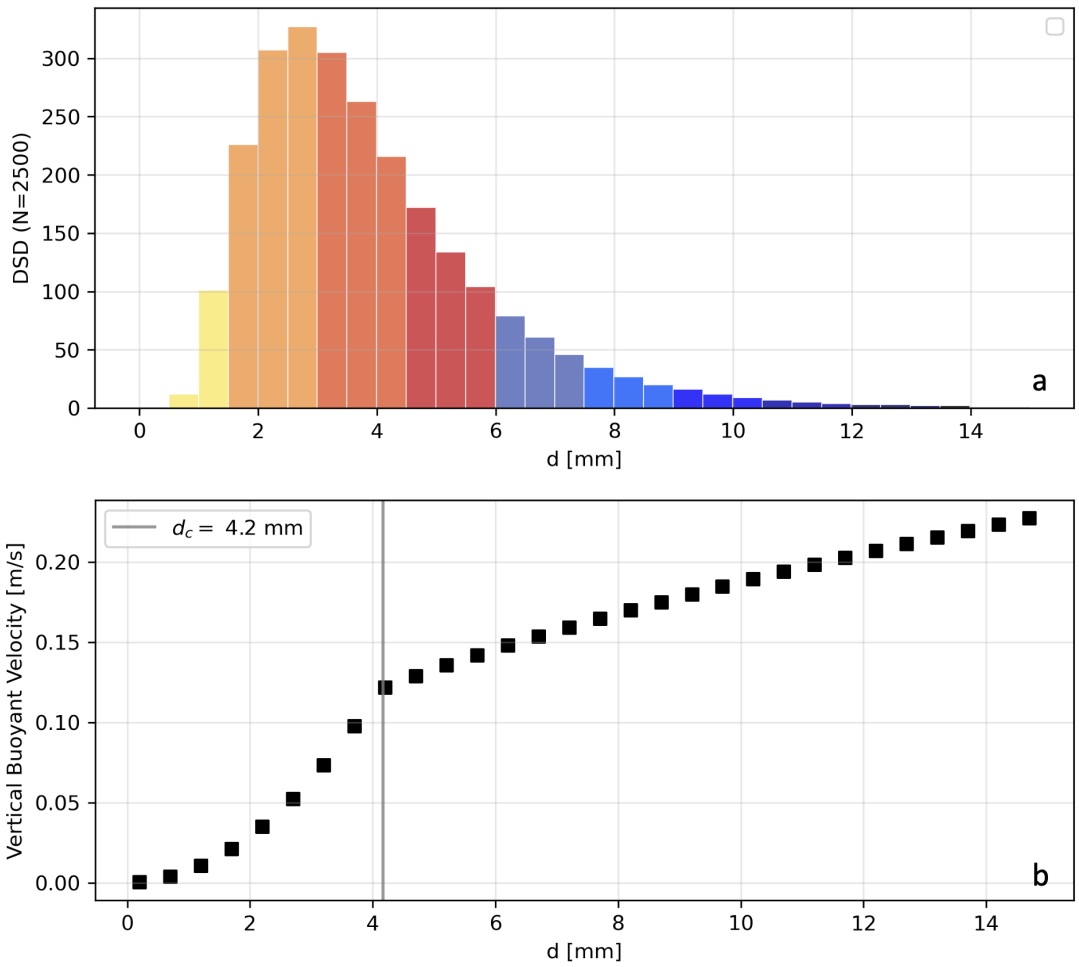

Figure 4.13: Southern Adriatic Sea near-far field coupling: in **a**, the Droplet Size Distribution according to a log-normal profile. In **b**, the buoyant vertical velocity associated to each size, with small droplets $d < d_c$ and large droplets $d > d_c$.

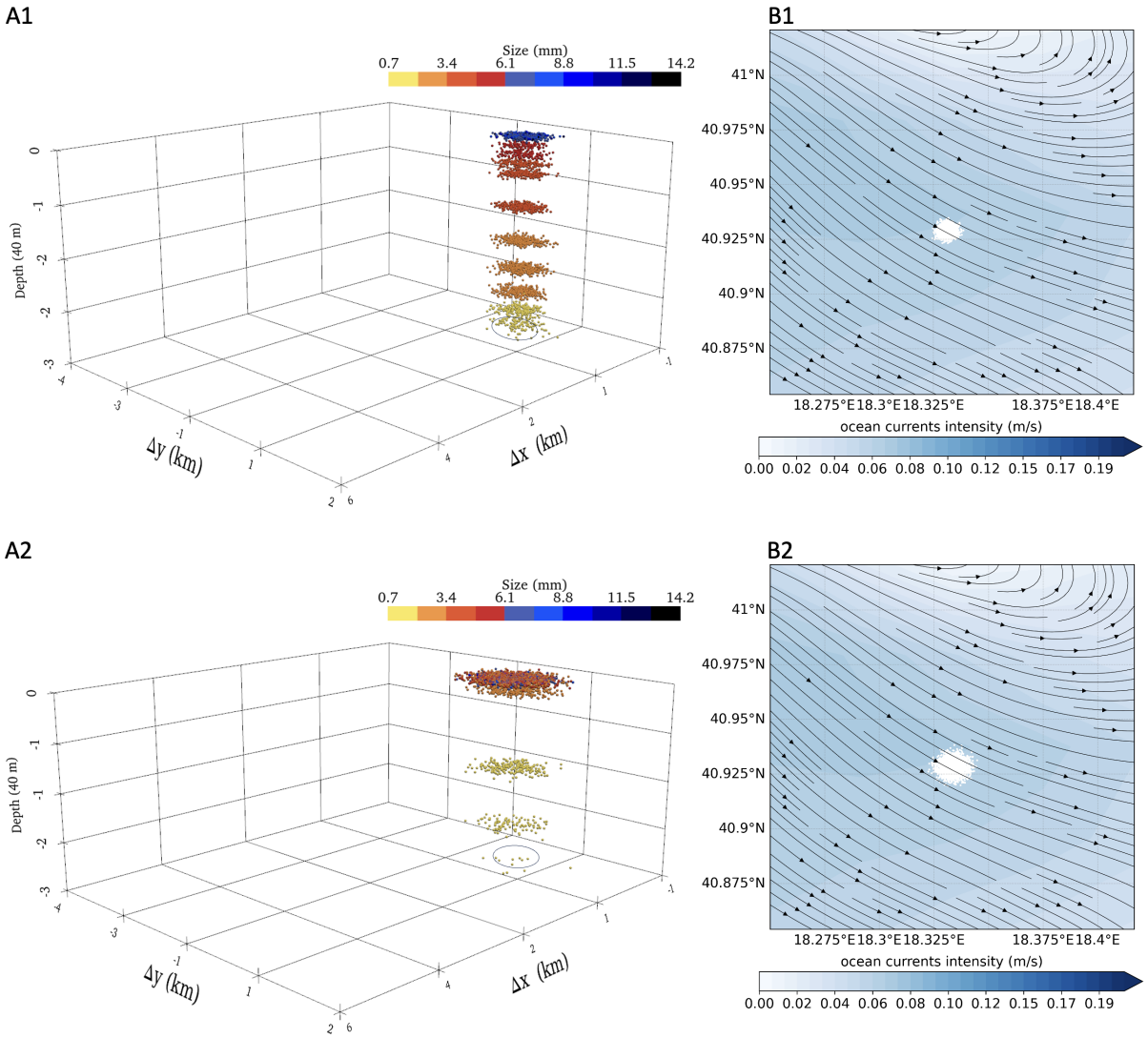

Figure 4.14: Far-field simulation in the Southern Adriatic Sea: (**A1-B1**) 15 min, (**A2-B2**) 30 min after end of near-field (black circle); droplet size is colour-coded with the DSD in Fig.4.13; in **B1-B2** ocean currents at z=-55 m and Lat-Lon view of the spill.

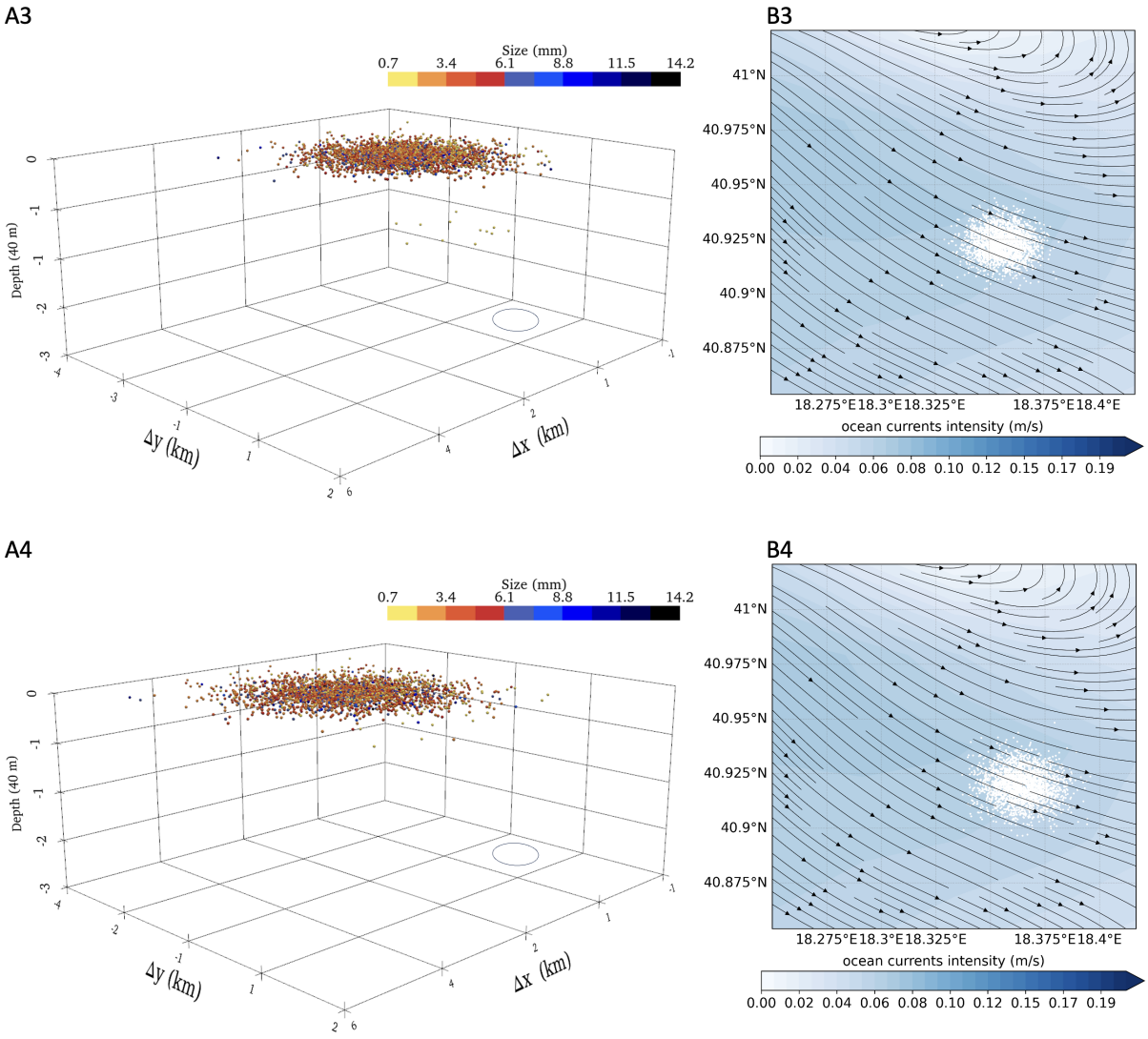

Figure 4.15: Far-field simulation in the Southern Adriatic Sea: (**A3-B3**) 6 hours, (**A4-B4**) 8 hours after end of near-field (black circle); in **B3-B4** ocean currents at z=-55 m and Lat-Lon view of the spill. Smaller particles persist longer subsurface.

4.5 Summary and conclusions

This chapter described the far-field component of UWORM model and the connection between the near-field component (in Chapter 3), and the far-field one. When ambient stratification is sufficient to induce subsurface intrusion, the collective representation of the oil particles in a plume ceases to hold. The plume's final state provides the particles' initial state, determining their initial position and spreading beneath the sea surface. Additionally, the characteristics of bottom discharge determine the particles size. Specifically, when oil fluid is released from an aperture in a damaged pipeline or from a nozzle in a drilling rig well, it breaks into filaments and particles. A droplet size distribution, which has shown a good fit with data, was chosen. In addition to being advected and dispersed by ocean currents, size plays a crucial role as it determines the buoyancy of these parcels and, consequently, the time to reach the surface.

In this study, we qualitatively assessed the near and far-field performance of our Underwater Oil Release Model (UWORM) in a case study involving the Aquila 2 ENI oil platform in the Southern Adriatic Sea in summertime. The chosen site, located offshore of the Brindisi coast at a depth of $\sim$ 800 m, offered an ideal setting for investigating near and far-field dynamics.

The near-field simulation revealed valuable insights into the plume's behaviour. The plume's trajectory, neutral buoyancy level, and maximum rise were calculated. The simulation also provided details on the plume's density over time, illustrating a transition from an oil-dominated composition to a mixture with seawater. The plume evolution lasted $\sim$ 2.7 hours. The near-field simulation's final state served as the starting point for the far-field simulation.

This phase involved the release of 2,500 particles, each assigned a size through a log-normal distribution. The particles' behaviour, influenced by their size and buoyant velocities, was tracked over a 8-hour period. The far-field simulation

illustrated that larger particles resurfaced faster, while smaller ones remained entrapped for a longer duration. Snapshots of the droplet cloud at different time intervals depicted the spatial distribution and size-dependent ascent of particles. After totally $\sim$11 hours, all the oil had resurfaced, being transported southeastward.

Chapter 5

Conclusions and perspectives

The threat of oil spills to the marine environment is a substantial and ongoing concern. This study focuses specifically on subsurface oil spill incidents, such as damaged pipelines, drilling well blowouts, or sinking oil tankers. The primary motivation for this work is to comprehensively understand the phenomena and predict the behaviour of such oil spills. After a subsurface accident occurs, essential scientific questions arise, ranging from predicting the location, timing, and likelihood of resurfacing to understanding the interaction with the submerged bathymetry.

The aim of this study was to develop and deploy a subsurface oil model UWORM, intending to integrate it with the existing Medslik-II surface model. This integration seeks to advance our comprehension and predictive abilities regarding oil spills by considering interactions both beneath and on the surface. In the realm of surface modelling, Medslik-II, an open-source model developed by a consortium including the University of Bologna and CMCC, is routinely employed in real oil spill incidents. Medslik-II employs advection-diffusion principles to simulate the physical transport of oil parcels and incorporates weathering processes for the chemical transformation of the oil slick. It uses a double-step algorithm to simulate

processes on two different time scales, combining Lagrangian particle tracking with Eulerian modelling. The final oil concentration at sea is computed from information about the oil slick and particles.

Upon delving deeper into subsurface modelling and processes, we encountered a complex field with various research challenges needing resolution. Furthermore, the Medslik-II model, being Fortran-based, is outdated and lacks comprehensive documentation. Therefore, we opted to focus on fully implementing a standalone subsurface code that could operate independently and easily integrate with any surface model for oil spills.

To address questions about the timing, location, and emergence of oil spilled at depth, we separated the subsurface evolution problem into near and far-field phases. These two phases, supported by both theoretical and empirical evidence, represent the current state-of-the-art understanding.

In both the near and far-field, buoyancy plays a predominant role in governing the motion. Buoyancy-driven oil ascends in a turbulent flow, leading to mixing and entrainment of seawater. In a stratified ocean, as buoyancy gradually becomes neutral, the plume decelerates until reaching a maximum level of rise. At this point, plume coherence diminishes, resulting in the separation of oil and water. Buoyancy reasserts itself as a driving force in far-field dynamics, influencing the velocity of oil particles proportionate to their size. Our study is structured around this two-phase classification. Firstly, we presented a near-field plume model, outlining the methodological approach and validation under varied conditions. Secondly, we explored far-field Lagrangian tracking of oil particles. The coupling of these two phases allows a complete simulation spanning from the ocean floor to the surface, which we demonstrate in a hypothetical oil spill scenario in the Southern Adriatic Sea.

In Chapter 3, for the near-field module, we designed and implemented a new

Python-based integral plume model, where the oil ascends as a coherent structure composed of independently evolving Lagrangian elements. This approach predicts seawater entrainment into the plume by combining boundary layer theory and turbulent mixing parametrisation. The model is grounded in two mechanisms: shear inflow and advection inflow driven by currents. Both instantaneous and continuous releases are options, with the latter considering variations in ocean currents under steady-state conditions.

The near-field model takes as input both release conditions (initial volume flux, oil density, and temperature) and ambient ocean conditions (depth-profile of velocity currents, salinity, temperature, and density). It yields outputs such as plume trajectory and geometry, thermodynamics, and pollutant dilution over time. Fifteen governing equations, focusing on fundamental processes and excluding detrainment and a gaseous component, were applied for each plume element. We introduced a straightforward equation for the time-varying mixture of oil and water density. To solve these equations, we implemented a Python module using a fourth-order Runge-Kutta scheme.

Our simulations underwent validation through laboratory experiments conducted in both stratified and unstratified environments, as well as a real-scale experiment in the North Sea in 1995, known as NOFO, specifically designed to study subsurface spills. The near-field validation underscores two crucial findings. Firstly, accurate calibration of the entraining flux is essential, given its significant impact on overall plume buoyancy. The second factor is the choice of the terminal level criterion. Our analysis of the vertical component reveals that a neutral buoyancy depth, where the plume density equals the ambient ocean density, is followed by a deceleration. The literature lacks a universally accepted definition of the terminal level. In our approach, we designated the terminal level as the depth where the plume's vertical velocity falls below a specific threshold, determined by numerical stability.

Future work on this module should address the gas component, including deep-

water deviations from ideal gas behaviour described in Chapter 2.

In moving from the near to the far field (Chapter 4), we decided against including an intermediate lateral buoyant spreading phase due to the typically reduced time and spatial scales involved. So the end of the near-field phase sets the initial conditions for the far-field, which was implemented via OceanParcels, were a 'buoyant behaviour' was added to the transport problem. The plume element at the terminal level is broken down into a sustained number of oil particles, each assigned an initial position uniformly across the final plume area. These particles undergo a three-dimensional ocean currents advection and turbulent sub-grid diffusion. Vertically, the movement of the particles is determined by their buoyancy. The droplet scale (ranging from μm to mm) suggests involving a buoyancy and a drag forces, resulting in a size-dependent equilibrium state. We assumed a static log-normal distribution for droplet size. Considerations for alternative choices include dynamic distributions that account for continuous coalescence and separation processes driven by turbulence. Future work should also incorporate the effects of chemical dispersants or biodegradation, which reduce droplet size.

In conducting a comprehensive near-far field simulation in the Southern Adriatic Sea, we successfully addressed the core questions of our investigation. The timing of oil resurfacing depends on the plume's rising time to the maximum level (approximately 3 hours) and subsequent droplet travel time, varying significantly with size (from 10 minutes for larger particles to 8 hours for smaller ones). Accurate predictions of resurfacing locations require precise information about the ocean state beyond the release position. Ocean currents play a crucial role in advecting the plume, entraining water, and subsequently advecting particles. Additionally, obtaining accurate knowledge of temperature and salinity, contributing to stratification, is essential. The uncertainty surrounding the droplet number is another aspect to be further studied, as it should reflect the discharged oil amount at the release point, in both instantaneous and continuous discharge scenarios. A statistical

analysis of the particles resurfacing phenomenon is to be conducted.

The subsurface model UWORM, which includes a new code for the near-field and incorporates modified OceanParcels for the far-field (with the addition of particle buoyancy), is now ready to be integrated with any surface model for oil transport. The final state of the UWORM subsurface model can serve as the initial state for a surface model. Depending on the occurrence of subsurface intrusion, this integration will utilise either the near-field stage (utilising information such as the final plume radius, depth, displacement relative to the source, and oil concentration) or the far-field stage (providing information on the total oil amount and positions of oil particles constituting the slick). The integration with a surface model is not addressed in this study and will be a focus of future work, particularly in coupling with Medslik-II.

Appendices

A.1 Forced entrainment computation

In this section we present the analytical expression of the "forced" entrainment, representing the transport of seawater into the plume. In calculating this inflow, the authors of (Lee and Cheung, 1990) considered that plume elements (cylinders) deformations (stretching in the vertical, bending and enlarging). In the local coordinates system (x', y', z'), we consider the velocity in spherical coordinates $(|\vec{v}|, v_\phi, v_\theta)$, where $|\vec{v}| = \sqrt{u^2 + v^2 + w^2}$, $v_\theta = \arctan(v/u)$ $v_\phi = \arcsin(w/u_v)$. As stated in Eq. (3.7), the volume flux of $\vec{v}_a = (u_a, v_a, 0)$ into the infinitesimal surface area dA of the cylinder is:

$$dQ_f = -\vec{v}_a \cdot d\vec{A} = -(\hat{i} \cdot u_a d\vec{A} + \hat{j} \cdot v_a d\vec{A}) \tag{5.1}$$

The total volume flux Q_f is obtained by integration on the total windward surface A_a:

$$Q_f = \int_{A_a} -\vec{v}_a \cdot d\vec{A} = \int_{A_a} -(\hat{i} \cdot u_a d\vec{A} + \hat{j} \cdot v_a d\vec{A}) = Q_{fx} + Q_{fy} \tag{5.2}$$

The first objective is the calculation of the area A_a, the portion of the lateral surface of the cylinder perpendicular to the ambient flow $\vec{v}_a$. Given the parallel and perpendicular projections of the ambient velocity components on the plume velocity

$$u_{a\parallel} = u_a \cos v_\theta \cos v_\phi, u_{a\perp} = u_a^2(1 - \cos {v_\phi}^2 \cos {v_\theta}^2)$$

$$v_{a\parallel} = v_a \sin v_\theta \cos v_\phi, v_{a\perp} = u_a^2(1 - \sin {v_\phi}^2 \cos {v_\theta}^2)$$

1832 we will herein demonstrate the result

$$\begin{cases} Q_{fx} &= \pi b \Delta b \, u_{a\parallel} + 2bh \, u_{a\perp} + \pi \frac{b^2}{2} \, \Delta u_{a\parallel} \\ Q_{fy} &= \pi b \Delta b \, v_{a\parallel} + 2bh \, v_{a\perp} + \pi \frac{b^2}{2} \, \Delta v_{a\parallel} \end{cases} \tag{5.3}$$

1833 Referring to Figure 5.1, in a time Δt, the cylinder is stretched of S, curved on
1834 finite difference orientations Δv_ϕ and Δv_θ, and enlarged of Δb. Defining a new
1835 orthonormal local coordinate system $(\hat{l}, \hat{m}, \hat{n})$, $\hat{l}$ is along the cylinder velocity, $\hat{m}$
1836 and $\hat{n}$ define the plane perpendicular to $\hat{l}$:

$$\begin{cases} \hat{l} &= \cos v_\phi \cos v_\theta \hat{i} + \cos v_\phi \sin v_\theta \hat{j} + \sin v_\phi \hat{k} \\ \hat{n} = -R\frac{d\hat{l}}{ds} &= R\big[\big(\cos v_\phi \sin v_\theta \dot{v_\theta} + \sin v_\phi \cos v_\theta \dot{v_\phi}\big)\hat{i} + \\ &+\big(\sin v_\phi \sin v_\theta \dot{v_\phi} + \cos v_\phi \cos v_\theta \dot{v_\theta}\big)\hat{j} + \\ &-\big(\cos v_\phi \dot{v_\phi}\big)\hat{k} \\ \hat{m} = \hat{n} \times \hat{l} &= R\big[\big(\sin v_\theta \dot{v_\phi} - \sin v_\phi \cos v_\phi \cos v_\theta \dot{v_\theta}\big)\hat{i} + \\ &-\big(\cos v_\theta \dot{v_\phi} + \cos v_\phi \sin v_\phi \sin v_\theta \dot{v_\theta}\big)\hat{j} + \\ &+\big(\cos^2 v_\phi \dot{v_\theta}\big)\hat{k} \end{cases} \tag{5.4}$$

1837 From Figure 5.1, the infinitesimal surface area is:

$$|dA| = (\Delta b^2 + S'^2)^{1/2} b d\psi$$

1838 The corresponding vector area can be written in the system $(\hat{l}, \hat{m}, \hat{n})$:

$$\vec{dA} = \Big[-\frac{\Delta b}{S'}\hat{l} + \cos\psi \hat{m} + \sin\psi \hat{n}\Big] S' b d\psi$$

1839 In Fig. 5.1 the stretching S defines the curvature radius $R = (\dot{v_\phi}^2 + \cos {v_\phi}^2 \dot{v_\theta}^2)^{-1/2}$,
1840 and S' defines the curvature radius $R' = R + x$, where $x = b \sin\psi$. We substitute
1841 the expressions for $S' = S(R + x)/R$ and $x = b \sin\psi$

$$d\vec{A} = \Big[-\Delta b\hat{l} + \cos\psi S\frac{(b\sin\psi + R)}{R}\hat{m} + \sin\psi S\frac{(b\sin\psi + R)}{R}\hat{n}\Big] b d\psi$$

The angle ψ serves for the area integration and is defined on the $\hat{m}-\hat{n}$ plane ($\psi = 0$ corresponds to $\hat{m}$-direction). The integration in ψ is done on the windward side of the lateral surface through β, which sets the projection of the ambient current $\vec{v}_a$ on the $\hat{m}-\hat{n}$ plane. The windward surface is then defined for ψ in $[\pi/2-\beta, 3/2\pi-\beta]$.

The Q_{fx} contribution to the total flux is evaluated by inserting $d\vec{A}$ and substituting the cartesian components of $(\hat{l}, \hat{m}, \hat{n})$. After the area integration we find the following

$$\begin{cases} Q_{fx} & = u_a b\big\{\pi\Delta b\cos v_\theta\cos v_\phi + \\ & +\Delta S\big[-2R\cos\beta\big(\sin v_\theta \dot{v_\phi} - \sin v_\phi\cos v_\phi\cos v_\theta \dot{v_\theta}\big) + \\ & +(b\tfrac{\pi}{2} + 2R\sin\beta)\big(\cos v_\phi\sin v_\theta\dot{v_\theta} + \cos v_\theta\sin v_\phi\dot{v_\phi}\big)\big]\big\} \end{cases} \tag{5.5}$$

we substitute the expression of R and β, finally obtaining:

$$Q_{fx} = u_a\left[\pi b\Delta b\cos v_\phi\cos v_\theta + 2b\Delta S\sqrt{1-\cos^2 v_\theta cos^2 v_\phi} + \frac{\pi b^2}{2}\Delta(\cos v_\phi\cos v_\theta)\right] \tag{5.6}$$

In a similar manner Q_{fy} is found, proving Equation 5.3.

$$Q_{fy} = v_a\left[\pi b\Delta b\cos v_\phi\sin v_\theta + 2b\Delta S\sqrt{1-\sin^2 v_\theta cos^2 v_\phi} + \frac{\pi b^2}{2}\Delta(\cos v_\phi\sin v_\theta)\right] \tag{5.7}$$

Eqs. (5.6) and (5.7) give the complete forced flux formulation in a 2D ambient flow. This computation is performed at each time step for every cylinder and it is combined with the shear volume flux to obtain the total entrainment.

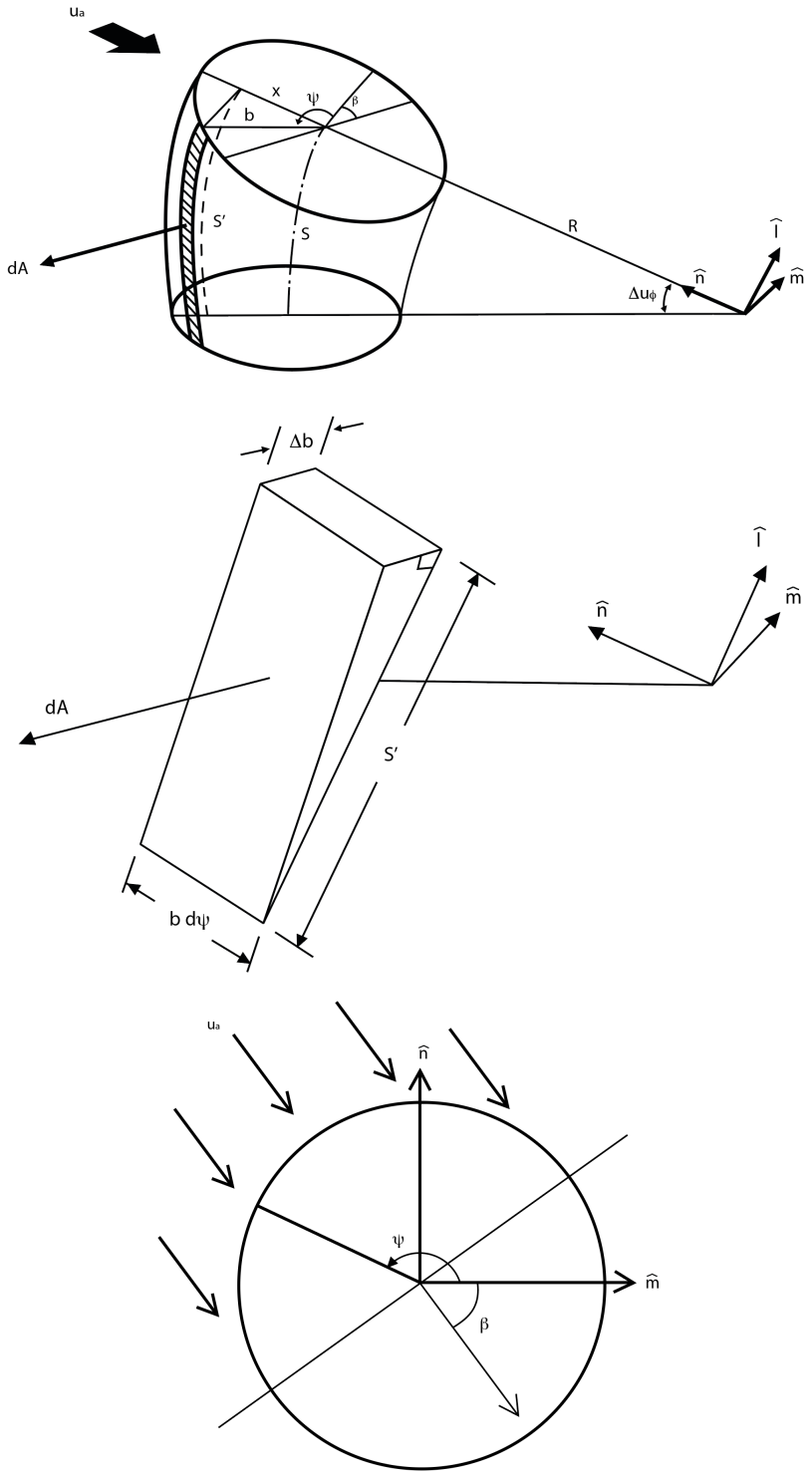

Figure 5.1: Cylinder infinitesimal area dA is calculated from potential stretching S, enlarging of radius Δb and bending Δv_ϕ. The ambient current direction is set by u_a.

A.2 Plume model numerical discretization

In this section we present the numerical discretization of the near-field component of UWORM. For clarity, we show a forward Euler scheme, though the code is implemented with a Runge-Kutta IV scheme.

In an instantaneous release, one cylinder is simulated. In a continuous release, a series of cylinders are modelled and each of them undergoes the following, with time-varying ambient ocean conditions.

The initial release conditions are:

$$b^0,\ \vec{v}^0 = (u^0, v^0, w^0) = (|\vec{v}|^0, v_\phi^0, v_\theta^0),\ (x^0, y^0, z^0),\ c^0 = 1,\ T^0,\ S^0$$

The oil density $\rho_{oil}(T^0)$ is calculated from Eq. 3.1g and the entrained ambient water density is $\rho_w^0(T^0, S^0)$ from Eq. 3.1h, so that ρ^0 is the initial cylinder density

$$\rho^0 = \frac{\rho_w^0 \rho_{oil}^0}{c^0 \rho_w^0 + (1 - c^0)\rho_{oil}^0} = \rho_{oil}^0$$

and the ambient time-varying conditions are calculated at the cylinder depth:

$$\rho_a^t(T_a^t, S_a^t),\ \ c_a^t,\ \ \vec{v}_a^t = (u_a^t, v_a^t, 0)$$

The simulation time-step is $\Delta t = b^0/|\vec{v}^0|$. The initial thickness is defined as $h^0 = |\vec{v}^0|\Delta t$ and the initial mass is $m^0 = \pi(b^0)^2 h^0 \rho^0$.

At each step, the cylinder properties are updated: position, mass, momentum, oil mass fraction, temperature and salinity. The new position is

$$\begin{cases} x^{t+\Delta t} &= x^t + u^t \Delta t \\ y^{t+\Delta t} &= y^t + v^t \Delta t \\ z^{t+\Delta t} &= z^t + w^t \Delta t \end{cases} \tag{5.8}$$

The mass is updated

$$m^{t+\Delta t} = m^t + \rho_a^t Q_e^t \Delta t \tag{5.9}$$

and the entrained volume flux is $Q_e^t = \max(Q_s^t, Q_f^t)$, where the shear component is

$$Q_s^t = 2\pi b^t h^t \alpha^t \ \ ||\vec{v}^t| - v_{a\|}^t|$$

where

$$\begin{cases} v_{a\|}^t & = \vec{v}^t \cdot \vec{v}_a^t / |\vec{v}^t| \\ \alpha^t & = (a1 + a2 \sin v_\phi^t F12^t)/(1 + a3\ v_{a\|}^t / ||\vec{v}^t| - v_{a\|}^t|) \\ F12^t & = 9.81 \frac{\rho_a^t - \rho^t}{\rho_a^0} (b^t / ||\vec{v}^t| - v_{a\|}^t|)^2 \end{cases} \tag{5.10}$$

The forced component is calculated:

$$\begin{cases} Q_f^t & = u_a h^t b^t \big[2\sqrt{\sin {v_\phi^t}^2 + \sin {v_\theta^t}^2 + (\sin v_\theta^t \sin v_\phi^t)^2} \\ & + \pi \frac{\Delta b^t}{\Delta s^t} \cos v_\theta^t \cos v_\phi^t \\ & + \frac{\pi}{2} b^t \frac{\cos v_\theta^t \cos v_\phi^t - \cos v_\theta^{t-\Delta t} \cos v_\phi^{t-\Delta t}}{\Delta s^t} \end{cases} \tag{5.11}$$

where $\Delta s = [(x^t - x^{t-\Delta t})^2 + (y^t - y^{t-\Delta t})^2 + (z^t - z^{t-\Delta t})^2]^{1/2}$ and $\Delta b = b^t - b^{t-\Delta t}$.

The momentum equation is calculated by knowledge of the mass, and it is discretized as:

$$\frac{\vec{v}^{t+\Delta t} m^{t+\Delta t} - \vec{v}^t m^t}{\Delta t} = \vec{v}_a \frac{m^{t+\Delta t} - m^t}{\Delta t} + m^t \frac{\rho_a^t - \rho^t}{\rho_a^0} g \hat{k} \tag{5.12a}$$

Since $m^{t+\Delta t} - m^t = \rho_a Q_e \Delta t$, it is

$$m^{t+\Delta t} \vec{v}^{t+\Delta t} = m^t \vec{v}^t + \vec{v}_a^t \rho_a^t Q_e^t \Delta t + m^t \frac{\rho_a^t - \rho^t}{\rho_a^0} g \Delta t \hat{k} \tag{5.13}$$

The discretized momentum conservation equations for each component are

$$\begin{cases} u^{t+\Delta t} m^{t+\Delta t} & = u^t m^t + u_a^t \rho_a^t Q_e^t \Delta t \\ v^{t+\Delta t} m^{t+\Delta t} & = v^t m^t + v_a^t \rho_a^t Q_e^t \Delta t \\ w^{t+\Delta t} m^{t+\Delta t} & = w^t m^t + w_a^t \rho_a^t Q_e^t \Delta t + m^t \frac{\rho_a^t - \rho^t}{\rho_a^0} g \Delta t \end{cases} \tag{5.14}$$

Then update the mass fraction of oil, the cylinder temperature and the salinity

$$\begin{cases} c^{t+\Delta t}m^{t+\Delta t} &= c^t m^t + c_a^t \rho_a^t Q_e^t \Delta t \\ T^{t+\Delta t}m^{t+\Delta t} &= T^t m^t + T_a^t \rho_a^t Q_e^t \Delta t \\ S^{t+\Delta t}m^{t+\Delta t} &= S^t m^t + S_a^t \rho_a^t Q_e^t \Delta t \end{cases} \tag{5.15}$$

and evaluate the new density through the state equation

$$\rho^{t+\Delta t} = \frac{\rho_{oil}(T^{t+\Delta t})\rho_w(T^{t+\Delta t}, S^{t+\Delta t})}{\rho_{oil}(T^{t+\Delta t})(1-c^{t+\Delta t}) + \rho_w(T^{t+\Delta t}, S^{t+\Delta t})c^{t+\Delta t}} \tag{5.16}$$

Finally calculate the new geometrical parameters and the orientation:

$$\begin{cases} h^{t+\Delta t} &= (|\vec{v}|^{t+\Delta t}/|\vec{v}|^t)h^t \\ b^{t+\Delta t} &= \sqrt{\frac{m^{t+\Delta t}}{\rho_m^{t+\Delta t}\pi h^{t+\Delta t}}} \end{cases} \tag{5.17}$$

$$\begin{cases} v_\theta^{t+\Delta t} &= \arctan(v^{t+\Delta t}/u^{t+\Delta t}) \\ v_\phi^{t+\Delta t} &= \arccos(w^{t+\Delta t}/|\vec{v}|^{t+\Delta t}) \end{cases} \tag{5.18}$$

We implemented a Python code with a Runge-Kutta IV scheme. In Figure 5.2 the Euler/RK-IV scheme comparison in the laboratory experiment **1b** described in Section 3.5.1, showing position (Figure 5.2**a**) and oil mass fraction (Figure 5.2**b**).

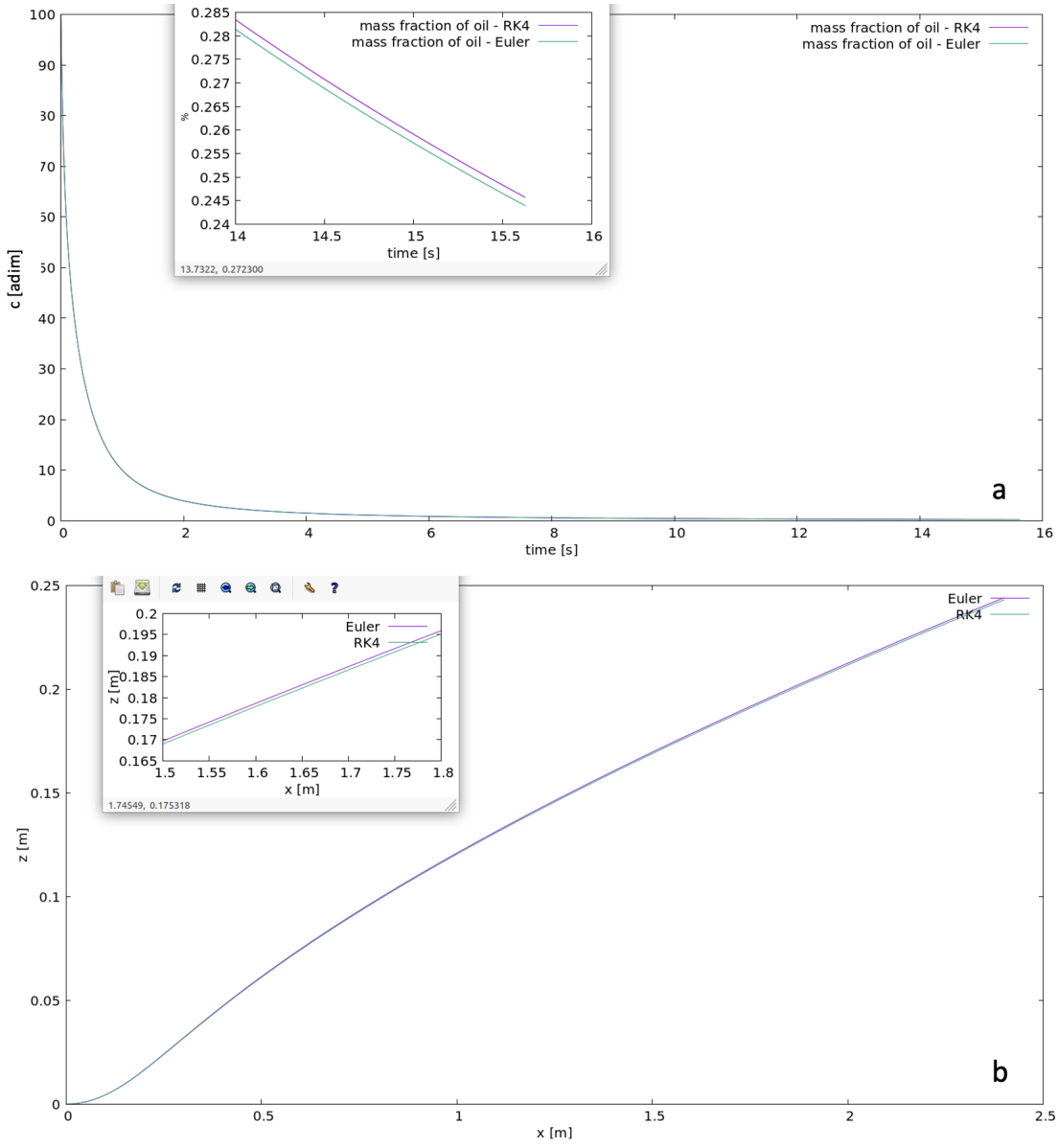

Figure 5.2: **a**, oil mass fraction c; **b**, vertical position z. Comparison between the Euler (purple) and RK-IV (green) schemes. The relative error is $\sim 0.5\%$.

A.3 Ocean vertical velocity computation

In the far-field, oil particles are advected with 3D ocean components (u_a, v_a, w_a). The vertical velocity w_a is computed from knowledge of the horizontal components, usually given by OGCM models. The hypothesis of continuity is a powerful means

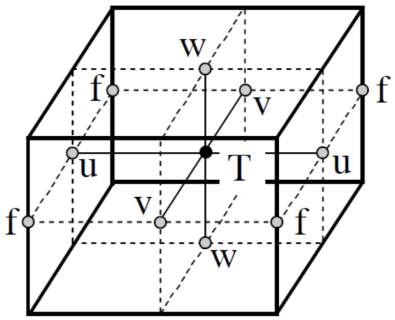

Figure 5.3: Arakawa-C grid used in NEMO model: T indicates scalar points where temperature, salinity, horizontal divergence are defined, (u,v,w) indicates vector points, and f indicates vorticity points. Adapted from NEMO v4.3 manual (Gurvan et al., 2022).

to calculate the vertical velocity, which can be integrated from the ocean floor to the surface with proper boundary conditions:

$$\frac{\partial \rho}{\partial t} + \nabla \cdot (\rho \vec{v_a}) = 0$$

The continuity equation becomes, under the incompressible assumption $\rho_a(x, y, z, t) =$ constant :

$$\nabla \cdot \vec{v_a} = 0 \tag{5.19}$$

Which equals to the equation for the vertical velocity w_a:

$$\frac{\partial w_a}{\partial z} = -\nabla_h \cdot (u_a, v_a) \tag{5.20}$$

with bottom boundary condition $w_a(z = -H) = 0$.

In a general curvilinear coordinate system, we define the scale factors $e1, e2, e3$ for the infinitesimal increments $(dx, dy, dz) = (e_1 dx_1, e_2 dx_2, e_3 dx_3)$.

CMEMS ocean currents are provided through the NEMO model, with staggered Arakawa C-type grid (Mesinger and Arakawa, 1976) which set scalar quantities at the center of each grid volume (T points), while vectorial fields are defined at the edges (u, v, w, f points), as illustrated in Figure 5.3.

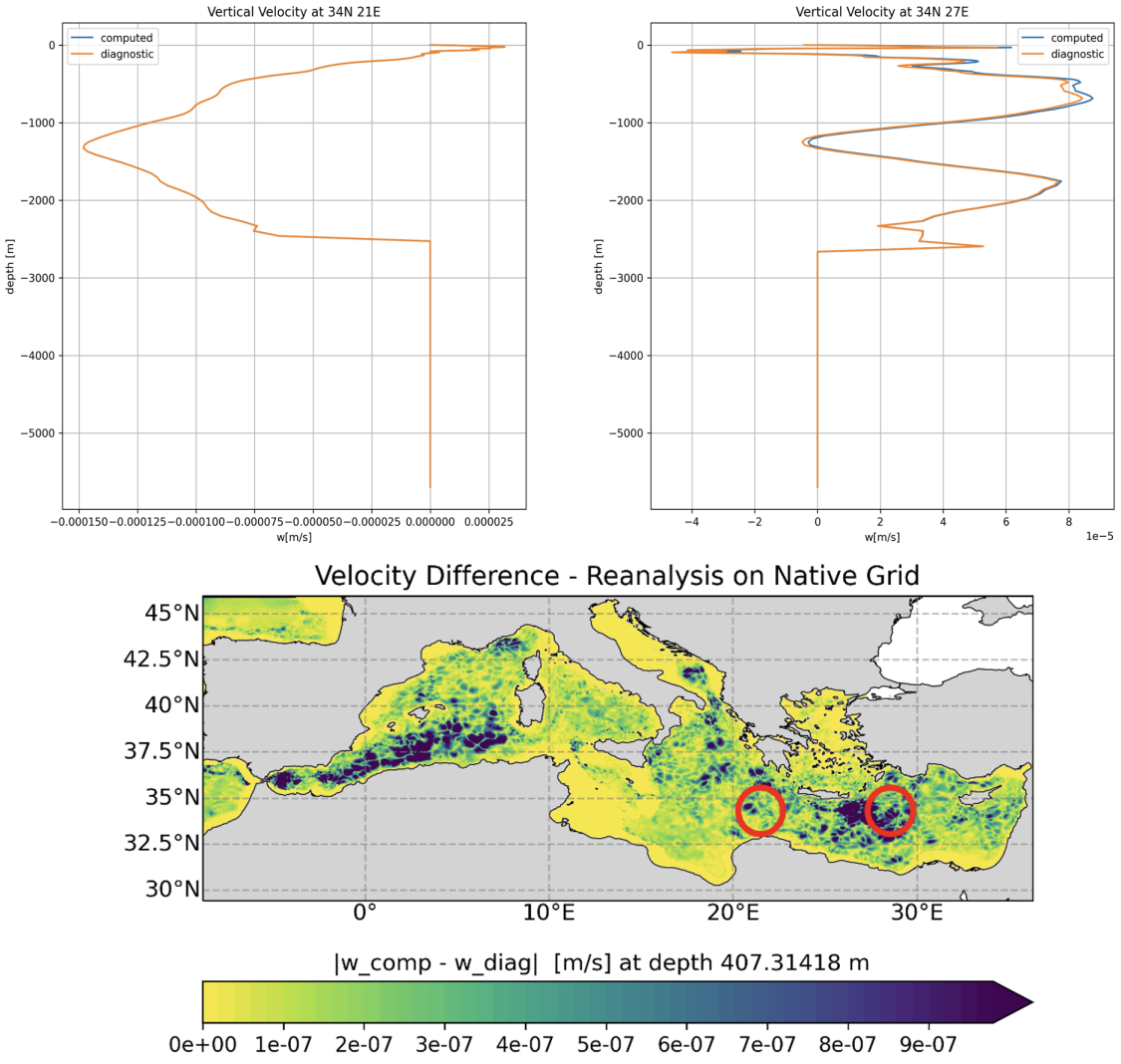

Figure 5.4: Computed vertical velocity depth profiles, for two different locations in the Mediterranean Sea. In orange, the one given by NEMO, in blue, the one computed through the algorithm described. Maximum discrepancy is $\sim 10^{-6}$ m/s.

In this representation, each variable is assigned with its scale factors and the

divergence in Eq. 5.19 is expressed as

$$\nabla \cdot \vec{v}_a = \frac{1}{e_{1t}e_{2t}e_{3t}}[\frac{\partial}{\partial x_1}u_a e_{2u}e_{3u} + \frac{\partial}{\partial x_2}v_a e_{1v}e_{3v} + \frac{\partial}{\partial x_3}w_a e_{1t}e_{2t}] = 0$$

Assuming that e_1 and e_2 do not depend on z, the vertical component of ocean velocity in Eq. 5.20 is calculated as

$$\begin{cases} \frac{\partial w_a}{\partial x_3} & = -e_{3t}\left[\frac{1}{e_{1t}e_{2t}e_{3t}}(\frac{\partial}{\partial x_1}u_a e_{2u}e_{3u} + \frac{\partial}{\partial x_2}v_a e_{1v}e_{3v})\right] \\ w_a(z=-H) & = 0 \end{cases} \tag{5.21}$$

We show in Figure 5.4 the computed vertical component by algorithm exposed above with the one from NEMO, for available data.

Bibliography

A. AI-Rabeh, R. Lardner, and M. Hossain. Oilpol-an oil fate and transport model for the arabian gulf. Technical report, King Abdulaziz University, 1995.

P. J. Akar and G. H. Jirka. Buoyant spreading processes in pollutant transport and mixing part 1: Lateral spreading with ambient current advection. *Journal of Hydraulic Research*, 32(6):815–831, 1994. doi: 10.1080/00221689409498692. URL https://doi.org/10.1080/00221689409498692.

A. Al-Rabeh, H. Cekirge, and N. Gunay. A stochastic simulation model of oil spill fate and transport. *Applied Mathematical Modelling*, 13(6):322–329, 1989. ISSN 0307-904X. doi: https://doi.org/10.1016/0307-904X(89)90134-0. URL https://www.sciencedirect.com/science/article/pii/0307904X89901340.

K. Aravamudan, P. Raj, J. Ostlund, E. Newman, and W. Tucker. Break-up of oil on rough seas-simplified models and step-by-step calculations. Technical report, Little (Arthur D.), Inc., Cambridge, MA (USA), 1982.

A. Artegiani, D. Bregant, E. Paschini, N. Pinardi, F. Raicich, and A. Russo. The adriatic sea general circulation. part ii: Baroclinic circulation structure. *Journal of Physical Oceanography*, 27:1515–1532, 08 1997. doi: 10.1175/1520-0485(1997)027<1515:TASGCP>2.0.CO;2.

U. C. Bandara and P. D. Yapa. Bubble sizes, breakup, and coalescence in deepwater

gas/oil plumes. *Journal of Hydraulic Engineering*, 137:729–738, 7 2011. ISSN 0733-9429. doi: 10.1061/(asce)hy.1943-7900.0000380.

F. T. Barreto, D. O. Dammann, L. F. Tessarolo, J. Skancke, I. Keghouche, V. Innocentini, N. Winther-Kaland, and L. Marton. Comparison of the coupled model for oil spill prediction (cmop) and the oil spill contingency and response model (oscar) during the deepspill field experiment. *Ocean and Coastal Management*, 204:105552, 2021. ISSN 0964-5691. doi: https://doi.org/10.1016/j.ocecoaman.2021.105552. URL https://www.sciencedirect.com/science/article/pii/S0964569121000375.

K. Bello and K. Idigbe. Development of a new drag coefficient model for oil and gas multiphase fluid systems. *Nigerian Journal of Technology*, 34:280, 3 2015. ISSN 0331-8443. doi: 10.4314/njt.v34i2.10.

J. Bennett and A. Clites. Accuracy of trajectory calculation in a finite-difference circulation model. *Journal of Computational Physics*, 68:272–282, 02 1987. doi: 10.1016/0021-9991(87)90058-1.

A. Berry, T. Dabrowski, and K. Lyons. The oil spill model oiltrans and its application to the celtic sea. *Marine Pollution Bulletin*, 64:2489–2501, 11 2012. ISSN 0025326X. doi: 10.1016/j.marpolbul.2012.07.036.

S. Berti, F. A. D. Santos, G. Lacorata, and A. Vulpiani. Lagrangian drifter dispersion in the southwestern atlantic ocean. *Journal of Physical Oceanography*, 41:1659–1672, 9 2011. ISSN 00223670. doi: 10.1175/2011JPO4541.1.

L. J. Bloomfield and R. Kerr. A theoretical model of a turbulent fountain. *Journal of Fluid Mechanics*, 424:197 – 216, 12 2000. doi: 10.1017/S0022112000001907.

M. A. Bobra and P. T. Chung. A catalogue of oil properties. Technical report, Consultchem, Ottawa, Canada, 1986.

P. J. Brandvik, O. Johansen, F. Leirvik, U. Farooq, and P. Daling. Droplet breakup in subsurface oil releases - part 1: Experimental study of droplet breakup and effectiveness of dispersant injection. *Marine pollution bulletin*, 73, 06 2013. doi: 10.1016/j.marpolbul.2013.05.020.

R. Camilli, C. M. Reddy, D. R. Yoerger, B. A. S. Van Mooy, M. V. Jakuba, J. C. Kinsey, C. P. McIntyre, S. P. Sylva, and J. V. Maloney. Tracking hydrocarbon plume transport and biodegradation at deepwater horizon. *Science*, 330(6001): 201–204, Oct. 2010. ISSN 1095-9203. doi: 10.1126/science.1195223. URL http://dx.doi.org/10.1126/science.1195223.

R. Camilli, D. D. Iorio, A. Bowen, C. M. Reddy, A. H. Techet, D. R. Yoerger, L. L. Whitcomb, J. S. Seewald, S. P. Sylva, and J. Fenwick. Acoustic measurement of the deepwater horizon macondo well flow rate. *Proceedings of the National Academy of Sciences of the United States of America*, 109:20235–20239, 12 2012. ISSN 00278424. doi: 10.1073/PNAS.1100385108/-/DCSUPPLEMENTAL/PNAS.1100385108_SI.PDF.

F. Chen and P. Yapa. Estimating the oil droplet size distributions in deepwater oil spills. *Journal of Hydraulic Engineering-asce - J HYDRAUL ENG-ASCE*, 133, 02 2007. doi: 10.1061/(ASCE)0733-9429(2007)133:2(197).

H. Chiri, A. J. Abascal, and S. Castanedo. Deep oil spill hazard assessment based on spatio-temporal met-ocean patterns. *Marine pollution bulletin*, 154:111123, 2020.

G. Coppini, E. Clementi, G. Cossarini, S. Salon, G. Korres, M. Ravdas, R. Lecci, J. Pistoia, A. Goglio, M. Drudi, A. Grandi, A. Aydoğdu, R. Escudier, A. Cipollone, V. Lyubartsev, A. Mariani, S. Creti, F. Palermo, M. Scuro, and A. Zacharioudaki. The mediterranean forecasting system. part i: evolution and performance. *EGUsphere*, 01 2023. doi: 10.5194/egusphere-2022-1337.

1960 G. T. Csanady. *Turbulent Diffusion in the Environment*. Springer Science, Dordrecht,
1961 Boston, 1973.

1962 P. Daniel, F. Marty, P. Josse, C. Skandrani, and R. Benshila. Improvement of drift
1963 calculation in mothy operational oil spill prediction system. *International Oil Spill*
1964 *Conference Proceedings*, 2003, 04 2003. doi: 10.7901/2169-3358-2003-1-1067.

1965 L. K. Dasanayaka and P. D. Yapa. Role of plume dynamics phase in a deepwater
1966 oil and gas release model. *Journal of Hydro-Environment Research*, 2:243–253, 4
1967 2009. ISSN 15706443. doi: 10.1016/j.jher.2009.01.004.

1968 M. De Dominicis, N. Pinardi, G. Zodiatis, and R. Archetti. Medslik-ii, a lagrangian
1969 marine surface oil spill model for short-term forecasting-part 2: Numerical
1970 simulations and validations. *Geoscientific Model Development*, 6:1871–1888,
1971 2013a. ISSN 1991959X. doi: 10.5194/gmd-6-1871-2013.

1972 M. De Dominicis, N. Pinardi, G. Zodiatis, and R. Lardner. Medslik-ii, a lagrangian
1973 marine surface oil spill model for short-term forecasting-part 1: Theory. *Geo-*
1974 *scientific Model Development*, 6:1851–1869, 2013b. ISSN 1991959X. doi:
1975 10.5194/gmd-6-1851-2013.

1976 E. Delnoij, J. Kuipers, and W. van Swaaij. Dynamic simulation of gas-liquid
1977 two-phase flow: effect of column aspect ratio on the flow structure. *Chemical*
1978 *Engineering Science*, 52(21):3759–3772, 1997. ISSN 0009-2509. doi: https://
1979 doi.org/10.1016/S0009-2509(97)00222-4. URL https://www.sciencedirect.
1980 com/science/article/pii/S0009250997002224.

1981 G. A. Delvigne and C. E. Sweeney. Natural dispersion of oil. *Oil Chemical Pollution*,
1982 4(4):281–310, 1989.

1983 DGS-UNMIG. Elenco delle piattaforme marine e strutture assimilabili. Technical
1984 report, Ministero dello sviluppo economico, 2017.

A. L. Dissanayake, I. Jun, and S. A. Socolofsky. Numerical models to simulate oil and gas blowout plumes and associated chemical and physical processes of hydrocarbons. In *E-proceedings of the 36th IAHR world congress*, volume 28, 2015.

R. L. Doneker, G. H. Jirka, and T. O. Barnwell. Expert system for hydrodynamic mixing zone analysis of conventional and toxic submerged single port discharges (cormix1), 1990.

Z. Duan, B. He, and Y. Duan. Sphere drag and heat transfer. *Scientific Reports*, 5, 7 2015. ISSN 20452322. doi: 10.1038/srep12304.

A. J. Elliott. Shear diffusion and the spread of oil in the surface layers of the north sea. *Deutsche Hydrografische Zeitschrift*, 39(3), 1986.

Emodnet. Emodnet map viewer. URL https://emodnet.ec.europa.eu/geoviewer/.

EMSA. Maritime surveillance service for pollution prevention. Technical report, European Maritime Safety Agency, 2021. URL http://www.emsa.europa.eu/csn-menu/items.html?cid=122&id=4322.

D. S. Etkin and J. Welch. Oil spill intelligence report international oil spill database: trends in oil spill volumes and frequency. *Proceedings International Oil Spill Conference (Florida, USA)*, 1997.

L. N. Fan. *Turbulent buoyant jets into stratified or flowing ambient fluids*. PhD thesis, California Institute of Technology, 1967.

L. N. Fan and N. H. Brooks. Numerical solutions of turbulent buoyant jet problems. Technical report, California Institute of Technology, 1969.

T. Fannelop and K. Sjoen. *Hydrodynamics of Underwater Blowouts*. Ship Research

Institute of Norway, Marine Technology Centre, 1980. URL https://books.google.it/books?id=OVp8mwEACAAJ.

R. Fernandes, R. Neves, and C. Viegas. Integration of an oil and inert spill model in a framework for risk management of spills at sea – a case study for the atlantic area. 06 2013. doi: 10.13140/2.1.1740.3200.

H. B. Fischer, E. J. List, R. C. Y. Koh, J. Imberger, and N. H. Brooks. Chapter 3 - turbulent diffusion. In H. B. FISCHER, E. J. LIST, R. C. KOH, J. IMBERGER, and N. H. BROOKS, editors, *Mixing in Inland and Coastal Waters*, pages 55–79. Academic Press, San Diego, 1979. ISBN 978-0-08-051177-1. doi: https://doi.org/10.1016/B978-0-08-051177-1.50007-6. URL https://www.sciencedirect.com/science/article/pii/B9780080511771500076.

N. Fofonoff and R. Millard. Algorithms for computation of fundamental properties of seawater. *UNESCO Tech. Pap. Mar. Sci.*, 44, 01 1983.

D. P. French-McCay, M. L. Spaulding, D. Crowley, D. Mendelsohn, J. Fontenault, and M. Horn. Validation of oil trajectory and fate modeling of the deepwater horizon oil spill. *Frontiers in Marine Science*, 8, 2 2021. ISSN 22967745. doi: 10.3389/fmars.2021.618463.

W. E. Frick. Non-empirical closure of the plume equations. *Atmospheric Environment (1967)*, 18:653–662, 1984. ISSN 0004-6981. doi: https://doi.org/10.1016/0004-6981(84)90252-X. URL https://www.sciencedirect.com/science/article/pii/000469818490252X.

W. E. Frick, D. J. Baumgartner, and C. G. Fox. Improved prediction of bending plumes. *Journal of Hydraulic Research*, 32:935–950, 1994. doi: 10.1080/00221689409498699.

C. W. Gardiner et al. *Handbook of stochastic methods*, volume 3. springer Berlin, 1985.

GESAMP. Estimates of oil entering the marine environment from sea-based activities. Technical report, IMO/FAO/UNESCO-IOC/UNIDO/ WMO/IAEA/UN/UNEP Joint Group of Experts on the Scientific Aspects of Marine Environmental Protection, 2007.

U. Gräwe. Implementation of high-order particle-tracking schemes in a water column model. *Ocean Modelling*, 36(1):80–89, 2011. ISSN 1463-5003. doi: https://doi.org/10.1016/j.ocemod.2010.10.002. URL https://www.sciencedirect.com/science/article/pii/S1463500310001484.

M. Gurvan, R. Bourdallé-Badie, J. Chanut, E. Clementi, A. Coward, C. Ethé, D. Iovino, D. Lea, C. Lévy, T. Lovato, N. Martin, S. Masson, S. Mocavero, C. Rousset, D. Storkey, S. Müeller, G. Nurser, M. Bell, G. Samson, P. Mathiot, F. Mele, and A. Moulin. Nemo ocean engine, Mar. 2022. URL https://doi.org/10.5281/zenodo.6334656.

G. Haller. Lagrangian coherent structures from approximate velocity data. *Physics of Fluids*, 14:1851–1861, 2002. ISSN 10706631. doi: 10.1063/1.1477449.

P. Harris. *United Nations World Ocean Assessment*, chapter 21, Offshore hydrocarbon industries. Cambridge University Press, 2016.

J. O. Hinze. Fundamentals of the hydrodynamic mechanism of splitting in dispersion processes. *AIChE Journal*, 1(3):289–295, 1955. doi: https://doi.org/10.1002/aic.690010303. URL https://aiche.onlinelibrary.wiley.com/doi/abs/10.1002/aic.690010303.

D. P. Hoult, J. Fay, and L. J. Forney. A theory of plume rise compared with field

observations. *Journal of the Air Pollution Control Association*, 19:585–590, 1969. URL https://api.semanticscholar.org/CorpusID:121604560.

K. Huijer. Trends in oil spills from tanker ships 1995-2004. *28th Arctic and Marine Oilspill Program (AMOP) Technical Seminar*, 2005.

J. R. Hunter. The application of lagrangian particle-tracking techniques to modelling of dispersion in the sea. *Numerical Modelling: Applications to Marine Systems*, 145: 257–269, 1987. ISSN 0304-0208. doi: https://doi.org/10.1016/S0304-0208(08)70037-9.

IMO. International convention for the prevention of pollution from ships (marpol). protocol - annex i regulations for the prevention of pollution by oil. Technical report, International Maritime Organization, 1983. URL https://www.imo.org/en/OurWork/Environment/Pages/OilPollution-Default.aspx.

ITOPF. Oil tanker spill statistics. Technical report, International Tanker Owners Pollution Federation, 2022. URL https://www.itopf.org/.

A. Jernelöv. The threats from oil spills: Now, then, and in the future. *Ambio*, 39: 353–366, 9 2010. ISSN 00447447. doi: 10.1007/s13280-010-0085-5.

A. Jernelöv and O. Lindén. Ixtoc i: A case study of the world's largest oil spill. *Ambio*, 10:299–306, 1981.

G. Jirka. Integral model for turbulent buoyant jets in unbounded stratified flows. part i: Single round jet. *Environmental Fluid Mechanics*, 4:1–56, 9 2004. doi: 10.1023/A:1025583110842.

O. Johansen. The halten bank experiment. In *Proc. 7th Arctic Marine Oilspill Program, Technical Seminar. Edmonton, Alberta: Environmental Protection Service*, pages 17–36, 1984.

O. Johansen. Deepblow – a lagrangian plume model for deep water blowouts. *Spill Science and Technology Bulletin*, 6:103–111, 04 2000. doi: 10.1016/S1353-2561(00)00042-6.

Ø. Johansen, H. Rye, and C. Cooper. Deepspill—-field study of a simulated oil and gas blowout in deep water. *Spill Science and Technology Bulletin*, 8(5):433–443, 2003. ISSN 1353-2561. doi: https://doi.org/10.1016/S1353-2561(02)00123-8. URL https://www.sciencedirect.com/science/article/pii/S1353256102001238.

Ø. Johansen, P. J. Brandvik, and U. Farooq. Droplet breakup in subsea oil releases - part 2: Predictions of droplet size distributions with and without injection of chemical dispersants. *Marine Pollution Bulletin*, 73:327–335, 8 2013. ISSN 0025326X. doi: 10.1016/j.marpolbul.2013.04.012.

S. Kark, E. Brokovich, T. Mazor, and N. Levin. Emerging conservation challenges and prospects in an era of offshore hydrocarbon exploration and exploitation. *Conservation Biology*, 29(6):1573–1585, July 2015. ISSN 1523-1739. doi: 10.1111/cobi.12562. URL http://dx.doi.org/10.1111/cobi.12562.

J. D. Kessler, D. L. Valentine, M. C. Redmond, M. Du, E. W. Chan, S. D. Mendes, E. W. Quiroz, C. J. Villanueva, S. S. Shusta, L. M. Werra, S. A. Yvon-Lewis, and T. C. Weber. A persistent oxygen anomaly reveals the fate of spilled methane in the deep gulf of mexico. *Science*, 331:312–315, 1 2011. ISSN 00368075. doi: 10.1126/SCIENCE.1199697. URL www.sciencemag.org/cgi/content/full/science.1199375/DC1.

M. Lange and E. Van Sebille. Parcels v0.9: Prototyping a lagrangian ocean analysis framework for the petascale age. *Geoscientific Model Development*, 10:4175–4186, 11 2017. ISSN 19919603. doi: 10.5194/gmd-10-4175-2017.

R. Lardner, W. Lehr, R. Fraga, and M. Sarhan. A model of residual currents and pollutant transport in the arabian gulf. *Applied Mathematical Modelling*, 12(4):379–390, 1988. ISSN 0307-904X. doi: https://doi.org/10.1016/0307-904X(88)90067-4. URL https://www.sciencedirect.com/science/article/pii/0307904X88900674.

J. Lee, V. Cheung, and C. C. Lai. Jetlag2008 - an update. Technical report, Croucher Laboratory of Environmental Hydraulics, The University of Hong Kong, 2008.

J. H. Lee, V. Chu, and V. H. Chu. *Turbulent jets and plumes: A Lagrangian approach*, volume 1. Springer Science & Business Media, 2003.

J. H. W. Lee and V. Cheung. Generalized lagrangian model for buoyant jets in current. *Journal of Environmental Engineering*, 116:1085–1106, 10 1990. ISSN 0733-9372. doi: 10.1061/(ASCE)0733-9372(1990)116:6(1085).

J. H. W. Lee and V. Cheung. Mixing of buoyancy-dominated jets in a weak current. *Proceedings of the Institution of Civil Engineers*, 91(1):113–129, 1991. doi: 10.1680/iicep.1991.13585. URL https://doi.org/10.1680/iicep.1991.13585.

A. H. Lefebvre. *Atomization and sprays*. Bristol : Taylor and Francis, 1989.

B. Lehr, S. Bristol, and A. Possolo. Oil budget calculator, deepwater horizon. Technical report, The Federal Interagency Solutions Group, Oil Budget Calculator Science and Engineering Team, 2011.

W. Lehr, R. Jones, M. Evans, D. Simecek-Beatty, and R. Overstreet. Revisions of the adios oil spill model. *Environmental Modelling & Software*, 17:189–197, 1 2002. ISSN 1364-8152. doi: 10.1016/S1364-8152(01)00064-0.

P. Li, Q. Cai, W. Lin, B. Chen, and B. Zhang. Offshore oil spill response practices and emerging challenges. *Marine Pollution Bulletin*, 110(1):6–27, 2016. ISSN

0025-326X. doi: https://doi.org/10.1016/j.marpolbul.2016.06.020. URL https://www.sciencedirect.com/science/article/pii/S0025326X16304246.

Z. Li, M. Spaulding, D. F. McCay, D. Crowley, and J. R. Payne. Development of a unified oil droplet size distribution model with application to surface breaking waves and subsea blowout releases considering dispersant effects. *Marine Pollution Bulletin*, 114:247–257, 1 2017. ISSN 18793363. doi: 10.1016/j.marpolbul.2016.09.008.

S. Liubartseva, G. Coppini, R. Lecci, and E. Clementi. Tracking plastics in the mediterranean: 2d lagrangian model. *Marine Pollution Bulletin*, 129:151–162, 4 2018. ISSN 18793363. doi: 10.1016/j.marpolbul.2018.02.019.

P. Lujala, J. K. Rød, and N. Thieme. Fighting over oil: Introducing a new dataset. *Conflict Management and Peace Science*, 24:239–256, 2007.

D. Mackay and P. J. Leinonen. *Mathematical model of the behaviour of oil spills on water with natural and chemical dispersion*. Environment Protection Service, Fisheries and Environment Canada, 1977a. ISBN 0662012178.

D. Mackay and P. J. Leinonen. *Mathematical model of the behaviour of oil spills on water with natural and chemical dispersion*. Environment Protection Service, Fisheries and Environment Canada, 1977b. ISBN 0662012178.

M. Marta-Almeida, M. Ruiz-Villarreal, J. Pereira, P. Otero, M. Cirano, X. Zhang, and R. D. Hetland. Efficient tools for marine operational forecast and oil spill tracking. *Marine Pollution Bulletin*, 71:139–151, 2013. ISSN 0025-326X. doi: https://doi.org/10.1016/j.marpolbul.2013.03.022. URL https://www.sciencedirect.com/science/article/pii/S0025326X13001628.

S. M. Masutani and E. E. Adams. Experimental study of multi- phase plumes with

application to deep ocean oil spills. Technical report, Hawaii Natural Energy Institute, University of Hawaii, Honolulu, 2001.

T. J. Mcdougall. Bubble plumes in stratified environments. *Journal of Fluid Mechanics*, 85:655–672, 1978. doi: 10.1017/S0022112078000841.

M. McNutt, R. Camilli, T. Crone, G. Guthrie, P. Hsieh, T. Ryerson, O. Savas, and F. Shaffer. Review of flow rate estimates of the deepwater horizon oil spill. *Proceedings of the National Academy of Sciences of the United States of America*, 109, 12 2011. doi: 10.1073/pnas.1112139108.

F. Mesinger and A. Arakawa. Numerical methods used in atmospheric models. *Environmental Science, Physics*, 1976. URL https://api.semanticscholar.org/CorpusID:118508257.

J. Michel. Spills of nonfloating oil: evaluation of response technologies. In *International Oil Spill Conference*, volume 2008, pages 261–267. American Petroleum Institute, 2008.

J. H. Milgram. Mean flow in round bubble plumes. *Journal of Fluid Mechanics*, 133: 345–376, 1983. doi: 10.1017/S0022112083001950.

A. K. Mishra and G. S. Kumar. Weathering of oil spill: Modeling and analysis. *Aquatic Procedia*, 4:435–442, 2015. ISSN 2214241X. doi: 10.1016/j.aqpro.2015.02.058.

B. R. Morton, G. I. Taylor, and J. S. Turner. Turbulent gravitational convection from maintained and instantaneous sources. *Proceedings of the Royal Society of London. Series A. Mathematical and Physical Sciences*, 234:1–23, 1956. doi: 10.1098/rspa.1956.0011. URL https://royalsocietypublishing.org/doi/abs/10.1098/rspa.1956.0011.

NA. Oil in the sea: inputs, fates, and effects. Technical report, National Research Council and Division on Engineering and Physical Sciences and Commission on

Physical Sciences and Mathematics and Applications and Steering Committee for the Petroleum in the Marine Environment Update, 1985.

R. Nepstad, T. Nordam, I. H. Ellingsen, L. Eisenhauer, E. Litzler, and K. Kotzakoulakis. Impact of flow field resolution on produced water transport in lagrangian and eulerian models. *Marine Pollution Bulletin*, 182:113928, 2022. ISSN 0025-326X. doi: https://doi.org/10.1016/j.marpolbul.2022.113928. URL https://www.sciencedirect.com/science/article/pii/S0025326X22006105.

I. D. Nissanka and P. D. Yapa. Calculation of oil droplet size distribution in ocean oil spills: A review. *Marine Pollution Bulletin*, 135:723–734, 10 2018. ISSN 18793363. doi: 10.1016/j.marpolbul.2018.07.048.

NOAA. Gulf of mexico data atlas. Technical report, National Centers for Environmental Information, 2023. URL https://www.ncei.noaa.gov/maps/gulf-data-atlas/atlas.htm?plate=Gas.

T. Nordam, J. Skancke, R. Duran, and C. Barker. *Vertical mixing in oil spill modeling*, pages 97–143. 01 2021. ISBN 9780128193549. doi: 10.1016/B978-0-12-819354-9.00002-8.

E. W. North, E. Adams, Z. Schlag, C. R. Sherwood, R. He, K. H. Hyun, and S. A. Socolofsky. *Simulating Oil Droplet Dispersal From the Deepwater Horizon Spill With a Lagrangian Approach*, pages 217–226. American Geophysical Union (AGU), 2011. ISBN 9781118666753. doi: https://doi.org/10.1029/2011GM001102. URL https://agupubs.onlinelibrary.wiley.com/doi/abs/10.1029/2011GM001102.

E. W. North, E. E. Adams, A. E. Thessen, Z. Schlag, R. He, S. A. Socolofsky, S. M. Masutani, and S. D. Peckham. The influence of droplet size and biodegradation on the transport of subsurface oil droplets during the deepwater horizon spill:

A model sensitivity study. *Environmental Research Letters*, 10, 2 2015. ISSN 17489326. doi: 10.1088/1748-9326/10/2/024016.

NSTA. Offshore oil and gas activity. Technical report, North Sea Transition Authority, 2023. URL https://www.arcgis.com/apps/webappviewer/index.html?id=f4b1ea5802944a55aa4a9df0184205a5.

P. Nwilo and O. Badejo. Oil spill problems and management in the niger delta. *International Oil Spill Conference Proceedings*, 2005:567–570, 05 2005. doi: 10.7901/2169-3358-2005-1-567.

L. Palatella, F. Bignami, F. Falcini, G. Lacorata, A. S. Lanotte, and R. Santoleri. Lagrangian simulations and interannual variability of anchovy egg and larva dispersal in the sicily channel. *Journal of Geophysical Research: Oceans*, 119: 1306–1323, 2014. doi: https://doi.org/10.1002/2013JC009384. URL https://agupubs.onlinelibrary.wiley.com/doi/abs/10.1002/2013JC009384.

P. Palomar, J. Lara, I. Losada, and L. Tarrade. Numerical modeling of brine discharge: commercial models, medvsa online simulation tools and advanced computational fluid dynamics. *Desalination and Water Treatment*, 51(1–3):543–559, Aug. 2012. ISSN 1944-3986. doi: 10.1080/19443994.2012.714625. URL http://dx.doi.org/10.1080/19443994.2012.714625.

P. Panos and L. John. Investigations of round vertical turbulent buoyant jets, 1988.

S. Polinov, R. Bookman, and N. Levin. Spatial and temporal assessment of oil spills in the mediterranean sea. *Marine Pollution Bulletin*, 167, 6 2021. ISSN 18793363. doi: 10.1016/j.marpolbul.2021.112338.

L. Premathilake and T. Khangaonkar. Fvcom-plume – a three-dimensional lagrangian outfall plume dilution and transport model for dynamic tidal environ-

ments: Model development. *Marine Pollution Bulletin*, 149, 12 2019. ISSN 18793363. doi: 10.1016/j.marpolbul.2019.110554.

R. Proctor, R. A. Flather, and A. J. Elliott. Modelling tides and surface drift in the arabian gulf—application to the gulf oil spill. *Continental Shelf Research*, 14(5):531–545, 1994. ISSN 0278-4343. doi: https://doi.org/10.1016/0278-4343(94)90102-3. URL https://www.sciencedirect.com/science/article/pii/0278434394901023.

M. Reed, O. M. Aamo, and P. S. Daling. Quantitative analysis of alternate oil spill response strategies using oscar. *Spill Science and Technology Bulletin*, 2:67–74, 1995. ISSN 1353-2561.

REMPEC. Report of the regional workshop on response to spill incidents involving hazardous and noxious substances (medexpol 2018). Technical report, Regional Marine Pollution Emergency Response Centre for the Mediterranean Sea, 2018.

T. S. Richards, Q. Aubourg, and B. R. Sutherland. Radial intrusions from turbulent plumes in uniform stratification. *Physics of Fluids*, 26, 3 2014. ISSN 10897666. doi: 10.1063/1.4869119.

H. Rye and P. J. Brandvik. Verification of subsurface oil spill models. *Proceedings of the 1997 International Oil Spill Conference*, pages 551–557, 1997. URL https://api.semanticscholar.org/CorpusID:128469292.

H. Rye, P. Brandvik, and M. Reed. Subsurface oil release field experiment - observations and modelling of subsurface plume behaviour. *Proceedings of the 19th AMOP Technical Seminar*, pages 1417–1435, 1996.

H. Rye, P. J. Brandvik, and T. Strøm. Subsurface blowouts: Results from field experiments. *Spill Science and Technology Bulletin*, 4:239–256, 1997.

M. Schatzmann. An integral model of plume rise. *Atmospheric Environment (1967)*, 13:721–731, 1979. ISSN 0004-6981. doi: https://doi.org/10.1016/0004-6981(79)90202-6. URL https://www.sciencedirect.com/science/article/pii/0004698179902026.

S. Shah, A. Heemink, and E. Deleersnijder. Assessing lagrangian schemes for simulating diffusion on non-flat isopycnal surfaces. *Ocean Modelling*, 39(3): 351–361, 2011. ISSN 1463-5003. doi: https://doi.org/10.1016/j.ocemod.2011.05.008. URL https://www.sciencedirect.com/science/article/pii/S1463500311001016.

S. A. Socolofsky and E. E. Adams. Multi-phase plumes in uniform and stratified crossflow. *Journal of Hydraulic Research*, 40:661–672, 2002. ISSN 00221686. doi: 10.1080/00221680209499913.

S. A. Socolofsky, T. Bhaumik, and D.-G. Seol. Double-plume integral models for near-field mixing in multiphase plumes. *Journal of Hydraulic Engineering*, 134 (6):772–783, 2008. ISSN 1943-7900.

S. A. Socolofsky, E. E. Adams, and C. R. Sherwood. Formation dynamics of subsurface hydrocarbon intrusions following the deepwater horizon blowout. *Geophysical Research Letters*, 38(9), 2011. doi: https://doi.org/10.1029/2011GL047174. URL https://agupubs.onlinelibrary.wiley.com/doi/abs/10.1029/2011GL047174.

S. A. Socolofsky, E. E. Adams, C. B. Paris, and D. Yang. How do oil, gas, and water interact near a subsea blowout? *Oceanography*, 29:64–75, 9 2016. ISSN 10428275. doi: 10.5670/oceanog.2016.63.

M. Sotillo, E. A. Fanjul, S. Castanedo, A. Abascal, J. Menendez, M. Emelianov, R. Olivella, E. García-Ladona, M. Ruiz-Villarreal, J. Conde, M. Gómez, P. Conde,

A. Gutierrez, and R. Medina. Towards an operational system for oil-spill forecast over spanish waters: Initial developments and implementation test. *Marine Pollution Bulletin*, 56(4):686–703, 2008. ISSN 0025-326X. doi: https://doi.org/10.1016/j.marpolbul.2007.12.021. URL https://www.sciencedirect.com/science/article/pii/S0025326X08000040.

M. Spaulding, Z. Li, D. Mendelsohn, D. Crowley, D. French-McCay, and A. Bird. Application of an integrated blowout model system, oilmap deep, to the deepwater horizon (dwh) spill. *Marine Pollution Bulletin*, 120, 05 2017. doi: 10.1016/j.marpolbul.2017.04.043.

M. L. Spaulding, V. S. Kolluru, E. Anderson, and E. Howlett. Application of three-dimensional oil spill model (wosm/oilmap) to hindcast the braer spill. *Spill Science and Technology Bulletin*, 1:23–35, 1994. ISSN 1353-2561. doi: https://doi.org/10.1016/1353-2561(94)90005-1. URL https://www.sciencedirect.com/science/article/pii/1353256194900051.

P.-Y. Traon, A. Reppucci, E. Alvarez Fanjul, L. Aouf, A. Behrens, M. Belmonte Rivas, B. Abderrahim, L. Bertino, V. Brando, M. Kreiner, B. Mounir, T. Carval, S. Ciliberti, H. Claustre, E. Clementi, G. Coppini, G. Cossarini, M. de Alfonso Alonso Muñoyerro, A. Delamarche, and A. Zacharioudaki. From observation to information and users: The copernicus marine service perspective. *Frontiers in Marine Science*, 05 2019.

UN. United nations, sdg 14, 2015. URL https://sdgs.un.org/goals/goal14.

C. Y. Wang and R. V. Calabrese. Drop breakup in turbulent stirred-tank contactors. part ii: Relative influence of viscosity and interfacial tension. *AIChE Journal*, 32: 667–676, 4 1986. ISSN 1547-5905. doi: 10.1002/AIC.690320417. URL https://onlinelibrary.wiley.com/doi/full/10.1002/aic.690320417https:

//onlinelibrary.wiley.com/doi/abs/10.1002/aic.690320417https://aiche.onlinelibrary.wiley.com/doi/10.1002/aic.690320417.

L. D. Winiarski and W. F. Frick. *Cooling tower plume model*. US Environmental Protection Agency, Office of Research and Development, 1976.

S. Wright. Effects of ambient crossflows and density stratification on the characteristic behavior of round turbulent buoyant jets. *Calif Inst Technol W M Keck Lab Hydraul Water Resour Rep KH-R KH-R-36*, 03 1977a.

S. J. Wright. Mean behavior of buoyant jets in a crossflow. *Journal of the Hydraulics Division*, 103:499–513, 5 1977b. ISSN 0044-796X. doi: 10.1061/JYCEAJ.0004749.

D. Yang, B. Chen, S. A. Socolofsky, M. Chamecki, and C. Meneveau. Large-eddy simulation and parameterization of buoyant plume dynamics in stratified flow. *Journal of Fluid Mechanics*, 794:798–833, 5 2016a. ISSN 14697645. doi: 10.1017/jfm.2016.191.

D. Yang, B. Chen, S. A. Socolofsky, M. Chamecki, and C. Meneveau. Large-eddy simulation and parameterization of buoyant plume dynamics in stratified flow. *Journal of Fluid Mechanics*, 794:798–833, 5 2016b. ISSN 14697645. doi: 10.1017/jfm.2016.191.

P. D. Yapa and Z. Li. Simulation of oil spills from underwater accidents i: Model development. *Journal of Hydraulic Research*, 35:673–688, 1997. ISSN 00221686. doi: 10.1080/00221689709498401.

P. D. Yapa, L. Zheng, and K. Nakata. Modeling underwater oil/gas jets and plumes. *Journal of Hydraulic Engineering*, 125:481–491, 5 1999. ISSN 0733-9429. doi: 10.1061/(ASCE)0733-9429(1999)125:5(481).

P. D. Yapa, L. I. Zheng, and F. Chen. A model for deepwater oil/gas blowouts, 2002.

P. D. Yapa, M. R. Wimalaratne, A. L. Dissanayake, and J. A. DeGraff. How does oil and gas behave when released in deepwater? *Journal of Hydro-Environment Research*, 6:275–285, 12 2012. ISSN 15706443. doi: 10.1016/j.jher.2012.05.002.

E. Zambianchi, M. Trani, and P. Falco. Lagrangian transport of marine litter in the mediterranean sea. *Frontiers in Environmental Science*, 5, 2 2017. ISSN 2296665X. doi: 10.3389/fenvs.2017.00005.

L. Zhao, M. C. Boufadel, S. A. Socolofsky, E. Adams, T. King, and K. Lee. Evolution of droplets in subsea oil and gas blowouts: Development and validation of the numerical model vdrop-j. *Marine Pollution Bulletin*, 83:58–69, 6 2014. ISSN 18793363. doi: 10.1016/j.marpolbul.2014.04.020.

B. L. Zheng and P. D. Yapa. Buoyant velocity of spherical and nonspherical bubbles/droplets.

L. Zheng and P. D. Yapa. Simulation of oil spills from underwater accidents ii: Model verification. *Journal of Hydraulic Research*, 36:117–134, 1998. ISSN 00221686. doi: 10.1080/00221689809498381.

L. Zheng, P. Yapa, and F. Chen. A model for simulating deepwater oil and gas blowouts - part i: Theory and model formulation. *Journal of Hydraulic Research - J HYDRAUL RES*, 41:339–351, 07 2003. doi: 10.1080/00221680309499980.

Acknowledgements

I would like to express my sincere gratitude to my supervisors: Prof. Nadia Pinardi, whose advice and experience have greatly enriched this thesis; Dr. Giovanni Coppini and Dr. Gianandrea Mannarini for their support and guidance throughout the thesis development process. Many thanks also to Dr. Francesco Trotta, whose technical expertise consistently contributed to the improvement of this work. Additionally, I thank the CMCC institution in Lecce for providing a great work environment.

I am very grateful to Dr. Ana Julia Abascal and Dr. Andrés García Gómez, for their scientific support but also for welcoming me into a vibrant community at IHCantabria. This period has been one of academic and personal growth, and I extend my thoughts to all *los chicos*.

I am eager to thank some special people who accompanied me through this journey. Alessia, who has been for me a gentle and powerful mirror and Alessandra, for making me understand what is to be taken and to be left. Rossana again, for her affection and love. This journey has been quite a ride, but I've had the SudEst Climb association in Lecce by my side all along, for which I'm grateful. I thank Fabio, my friend and soulmate, as well as my parents, and my sister Silvia.